Pontifícia Universidade Católica
do Rio de Janeiro

Pâmela Pires de Paula

Influence of surface coating and ultra-high performance concrete matrix on the mechanical behavior of carbon textile reinforced concrete

Dissertação de Mestrado

Dissertation presented to the Programa de Pós-Graduação em Engenharia Civil of PUC-Rio in partial fulfillment of the requirements for the degree of Mestre em Engenharia Civil.

Advisor: Prof. Flávio de Andrade Silva

Co-advisor: Prof. Rebecca Mansur de Castro Silva

Rio de Janeiro
April 2025

Pontifícia Universidade Católica
do Rio de Janeiro

Pâmela Pires de Paula

Influence of surface coating and ultra-high performance concrete on the mechanical behavior of carbon textile reinforced concrete

Dissertation presented to the Programa de Pós-Graduação em Engenharia Civil of PUC-Rio in partial fulfillment of the requirements for the degree of Mestre em Engenharia Civil. Approved by the Examination Committee.

Prof. Flávio de Andrade Silva
Advisor
Departamento de Engenharia Civil e Ambiental – PUC-Rio

Prof. Rebecca Mansur de Castro Silva
Co-advisor
Universidade Federal Fluminense

Prof. Alva Peled
Ben-Gurion University of the Negev

Prof. Tine Tysmans
Vrije Universiteit Brussel

Rio de Janeiro, April 3rd, 2025

All rights reserved.

Pâmela Pires de Paula

Graduated in Civil Engineering at Pontifícia Universidade Católica do Rio de Janeiro (PUC-Rio) in 2022. The area of interest encompasses textile reinforced concrete, cement-based composites, and experimental research.

Bibliographic data

Paula, Pâmela Pires de

Influence of surface coating and ultra-high performance concrete matrix on the mechanical behavior of carbon textile reinforced concrete / Pâmela Pires de Paula ; advisor: Flávio de Andrade Silva ; co-advisor: Rebecca Mansur de Castro Silva. – 2025.

144 f. : il. color. ; 30 cm

Dissertação (mestrado)–Pontifícia Universidade Católica do Rio de Janeiro, Departamento de Engenharia Civil e Ambiental, 2025.

Inclui bibliografia

1. Engenharia Civil e Ambiental - Teses. 2. Concreto têxtil. 3. Tecido de carbono. 4. Tratamentos alternativos. 5. Concreto de ultra alto desempenho. 6. Comportamento estrutural. I. Silva, Flávio de Andrade. II. Silva, Rebecca Mansur de Castro. III. Pontifícia Universidade Católica do Rio de Janeiro. Departamento de Engenharia Civil e Ambiental. IV. Título.

CDD: 624

Acknowledgements

To Prof. Flávio de Andrade Silva, my advisor, for all support. Thank you for believing in me. Thank you for your patience, encouragement, dedication, and suggestions necessary for the completion of this research.

To Prof. Rebecca Mansur de Castro Silva, my co-advisor, for the support, patience, dedication, and encouragement. Thank you for agreeing to guide me along with Prof. Flávio. I have learned a lot from you, and I am really grateful for having had you as my co-advisor.

To my parents, Karla and Walmir, for everything. Thank you for your support, encouragement and love.

To my sister, Ludmyla, for the support and love.

To Andreas, for all love, support, and encouragement.

To the technical staff of LEM-DEC, Euclides, Rogério, Jhansen, Marques, and Anderson, for your help and company during my time at the laboratory.

To the friends I have made along the way during my time at the laboratory: Felipe Rodrigues, Júlio, José Victor, Victtor Feijão, Júlia, Gabriel, Jessé, Renan Felinto, and Rennan Liberato.

To the Institut für Textiltechnik (ITA) from RWTH Aachen University, in particular Martin Scheurer, for providing some of the carbon fabrics used in this study.

This study was financed in part by the Coordenação de Aperfeiçoamento de Pessoal de Nível Superior - Brasil (CAPES) - Finance Code 001, and by the Brazilian funding agency CNPq.

Abstract

Pires de Paula, Pâmela; de Andrade Silva, Flávio (Advisor). **Influence of surface coating and ultra-high performance concrete matrix on the mechanical behavior of carbon textile reinforced concrete**. Rio de Janeiro, 2025. 144p. Dissertação de Mestrado - Departamento de Engenharia Civil e Ambiental, Pontifícia Universidade Católica do Rio de Janeiro.

The interest in using textile reinforcements for concrete has grown increasingly in recent decades. Carbon textiles, in particular, exhibit excellent mechanical properties and durability, being an interesting alternative in applications such as Textile Reinforced Concrete (TRC). Nevertheless, carbon fibers exhibit brittle failure and poor bonding with cementitious matrices. This work aims to investigate the influence of alternative polymeric coatings, namely a water-based epoxy (WBEP), and a thermoplastic resin (THRM), and an ultra-high performance concrete (UHPC) matrix on the mechanical and structural behavior of carbon TRC. The use of polymeric coatings is a well-established method to improve the bond of carbon fabrics with cementitious matrices. Contact angle tests were performed to understand the influence of the different coatings on the hydrophobicity of the carbon yarns, while three-point bending tests were conducted to evaluate the stiffness conferred by the WBEP and THRM coatings in comparison with commercially available carbon fabrics coated with epoxy (EPXY) and styrene-butadiene rubber (SBR). Direct tensile tests were performed to assess the mechanical performance of the TRC composites with the WBEP and THRM coatings. Additionally, the tensile behavior of epoxy-coated textiles embedded in a UHPC matrix was investigated. The results indicate that both the WBEP and THRM coatings exhibit mechanical properties comparable to EPXY. The incorporation of dispersed steel fibers into the matrix contributes to enhancing the ductility of the composites. The composites with the UHPC matrix showed enhanced mechanical performance compared to those with the fine-grained concrete matrix. The specimens presented a higher first crack strength, smaller cracks, and no spalling. At the structural level, carbon TRC I-section beams with the aforementioned variables were tested under four-point bending tests. The results demonstrated the suitability of the WBEP and THRM coatings for use in TRC

structural elements, with WBEP presenting a better overall structural performance. The UHPC matrix also improved the load-bearing capacity, durability, and user safety, with no spalling detected. These findings contribute to the development of more durable and sustainable TRC structures, potentially expanding the range of applications of this versatile material.

Keywords

Textile reinforced concrete (TRC); carbon fabrics; alternative coatings; water-based epoxy; thermoplastic resin; ultra-high performance concrete (UHPC); composite materials; structural behavior.

Resumo

Pires de Paula, Pâmela; de Andrade Silva, Flávio (Orientador). **Influência da impregnação e da matriz de concreto de ultra alto desempenho no comportamento mecânico do concreto têxtil de tecido de carbono**. Rio de Janeiro, 2025. 144p. Dissertação de Mestrado - Departamento de Engenharia Civil e Ambiental, Pontifícia Universidade Católica do Rio de Janeiro.

O interesse em usar reforços têxteis para concreto tem crescido cada vez mais nas últimas décadas. Os tecidos de carbono, em particular, apresentam excelentes propriedades mecânicas e durabilidade, sendo uma alternativa interessante em aplicações como o concreto têxtil (TRC). No entanto, as fibras de carbono apresentam um modo de falha frágil e uma fraca aderência com matrizes cimentícias. Este trabalho tem como objetivo investigar a influência de tratamentos poliméricos alternativos, nomeadamente um epóxi à base de água (WBEP) e uma resina termoplástica (THRM), e uma matriz de concreto de ultra alto desempenho (UHPC) no comportamento mecânico e estrutural do TRC de carbono. O uso de tratamentos (*coatings*) poliméricos é um método bem estabelecido para melhorar a aderência de tecidos de carbono com matrizes cimentícias. Ensaios de ângulo de contato foram realizados para entender a influência dos diferentes tratamentos na hidrofobicidade dos cordões de carbono, enquanto ensaios de flexão em três pontos foram conduzidos para avaliar a rigidez conferida pelos revestimentos WBEP e THRM em comparação com tecidos tratados com epóxi (EPXY) e borracha de estireno-butadieno (SBR), disponíveis comercialmente. Ensaios de tração direta foram realizados para avaliar o desempenho mecânico dos compósitos TRC com *coatings* de WBEP e THRM. Além disso, o comportamento de tração dos tecidos de carbono tratados com epóxi combinados com uma matriz UHPC foi investigado. Os resultados indicam que tanto os revestimentos WBEP quanto THRM exibem propriedades mecânicas comparáveis ao EPXY. A incorporação de fibras de aço dispersas na matriz contribui para aumentar a ductilidade dos compósitos. Os compósitos com a matriz de UHPC mostraram desempenho mecânico superior em comparação com aqueles com a matriz de concreto fino. Os corpos de prova apresentaram maior resistência à primeira fissura, fissuras menores e nenhum *spalling*. No nível estrutural, vigas de seção I de TRC de carbono com as variáveis mencionadas acima foram ensaiadas sob flexão de quatro pontos. Os resultados

demonstraram a adequação dos tratamentos de WBEP e THRM para uso em elementos estruturais TRC, com WBEP apresentando um melhor desempenho estrutural geral. A matriz UHPC também melhorou a capacidade de carga, durabilidade e segurança, sem a ocorrência de *spalling*. Esses resultados contribuem para o desenvolvimento de estruturas TRC mais duráveis e sustentáveis, potencialmente expandindo a gama de aplicações desse material versátil.

Palavras-chave

Concreto têxtil; tecido de carbono; tratamentos alternativos; epóxi à base d'água; resina termoplástica; concreto de ultra alto desempenho; materiais compósitos; comportamento estrutural.

Table of Contents

1 Introduction 18
1.1. Motivation 18
1.2. Objectives 20
1.3. Thesis structure 21
2 Literature Review 22
2.1. Textile reinforced concrete: overview 22
2.2. Cementitious matrix 25
2.2.1. Fiber reinforced concrete as TRC matrix 27
2.3. Textile reinforcement 30
2.4. Fiber-matrix interface 35
2.5. Structural behavior of TRC beams 38
3 Experimental Program 42
3.1. Introduction 42
3.2. Materials 42
3.2.1. Cementitious matrices 42
3.2.1.1. Fine-grained concrete 42
3.2.1.2. Ultra-high performance concrete 43
3.2.1.3. Mechanical properties of the matrices 46
3.2.2. Carbon textiles 48
3.2.2.1. Water-based epoxy coating process 50
3.3. Specimens manufacturing 51
3.3.1. Composite manufacturing 51
3.3.2. Structural elements manufacturing 56
3.4. Testing procedures 64
3.4.1. Scanning Electron Microscopy (SEM) 64
3.4.2. Contact angle tests 64
3.4.3. Three-point bending tests 66
3.4.4. Direct tensile tests 68
3.4.5. Four-point bending tests 70
4 Results and Discussion 73
4.1. Effect of surface coating on the physical and mechanical properties of carbon textiles 73

4.1.1. Morphological characterization 73
4.1.2. Analysis of the hydrophobicity of carbon textiles 77
4.1.3. Analysis of the stiffness of carbon textiles 80
4.2. Mechanical behavior of carbon TRC composites 83
4.2.1. Influence of surface coating 83
4.2.2. Influence of the curing time of the WBEP resin coating 93
4.2.3. Influence of the UHPC matrix 99
4.3. Flexural behavior of carbon TRC I-section beams 104
4.3.1. Influence of surface coating 104
4.3.2. Influence of the UHPC matrix 113
5 Conclusion 123
5.1. Conclusion 123
5.2. Suggestions for future works 127
6 References 128
Appendix A 142

List of Figures

Figure 2.1 - TRC structures: (a) roof structure made of precast TRC shells at RWTH Aachen University [46], (b) cylindrical shells at RWTH Aachen University [47], (c) façade of the laboratory of the Institute of Structural Concrete at RWTH Aachen University, Germany [48], and (d) pedestrian bridge in Albstadt, Germany [49]. 23

Figure 2.2 - The CUBE at TU Dresden, Germany [51]. 24

Figure 2.3 - Oricrete prototype manufacturing process [52]. 25

Figure 2.4 - Different types of fabric structures: (a) woven: plain weave, (b) woven: leno weave, (c) weft-knitted, (d) warp-knitted, and (e) bonded (adapted from [61]). 32

Figure 2.5 - 3D textile structure (adapted from [101]). 32

Figure 2.6 - Design flexibility of textile fabric obtained using the prepreg approach [116]. 34

Figure 2.7 - Multifilament yarn. 36

Figure 2.8 - Stress distribution within the yarn of (a) uncoated fabrics, (b) SBR-coated fabrics, and (c) fully epoxy-impregnated fabrics (adapted from [115]). 37

Figure 2.9 - Reinforcement configuration, cross-section dimensions, and test setup used by Valeri, Ruiz, and Muttoni [122]. 40

Figure 2.10 - Reinforcement configurations and I-section dimensions analyzed by Bielak *et al.* [123]. 40

Figure 2.11 - T-beams cross-sections and reinforcement configurations evaluated by Preinstorfer *et al.* [124]. 41

Figure 3.1 - Steel fiber used in the UHPC matrix. 44

Figure 3.2 - Compression test setup (a) overview and (b) LVDT detail. 47

Figure 3.3 - Compressive stress *vs.* strain curves of the (a) fine-grained concrete and (b) ultra-high performance concrete. 48

Figure 3.4 - Mesh opening dimensions of the (a) carbon fabric from Solidian and (b) carbon textile provided by ITA. 49

Figure 3.5 - (a) Wooden frame and uncoated textile, and (b) WBEP coating procedure. 51

Figure 3.6 - Specimens identification system. 53
Figure 3.7 - TRC plates for direct tensile tests manufacturing process. 54
Figure 3.8 - (a) Carbon TRC composite for direct tensile test and (b) detail of reduced gauge length area. 55
Figure 3.9 - Beam identification structure. 57
Figure 3.10 - (a) Cross-section dimensions of the I-section beams and (b) cross-section view of the adapted wooden rectangular formwork. 58
Figure 3.11 - (a) I-section carbon textile reinforcement assembled and (b) detail of web-flange connection. 59
Figure 3.12 - Epoxy-coated carbon fabric: (a) overlap region and (b) overlap dimensions. 59
Figure 3.13 - Hot glue stick spacer. 60
Figure 3.14 - Casting process of the beams with the conventional matrix. 61
Figure 3.15 - (a) Fiber agglomeration on the mesh opening of the textile reinforcement and (b) adapted end side of the formwork to cast the beams with the UHPC matrix. 62
Figure 3.16 - Casting process of the carbon TRC I-section beams with the UHPC matrix. 63
Figure 3.17 - Carbon TRC I-section beam. 64
Figure 3.18 - Water contact angle test setup. 65
Figure 3.19 - Detail of the water droplet. 66
Figure 3.20 - Textiles subjected to the three-point bending tests: (a) solvent-based epoxy (EPXY), (b) water-based epoxy (WBEP), (c) thermoplastic resin (THRM), and (d) SBR. 67
Figure 3.21 - Textile bending test setup. 67
Figure 3.22 - Direct tensile test setup. 68
Figure 3.23 - DIC setup for direct tensile test. 70
Figure 3.24 - Four-point bending test setup: (a) overview and (b) schematic representation (dimensions in mm). 72
Figure 3.25 - Strain gauges placed on the (a) top flange textile reinforcement and (b) on the web textile reinforcement. 72
Figure 4.1 - SEM images of the cross-sections of the (a, b, c) uncoated, (d, e, f) water-based epoxy-coated, (g, h, i) thermoplastic resin-coated, and (j, k, l) epoxy-coated carbon textiles warp yarns. 74

Figure 4.2 - SEM images of the warp yarns of the (a) uncoated, (b) water-based epoxy-coated, (c) thermoplastic resin-coated, and (d) solvent-based epoxy-coated carbon textiles. 76

Figure 4.3 - Images from the contact angle tests images for different times (10 and 60 s) for the carbon yarns. 78

Figure 4.4 - Representative load *vs.* deflection curves for the WBEP, THRM, EPXY and SBR carbon textiles obtained from the three-point bending tests. 80

Figure 4.5 - Reshaped carbon textile with the thermoplastic resin coating. 82

Figure 4.6 - Representative tensile stress *vs.* strain curves for the CONV-UNCO, CONV-WBEP-04h, CONV-WBEP-24h, CONV-WBEP-07d, CONV-THRM and CONV-EPXY carbon TRC composites calculating the stresses with the (a) composite area and (b) reinforcement area. 83

Figure 4.7 - Crack pattern before failure of carbon TRC composites: (a) CONV-UNCO, (b) CONV-WBEP-07d, (c) CONV-THRM, and (d) CONV-EPXY. 87

Figure 4.8 - Crack pattern on the CONV-WBEP-07d, CONV-THRM, and CONV-EPXY composites at various strain levels. 91

Figure 4.9 - TRC with the thermoplastic-coated textile after the direct tensile test. 92

Figure 4.10 - Representative tensile stress *vs.* strain curves for the CONV-UNCO, CONV-WBEP-04h, CONV-WBEP-24h, CONV-WBEP-07d, CONV-THRM and CONV-EPXY carbon TRC composites, calculating the stresses with the (a) composite area and (b) reinforcement area. 94

Figure 4.11 - Crack pattern before failure of carbon TRC composites: (a) CONV-UNCO, (b) CONV-WBEP-04h, (c) CONV-WBEP-24h, and (d) CONV-WBEP-07d. 96

Figure 4.12 - TRC composite with the WBEP-24h fabric after the direct tensile test. 98

Figure 4.13 - Representative tensile stress *vs.* strain curves for the CONV-EPXY and UHPC-EPXY carbon TRC composites, calculating the stresses with the (a) composite area and (b) reinforcement area. 99

Figure 4.14 - Fiber orientation on the UHPC-EPXY composites subjected to the tensile tests. 101

Figure 4.15 - Crack pattern on the CONV-EPXY and UHPC-EPXY composites at the end of Stage II and at the maximum strain (right before failure). 102

Figure 4.16 - Failure mode of the carbon TRC composites: (a) CONV-EPXY and (b) UHPC-EPXY. 104

Figure 4.17 - Load *vs.* deflection curves for the CONV-WBEP-240, CONV-THRM-240, and CONV-EPXY-240 carbon TRC beams: (a) overview and (b) detail for low deflections. 105

Figure 4.18 - Crack pattern of the (a) CONV-WBEP-240, (b) CONV-THRM-240, and (c) CONV-EPXY-240 at the SLS and at the maximum load before failure. 107

Figure 4.19 - Failure modes of the (a) CONV-WBEP-240, (b) CONV-THRM-240, and (c) CONV-EPXY-240 beams. 111

Figure 4.20 - Moment *vs.* curvature curves of the CONV-WBEP-240, CONV-THRM-240, and CONV-EPXY-240 carbon TRC beams. 112

Figure 4.21 - Load *vs.* deflection curves for the CONV-EPXY-240, UHPC-EPXY-240, CONV-EPXY-300, and UHPC-EPXY-300 carbon TRC beams: (a) overview and (b) detail for low deflections. 114

Figure 4.22 - Crack pattern of the (a) CONV-EPXY-240 and (b) UHPC-EPXY-240 beams at the SLS and at the maximum load. 117

Figure 4.23 - Failure modes of the (a) CONV-EPXY-240, (b) UHPC-EPXY-240, (c) CONV-EPXY-300, and (d) UHPC-EPXY-300 carbon TRC I-section beams. 120

Figure 4.24 - Moment *vs.* curvature curves of the CONV-EPXY-240, UHPC-EPXY-240, CONV-EPXY-300 and UHPC-EPXY-300 carbon TRC beams. 121

Figure A.0.1 - Tensile stress *vs.* strain curves of the CONV-UNCO carbon TRC composites with the tensile stress obtained using the: (a) composite cross-sectional area and (b) reinforcement area. 142

Figure A.0.2 - Tensile stress *vs.* strain curves of the CONV-WBEP-04h carbon TRC composites with the tensile stress obtained using the: (a) composite cross-sectional area and (b) reinforcement area. 142

Figure A.0.3 - Tensile stress *vs.* strain curves of the CONV-WBEP-24h carbon TRC composites with the tensile stress obtained using the: (a) composite cross-sectional area and (b) reinforcement area. 143

Figure A.0.4 - Tensile stress *vs.* strain curves of the CONV-WBEP-07d carbon TRC composites with the tensile stress obtained using the: (a) composite cross-sectional area and (b) reinforcement area. 143

Figure A.0.5 - Tensile stress *vs.* strain curves of the CONV-THRM carbon TRC composites with the tensile stress obtained using the: (a) composite cross-sectional area and (b) reinforcement area. 143

Figure A.0.6 - Tensile stress *vs.* strain curves of the CONV-EPXY carbon TRC composites with the tensile stress obtained using the: (a) composite cross-sectional area and (b) reinforcement area. 144

Figure A.0.7 - Tensile stress *vs.* strain curves of the UHPC-EPXY carbon TRC composites with the tensile stress obtained using the: (a) composite cross-sectional area and (b) reinforcement area. 144

List of Tables

Table 3.1 - Fine-grained concrete composition [15]. 43
Table 3.2 - Steel fiber properties (according to the manufacturer). 44
Table 3.3 - Ultra-high performance concrete composition [127]. 45
Table 3.4 - Average compressive tests results of the matrices. 48
Table 3.5 - Technical data of the Solidian carbon textile (according to the supplier). 49
Table 3.6 - Technical data of the carbon textiles provided by ITA. 49
Table 3.7 - Technical data of the MC-DUR-1177 WV-A resin [131]. 50
Table 3.8 - Test variables and specimen identification. 53
Table 3.9 - Average gauge length thickness of the TRC plates. 54
Table 3.10 - Reinforcement area of the composites for the tensile tests. 56
Table 3.11 - Test variables and beam identification. 57
Table 3.12 - Direct tensile tests boundary conditions. 69
Table 4.1 - Average measured contact angles of the carbon yarns. 77
Table 4.2 - Average load and flexural stiffness results of three-point bending tests on the carbon fabrics at an 80 mm mid-span deflection. 81
Table 4.3 - Average results of the direct tensile tests for the CONV-UNCO, CONV-WBEP-07d, CONV-THRM, and CONV-EPXY carbon TRC composites. 84
Table 4.4 - Average results of DIC cracking analysis of the CONV-UNCO, CONV-WEBP-07d, CONV-THRM, and CONV-EPXY composites at the ultimate load. 88
Table 4.5 - Average results of the direct tensile tests for the CONV-WBEP-04h, CONV-WBEP-24h, and CONV-WBEP-07d carbon TRC composites. 94
Table 4.6 - Average results of DIC cracking analysis of the TRC composites at the ultimate load. 95
Table 4.7 - Average results of the direct tensile tests for the CONV-EPXY and UHPC-EPXY carbon TRC composites. 100
Table 4.8 - Average results of DIC cracking analysis of the TRC composites at the ultimate load. 103

Table 4.9 - Main results obtained from the four-point bending tests on the carbon TRC I-section beams: CONV-WBEP-240, CONV-THRM-240, and CONV-EPXY-240. 105

Table 4.10 - DIC analysis results at different deflection levels for the CONV-WBEP-240, CONV-THRM-240, and CONV-EPXY-240 carbon TRC beams. 108

Table 4.11 - Main results obtained from the four-point bending tests on the carbon TRC I-section beams: CONV-EPXY-240, UHPC-EPXY-240, CONV-EPXY-300, and UHPC-EPXY-240. 114

Table 4.12 - DIC analysis results at different deflection levels for the CONV-EPXY-240 and UHPC-EPXY-240 carbon TRC I-section beams. 117

1
Introduction

1.1.
Motivation

The history of civil construction is marked by the pursuit of materials and techniques that allow the construction of resistant, durable, and economically viable structures. The development of Portland cement in 1824 was a crucial milestone in this trajectory [1]. This innovative material has revolutionized how structures were built, and its influence continues to this day. With the development of Portland cement, concrete has become the most used construction material and the second most consumed material in the world, being surpassed only by water [2].

Although widely used, concrete presents low tensile strength and is considered a highly polluting material due to the high levels of CO_2 emissions associated with cement production [3]. Traditionally, steel has been used as reinforcement to mitigate concrete's low tensile strength. Steel offers advantages such as the ability to withstand both tensile and compressive stresses, relative ease of handling on site, and ductile behavior [4]. However, its use as reinforcement in concrete is not without challenges. As an oxidizable metal, steel is susceptible to corrosion when exposed to aggressive environments and substances [5]. Corrosion makes the structure vulnerable to loss of strength under applied loads, as this phenomenon not only reduces the cross-sectional area of the steel rebar but also leads to a loss of bond between the concrete and the reinforcement [5], compromising the load-bearing capacity of steel Reinforced Concrete (RC) structures.

Design guidelines for concrete structures, such as the Brazilian Standard ABNT NBR 6118 [6], recommend the use of an additional concrete layer to protect the steel reinforcement and mitigate the corrosion process. Nevertheless, this protective layer results in higher and heavier cross-sections and increased environmental impact due to the higher required amount of concrete. To address

these limitations, alternative materials have been explored, leading to the development of Textile Reinforced Concrete (TRC).

TRC presents a promising alternative to steel RC by combining fine-grained concrete with corrosion-resistant textile reinforcements [7], enabling the creation of thinner, lighter structures with complex geometries [8]. Moreover, this composite offers significant advantages, including reduced material consumption, lower environmental impact through minimized concrete cover, and enhanced durability due to the inherent corrosion resistance of the reinforcement [7,9,10].

Among the several types of textiles currently available, carbon-based fabrics stand out because of their high mechanical properties, alkali resistance, and low specific weight [11,12]. Nevertheless, the multifilament structure of carbon yarns, along with the hydrophobic nature of these fibers [11], presents challenges in achieving an adequate bond with the cementitious matrix and uniform stress distribution within the strand, compromising the overall mechanical performance of the composite [7]. Polymers such as solvent-based epoxies and styrene-butadiene rubber (SBR) have been consistently used to coat these fabrics and improve stress distribution.

Although epoxy coatings provide TRC composites with excellent mechanical behavior, the use of solvent-based epoxy has been associated with delamination issues related to the hydrophobic properties of this resin [13,14]. Conversely, SBR offers design flexibility not achieved with epoxy coatings; however, it results in composites with compromised mechanical properties [15], limiting the mechanical potential of high-performance materials, such as carbon TRC.

New coating materials have been investigated to overcome the limitations of traditional treatments. An alternative to solvent-based epoxy coatings is the use of water-dispersed epoxy. Waterborne epoxies can help improve the chemical bond with the cementitious matrices due to their more hydrophilic nature, while also providing benefits in terms of sustainability because of their lower volatile organic compound (VOC) emissions [16]. The use of a water-based epoxy coating has been explored in previous research [17], and the results indicated the potential of this resin as an alternative to commonly used solvent-based epoxies. Nevertheless, further evaluation of this epoxy as a coating material on both material and structural levels remains to be done.

For coating materials offering design flexibility, thermoplastic resins have been considered [18]. Unlike thermosetting resins, thermoplastics allow for easy reshaping of textile reinforcements through the application of thermal energy, due to their ability to repeatedly soften and solidify with temperature changes [19]. While Heins *et al.* [18] investigated the effect of these coatings on textile mechanical properties, their performance at the composite and structural levels remains unexplored.

This study aims to evaluate the mechanical and structural behavior of carbon TRC with these alternative coatings (a water-based epoxy and a thermoplastic resin), aiming to contribute to the understanding of this composite material, enabling its future practical applications.

Additionally, since the cementitious matrix plays a crucial role in the performance of TRC, this study also evaluates the influence of an ultra-high performance concrete (UHPC) matrix with steel fiber addition on the mechanical and structural performance of carbon TRC incorporating commercial solvent-based epoxy-coated fabric. The use of UHPC as a matrix in TRC with high-strength fabrics, such as carbon, can be an extremely attractive option for structures that require a long service life and special properties, such as high ductility and impact resistance [9].

1.2. Objectives

The main objective of this research is to investigate the impact of two alternative coatings (water-dispersed epoxy and thermoplastic resin), as well as the influence of an ultra-high performance concrete (UHPC) matrix, on the mechanical and structural performance of carbon textile reinforced concrete (TRC). To achieve this, the following secondary goals were defined:

- Investigation of the hydrophobicity of carbon yarns with water-based epoxy and thermoplastic resin coatings, as well as carbon yarns with a solvent-based epoxy coating, through water contact angle tests;
- Assessment of the stiffness imparted by water-based epoxy and thermoplastic resin impregnations on the carbon textiles through three-

point bending tests, in comparison to commercial fabrics with solvent-based epoxy and SBR coatings;

- Characterization of the different carbon TRC composites through direct tensile tests. Composites with fine-grained concrete matrix and textiles with water-dispersed epoxy, thermoplastic resin, and solvent-dispersed epoxy coatings were analyzed. Additionally, specimens with ultra-high performance concrete matrix and textile with solvent-based epoxy were evaluated;
- Analysis of the structural behavior of carbon TRC I-section beams through four-point bending tests. Beams using textile reinforcements with water-based epoxy, thermoplastic resin, and solvent-based epoxy coatings, in combination with fine-grained concrete matrix were evaluated. Furthermore, beams with ultra-high performance concrete matrix and solvent-based epoxy-coated textile reinforcement were studied.

1.3. Thesis structure

This thesis is divided into five chapters, namely: Introduction, Literature Review, Experimental Program, Results and Discussion, and Conclusion.

Chapter 1 presents the introduction, motivation, objectives, and the thesis structure.

Chapter 2 contains a literature review on the main aspects of textile reinforced concrete. It presents definitions and general concepts related to this material, including the matrices and fabrics used, fiber-matrix interface, mechanical behavior of TRC composites, and structural performance of textile reinforced concrete beams.

Chapter 3 details the experimental program. The materials used in this study, the manufacturing processes for casting the specimens, and the description of the testing procedures are presented in this chapter.

Chapter 4 contains the results and discussions of the tests conducted.

Chapter 5 outlines the conclusions of this study, followed by suggestions for future works.

2
Literature Review

2.1.
Textile reinforced concrete: overview

Textile Reinforced Concrete (TRC), also known in the literature as Textile Reinforced Mortar (TRM) [20–27] and Fabric Reinforced Cementitious Matrix (FRCM) [28–36], is a relatively new composite material that consists of a cementitious matrix and one or multiple layers of textile reinforcements composed of continuous fibers of natural or synthetic origin [7].

According to Scheerer *et al.* [37], the early development of TRC can be traced to the beginning of the 1980s when the first research activities and patents of technical fabrics to reinforce cementitious matrices began to emerge. However, it was only in the early to mid-90s that initial studies [38–40] on the use of fabric reinforcements for concrete were published, and it was not until the end of the decade that the term "textile reinforced concrete" was used for the first time [41].

In the early 2000s, more research on textile reinforced concrete started being conducted and the first technical committee dedicated exclusively to the study of this material [42], namely the Technical Committee 201-TRC, was created by RILEM (*Réunion Internationale des Laboratoires et Experts des Matériaux, systèmes de construction et ouvrages*) in 2003. Although there is no information on the exact year, the topic was also included within the scope of study of the Committee 549 - Thin Reinforced Cementitious Products and Ferrocement [43] of the American Concrete Institute (ACI) at the beginning of the decade.

With the creation and inclusion of TRC in technical committees, this composite material started gaining more attention around the world, and in 2006, the first international conference on the subject was held in Aachen, Germany. In the same year, the first state-of-the-art report on TRC [7] was published by RILEM. Since then, extensive research has been conducted to evaluate its main components, mechanical performance, structural behavior, and applications.

Despite being a recent material, TRC offers several advantages over Steel Reinforced Concrete (RC). This composite combines high tensile strength and elevated durability due to the corrosion resistance of the textile reinforcements [9]. As the fabrics are not subjected to corrosion, the additional layer of concrete used to protect the reinforcement, known as minimal cover, is no longer required. Thus, the amount of concrete utilized to cast structural elements can be significantly reduced, allowing the creation of thinner and lighter elements [10,41]. According to Alexander and Shashikala [44], replacing steel rebars with textile reinforcements can reduce concrete consumption by up to 80%. Thus, considering that 7% of all global CO_2 emissions are attributed to the cement industry [45], TRC also becomes an extremely advantageous material in terms of sustainability when compared to steel RC.

Textile reinforced concrete can be used in the manufacturing of new load-bearing structures. In addition, due to its ease of production, this composite is an extremely attractive alternative for use in the precast industry in the manufacturing of sandwich panels, water and sewage pipes, roofs, as well as ventilated façade systems. Figure 2.1 shows some examples of existing structural elements made of TRC.

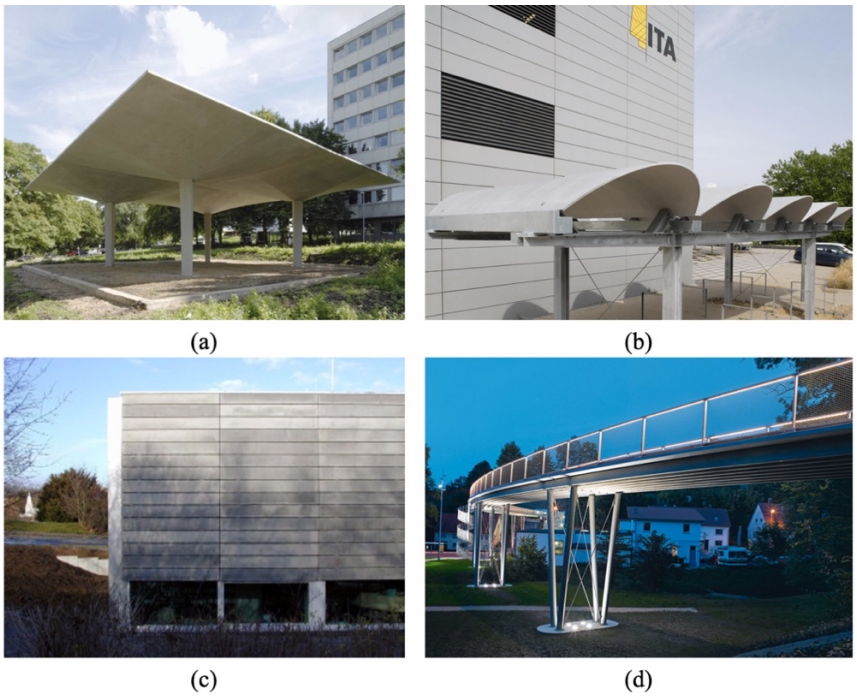


Figure 2.1 - TRC structures: (a) roof structure made of precast TRC shells at RWTH Aachen University [46], (b) cylindrical shells at RWTH Aachen University [47], (c) façade of the laboratory of the Institute of Structural Concrete at RWTH Aachen University, Germany [48], and (d) pedestrian bridge in Albstadt, Germany [49].

Recently, the first building entirely made of carbon TRC was constructed on the campus of TU Dresden as part of the German project "C^3 – Carbon Concrete Composite" (Figure 2.2). Named "The CUBE", the construction has an area of 243 m^2 and was inaugurated in September 2022 [50]. According to Henn [51], the architectural firm that developed the project alongside TU Dresden, the curved design of the structure was specifically intended to highlight the design flexibility offered by textile reinforced concrete.



Figure 2.2 - The CUBE at TU Dresden, Germany [51].

An interesting application of TRC in the construction of new structural or nonstructural elements that showcases its design flexibility is in the so-called Oricrete. According to Chudoba [52], Oricrete follows the folding technique of origami to manufacture spatial elements made of continuously reinforced thin-walled cementitious plates without the need for formwork (see Figure 2.3). This technique, developed by researchers at the RWTH Aachen University [53], allows the production of structural or nonstructural elements with complex geometries by simply adjusting the crease pattern or its parameters [52].

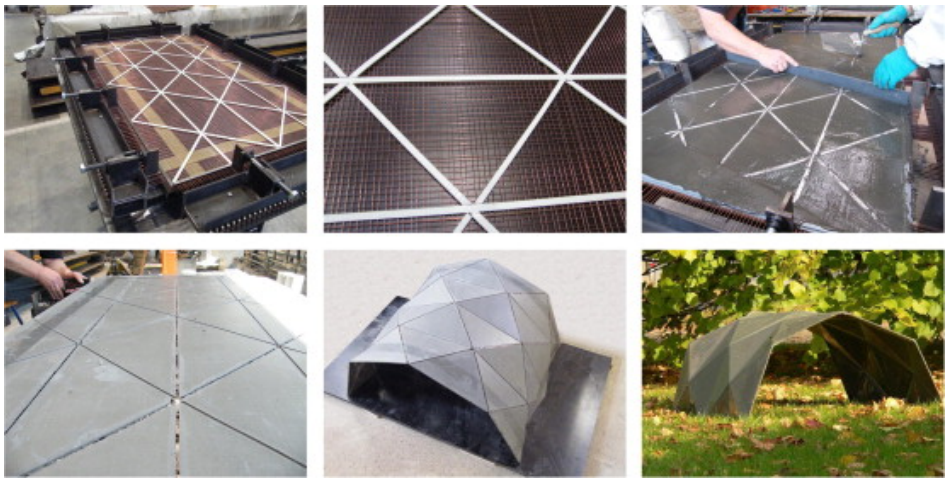


Figure 2.3 - Oricrete prototype manufacturing process [52].

TRC can also be used to strengthen, repair, and retrofit existing structures, being often referred to in this case as Fabric Reinforced Cementitious Matrix (FRCM). The use of external layers of TRC emerges as an economical and sustainable alternative for extending the lifespan of structures and increasing the load-bearing capacity of beams [28–30], slabs [31,54,55], columns [32–34], roofs and even concrete bridges. Silva [56] has shown that with proper surface preparation, TRC achieves a good bond with the strengthened structure, and an adequate load distribution between elements is accomplished.

Strengthening structures with textile reinforced concrete avoids the demolition and reconstruction of the structure, highlighting another sustainable aspect offered by this material. Some examples of the use of TRC for this purpose include the strengthening of the Hyper Shell roof [57] in Magdeburg, Germany, the structural rehabilitation of a vehicle bridge near Frankfurt [58], also in Germany. In Brazil, carbon fabrics produced by S&P Clever Reinforcement have been used to strengthen the support pillars of the new roof in the Maracanã Stadium [59].

2.2. Cementitious matrix

Composite materials generally consist of two phases: matrix and reinforcement. The matrix is the phase that shapes the material and is responsible for receiving and distributing the stresses to the reinforcement as well as protecting it [60]. Thus, the matrix plays a role as important as that of the reinforcement in the properties and mechanical behavior of composite materials such as TRC.

The cementitious matrices commonly used in textile reinforced concrete consist of fine-grained concrete made of materials with a particle size limited to 2 mm [7]. The restricted particle size of the dry materials ensures that the concrete can penetrate the small mesh openings of the fabrics. The complete penetration of the matrix into the mesh openings of the fabric is essential for the proper functioning of the reinforcement in conjunction with the matrix directly influencing the mechanical behavior of the material [61]. Since they do not contain coarse aggregates in their composition, these matrices are technically mortars; thus, TRC is also referred to as Textile Reinforced Mortar. However, due to their high mechanical properties, they are referred to as fine-grained concrete [7].

Plastic consistency, low viscosity, good workability, and low water-to-binder ratio are some of the rheological characteristics that matrices should present during the composite manufacturing in order to obtain the desired properties [62]. A plastic consistency combined with low viscosity allows the matrix to flow easily through the mesh openings. Ease of casting and efficient compaction can be achieved through good workability. A low water-cement ratio provides high mechanical strength to the matrix in its hardened state. Silica fume, fly ash, metakaolin, and superplasticizers are additives frequently used in TRC matrix mixes to obtain the above mentioned properties [7].

The matrix composition should be adapted according to the desired application, project, and type of textile reinforcement [7]. The use of refractory concrete is an interesting alternative for applications that require high temperature resistance [63–65]. Some types of fibers such as glass, alkali-resistant glass (AR glass), and natural fibers, are prone to chemical degradation when exposed to highly alkaline environments due to their low alkali resistance [66–69]. Thus, glass-, AR-glass-, and natural-based fabrics require matrices with reduced clinker content to fulfill durability requirements. Several studies [69–73] have shown that partial replacement of Portland cement with pozzolans is an effective solution to enhance the durability of such fibers within cementitious composites. Pozzolanic materials, such as fly ash and silica fume, contain amorphous silica, which reacts with calcium hydroxide (CH) and consumes it, thereby reducing the pH of the matrix [3].

The incorporation of pozzolans also contributes to enhancing the strength of the matrix due to the formation of calcium silicate hydrate (C-S-H) in the pozzolanic reaction. C-S-H is the main reaction product responsible for the strength

of concrete [3]. Furthermore, mineral admixtures enhance the bond between the fabric and the matrix, as some studies have observed densification around the textile area [13,74]. Nevertheless, it is worth noting that the addition of pozzolanic materials, mainly silica fume, should be limited to a maximum proportion of 10% by mass of the total cement content, as a reduction in workability has been observed when higher amounts of silica were incorporated [7].

2.2.1. Fiber reinforced concrete as TRC matrix

When subjected to elevated loads, TRC presents a brittle failure mode, mainly due to the absence of plastic deformation of the materials employed as reinforcement (notably AR-glass and carbon fibers) [7]. The incorporation of discrete fibers into the cementitious matrix is a relatively simple technique to modify this behavior, as short fibers can easily be added during mixing. The random and dispersed distribution of short fibers within concrete helps control crack propagation once the matrix reaches its tensile strength. By connecting the open cracks, the dispersed fibers enable stress transfer between the textile reinforcement and concrete [75]. In this way, the concrete contributes to the loading capacity even after its tensile strength is surpassed. This mechanism, known as “bridging effect”, allows for an increase in the first-crack stress and better cracking patterns [25,76–78], imparts a pseudo-ductile behavior to the composite and enables higher energy absorption [79].

Nevertheless, the effect of fiber addition on the ductility and overall mechanical behavior depends on the volume fraction, type of fiber and fiber-matrix interface. At low volume fractions, the contribution of short fibers to the ductility of the TRC composites is limited. Du *et al.* [80] observed that the incorporation of short steel fibers in a volume fraction of 0.8% did not lead to a significant improvement in the peak stress and strain capacity of TRC. Barhum and Mechtcherine [77], on the other hand, reported a decrease in the tensile strength and strain capacity of the TRC composites with the addition of carbon and AR-glass fibers in a volume fraction of 0.5%. However, the authors observed that the increase in the volume fraction to 1.0% resulted in an expansion of the multiple-cracking stage; the width of this region was more than doubled in the case of carbon fibers.

An increase in the energy absorption was observed due to the addition of short fibers. The work-to-fracture increased by almost 40% for the composites made of the matrix with the addition of both short fibers. The incorporation of short fibers improved the textile-matrix bond by a cross-linking mechanism.

Regarding the type of fiber, Zhu *et al.* [81] reported that short carbon, glass, and steel fibers contribute differently to reinforcing mechanisms. On the one hand, carbon and glass fibers enhanced interfacial bonding through the formation of cross-links between the matrix and textile, increasing the ultimate load of TRC due to their larger aspect ratios. On the other hand, steel fibers, with a smaller aspect ratio, showed limited bonding but improved the stiffness by restraining yarn slippage and improving the coordination between textile layers. The authors noted a decrease in the multiple-cracking behavior of the composites when the volume content of carbon fibers increased, attributing it to the brittleness and fracture of the fibers in the mixed concrete, as well as to the insufficient length of the fibers to enable a bridging effect.

In addition to enhancing ductility, the addition of short fibers can also modify and improve the failure mode of the composites depending on the volume fraction. Deng *et al.* [25] reported that when the volume content of PVA fibers was lower than 1.5%, the failure mode of carbon TRC composites was characterized by slippage of textiles in the gauge length in uniaxial tensile tests. The authors found that for volume fractions of 1.5% and 2.0%, failure occurred due to the fracture of the textiles, indicating that the short PVA fibers provided additional reinforcement of the interface and improved the interface bonding of the textile-matrix. Dong *et al.* [27] observed that the incorporation of short Polyvinyl Alcohol (PVA) fibers in AR-glass TRC avoided spalling upon the composite's failure. Pham *et al.* [78] found that the addition of short PVA fibers in a volume fraction of 1.2% in carbon TRC improved textile-matrix bond strength, as the detachment of the textile from the concrete layers was mitigated. In flexural tests, Dinh *et al.* [82] noted that the increase in the fiber volume fraction of PVA fibers from 0.8% to 1.2% delayed delamination between the carbon fabric and the cementitious matrix.

The combination of special types of Fiber Reinforced Concrete (FRC) with textile reinforcements can be interesting in special structural applications or special conditions. In the case of structures that might be subjected to large deformations, for example, the use of Strain-Hardening Cement-based Composites (SHCC) in

replacement to the conventional fine-grained concrete matrix is an interesting option [83]. SHCC, also known as Engineering Cementitious Composites (ECC), is a special class of FRC that employs discrete PVA or ultra-high molecular weight polyethylene fibers in relatively high volume fractions, generally around 2.0%, in order to achieve a pseudo strain-hardening behavior with the formation of multiple cracks when subjected to tensile stresses [84]. This composite is known for its unique ability to withstand large deformations and presents high ductility. Previous studies [85–88] have reported improvements in the tensile strength, strain capacity, energy absorption, and crack control of TRC composites with SHCC matrices.

In terms of durability requirements, behavior in the Serviceability Limit State (SLS), and structural performance, the employment of Ultra-High Performance Concrete (UHPC) matrices in TRC is a promising alternative. UHPC stands out for its ability to achieve elevated compressive strengths of at least 120 MPa, according to the ASTM Standard C1856/C1856M [89]. Such high strengths can be achieved due to the high dosage of cement, typically greater than 700 kg/m^3 [90], reduced water-cement ratio, and optimized granular packaging [91]. The formulation of UHPC usually includes cement, water, fine-grained sand, fine-grained materials such as silica fume, quartz powder and fly ash, and superplasticizers [91,92]. Furthermore, short steel fibers with a volume fraction up to 2% are frequently utilized to improve the tensile strength of ultra-high performance concrete [91]. In addition to high compressive strengths, the dense granular packing nature of this concrete yields elevated durability and impact resistance [93].

While the mechanical behavior of UHPC under quasi-static and dynamic loads has been studied by many authors, its combination with textile reinforcements and its influence on the mechanical performance of TRC has been less investigated. Mészöly *et al.* [94] studied the flexural behavior of UHPC plates with AR-glass and carbon textile reinforcements. The authors observed that the incorporation of steel fibers increased the first-crack stress, improved the crack behavior, and doubled the ultimate load of the specimens. However, the failure mode of the plates with textile reinforcement with the plain UHPC matrix was characterized by delamination, while those with short fiber incorporation did not present any delamination. Compared to the plain UHPC with steel fibers, the glass textile reinforcement only improved the load capacity of the composites with this matrix by 4%, whereas the

carbon fabric increased it by 65%. The low effectiveness of the glass fabric can be attributed to its low load-bearing capacity and stiffness.

Rossi *et al.* [95] evaluated the influence of overlapped joints on the behavior of TRC with a UHPC matrix. While the assessment of the effect of the UHPC matrix on the mechanical performance of TRC was not substantial, the authors found that the addition of short steel fibers into the matrix increased the performance of the composites with respect to out-of-plane deformation by achieving a higher stiffness with the prevention of a diffused crack pattern.

Yao *et al.* [96] investigated the tensile behavior of carbon, basalt, and AR-glass textile reinforcements with UHPC matrices with different volume fractions (0.5, 1.0, 1.5, and 2.0%). The effect of the number of textile layers (four and six) was also assessed. The results showed that, as the fiber volume fraction increased, higher first-crack stresses and tensile strengths were observed for the three types of textile reinforcements. The subsequent increase in the number of reinforcement layers also led to an improvement in tensile strength. The post-cracking stiffness, tensile strength, and ductility of the composites were directly influenced by the type of fabric. While the carbon fabrics presented lower reinforcement ratios (0.17 and 0.25% for 4 and 6 layers, respectively), the composites with these textiles presented the highest ultimate strength among the other series. The authors noted that while the strain capacity of the specimens with carbon textiles decreased with higher fiber volume fractions, the series with other textiles exhibited the opposite trend. In terms of crack width, most specimens presented lower maximum crack widths at failure than those specified by the design guidelines, indicating the improved potential of combining UHPC matrices with textile reinforcements in terms of durability requirements.

2.3. Textile reinforcement

The fabrics usually used as reinforcement in TRC consist of multifilament yarns arranged in different directions, forming a mesh structure with a determined opening [97]. A multifilament yarn (bundle), in turn, is composed of thousands of continuous fiber filaments grouped together [61]. A yarn is usually characterized by its fineness in tex, which is defined as the weight in grams of 1000 m of yarn

[79]; that is, 1 tex is equal to 1 g/1000 m. The fineness of a yarn depends on the number of filaments, the average diameter of the filaments, and fiber density [7].

The basic structure of textiles can be divided into warp and weft [61]. In technical fabrics used as reinforcement in composite materials, warp refers to yarns arranged in the longitudinal direction of the fabric, usually placed in the load direction, whereas weft refers to yarns in the transverse direction [10]. The method by which the warp and weft yarns are connected determines the resulting fabric type, geometry, and mesh opening [61]. Among the main fabric architectural types, one can cite woven, knitted, and bonded fabrics [61], that are differentiated in methods of yarn connection.

Woven fabrics (Figure 2.4a) are produced by interlacing two sets of perpendicular yarns at a right angle with the alternation of one crossing over and under the other, resulting in a characteristic wavy structure [61]. Woven fabrics with a mesh opening are created using a special technique known as leno weave. In the leno weave technique, fabrics are produced by twisting two warp yarns around the weft yarns (Figure 2.4b) [61]. In contrast, knitted fabrics are created by connecting yarns in loops rather than interlacing them. Although warp knitting and weft knitting are the two main methods used to produce these fabrics, weft-knitted fabrics (Figure 2.4c) are not typically used as reinforcements because of the high curvature of the final fabric shape. Warp-knitted fabrics (Figure 2.4d), on the other hand, offer better structural stability and can be manufactured with different mesh openings and structures [7,61]. Bonded fabrics (Figure 2.4e), in turn, are manufactured by connecting two perpendicular sets of warp and weft yarns with glue or by heating. This technique allows the production of fabrics with several mesh openings, due to the strong bond at the connection points [61].

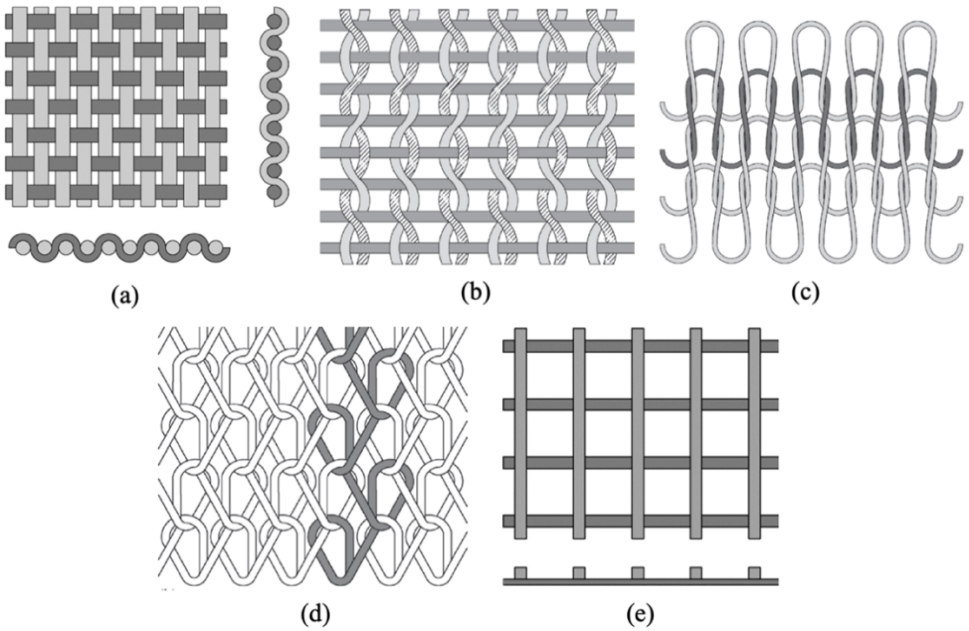


Figure 2.4 - Different types of fabric structures: (a) woven: plain weave, (b) woven: leno weave, (c) weft-knitted, (d) warp-knitted, and (e) bonded (adapted from [61]).

The geometry of the textile reinforcement influences the mechanical behavior of the TRC composites. When combined with cementitious matrices, woven fabrics and fabrics with more complex geometries, such as short weft knitted fabrics, tend to improve the mechanical behavior of the composite due to the additional mechanical anchoring provided by these structures [38,98,99]. Moreover, the use of bulky (3D) structures instead of flat (2D) fabrics allows the textile reinforcement to resist stresses both within the plane and in the perpendicular direction [97,100], thereby improving the mechanical performance of TRC. Figure 2.5 shows the 3D fabric structure.

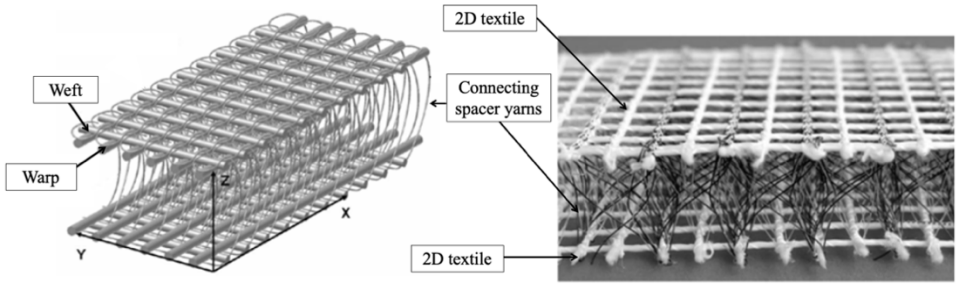


Figure 2.5 - 3D textile structure (adapted from [101]).

Fabrics can be made from a range of fiber types, which can be man-made or of natural origin. Carbon [25,74,102–104], alkali-resistant (AR) glass [20,23,24],

and aramid [105] are the main types of man-made fibers employed in the manufacturing of textile reinforcements. In the case of natural fibers, several authors have investigated the use of sisal [67,106,107], curauá [108,109], jute [22,72,110], and flax [71,111,112] textile reinforcements in TRC composites. Evidently, different types of fibers present different properties; therefore, the mechanical properties of the textile and the resulting composite are significantly influenced by the fiber material.

Carbon fibers stand out for their high tensile strength, modulus of elasticity, and durability. Additionally, these fibers present low coefficient of thermal expansion, low specific weight, and alkali resistance [12,75], making them particularly interesting for the use in the production of textile reinforcements for cementitious matrices [9].

Despite the aforementioned advantages, carbon fibers present low bond with cementitious matrices due to their hydrophobic nature [11]. Moreover, these fibers are usually found in tows, and one of the biggest challenges in using fabrics composed of multifilament yarns is the achievement of efficient stress transfer between the matrix and reinforcement [7]. In this way, in order to improve the bond with the matrix and achieve a more uniform stress distribution within the yarns [97], the fabrics are coated with polymers or mineral-based materials. Epoxy resin, acrylate and Styrene-Butadiene Rubber (SBR) are the most commonly used coating materials [113]. These materials result in fabrics with substantially different properties and bond with the cementitious matrix [113,114].

In terms of handling, epoxy resin impregnation presents a major disadvantage as it results in very stiff textiles, which limits one of the main characteristics of textile reinforced concrete: its versatility. SBR coatings, on the other hand, provide flexible fabrics [15], and therefore, are preferred in applications where design flexibility is required to create complex geometries or for retrofitting. However, as will be discussed in Section 2.4, TRC composites with textile reinforcements coated with SBR exhibit a significant inferior performance than those with epoxy-coated fabrics [103,104,115].

Alternative coating materials and techniques have been studied in order to achieve design flexibility in TRC. In a study conducted by Heins *et al.* [18], the use of thermoplastic resins as impregnation materials [18] was proposed. Thermoplastic polymers offer the possibility of easy reshaping of textile reinforcements with the

application of thermal energy due to the absence of chemical cross-links in their molecular structure. The lack of cross-linked structures allows thermoplastics to soften when heated and return to a solid state upon cooling, making it possible to reshape the textile reinforcements as desired. The effect of two thermoplastic impregnations (an aqueous polyacrylate dispersion and an aqueous polystyrene dispersion) on the mechanical behavior of AR glass fabrics was analyzed by Heins *et al.* [18]. The authors reported that both materials led to ultimate tensile strengths comparable to those achieved using traditional coating materials such as epoxy and SBR, demonstrating the potential of thermoplastic coatings. Nevertheless, the effect of such impregnation materials on the bond with the cementitious matrix and the mechanical behavior of TRC composites remain to be investigated.

Scheurer *et al.* [17] explored a pre-impregnation (prepreg) approach for the obtention of drapable fabrics. According to the authors, this technique consists of coating the fabrics and embedding them into concrete before the curing process of the impregnation material happens. Since the curing process of the coating occurs after the textiles are embedded in the concrete matrix, the flexible properties of the textiles are retained, even when using materials that result in stiff textiles, such as epoxy resins, allowing its use to cast elements with complex geometries, and in new manufacturing processes such as oricrete, 3D printing and extrusion [17]. Figure 2.6 shows an example of a folded textile obtained using the prepreg method.

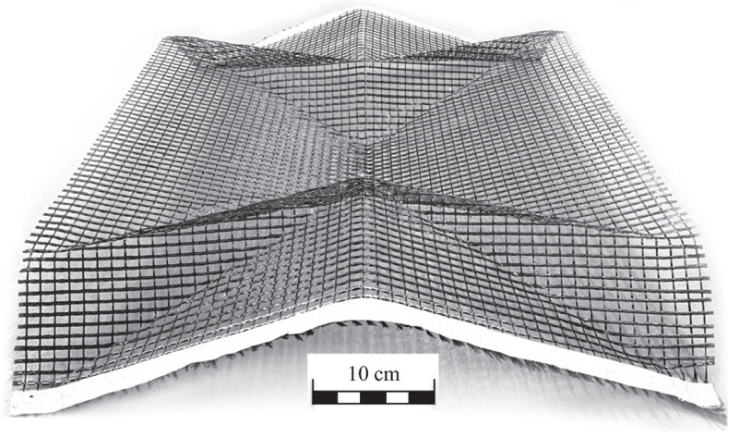


Figure 2.6 - Design flexibility of textile fabric obtained using the prepreg approach [116].

2.4. Fiber-matrix interface

As a composite material, the mechanical behavior of textile reinforced concrete depends not only on the cementitious matrix and textile reinforcement, but also on the bond between these two phases [113]. The interfacial bonding characteristics between the textiles and cementitious matrix play an essential role in the performance of TRC, influencing the stress transfer from the concrete to the reinforcement, and consequently, the strength and ductility of the composite [7].

As mentioned earlier, the textile reinforcements are formed by bundled yarns consisting of thousands of fiber filaments assembled in parallel [61], as Figure 2.7 illustrates. Due to the size incompatibility between the diameter of the cement grains, which typically ranges from 10 to 70 μm, and the spaces between filaments, which are usually smaller than 5 μm, the cementitious matrices are unable to penetrate within the yarns and fill the intrafilamentary spaces [75]. As a result, only the outer filaments are in direct contact with the matrix and thus, properly anchored, whereas the filaments located closer to the core are relatively free within the strands [7]. The lack of anchorage of the inner filaments significantly compromises the mechanical performance of TRC composites because these filaments are unable to engage adequately upon loading; therefore, they do not contribute to the load-bearing capacity of the material. This prevents the full use of the mechanical properties offered by high performance fibers, such as carbon and AR-glass. Furthermore, in the case of carbon-based fabrics, the inherent hydrophobic nature of carbon fibers [11] is another factor that further compromises the bond with the hydrophilic cementitious matrix.

The stress distribution within the yarn and the bond of multifilament yarns towards the cementitious matrix can be improved through polymeric impregnations [114]. Unlike cement particles, polymers are able to penetrate the extremely narrow spaces inside the yarn, enabling the activation and stress transfer between the inner filaments, thereby improving the mechanical performance of the TRC composites. High penetration capacity (usually obtained with lower viscosities), high strength in the cured state, high durability, and temperature resistance are some of the properties polymers should present to be suitable for use as coating material [18]. Besides polymeric coatings, mineral-based materials [23,107,117] can be used to

impregnate the fabrics. Mineral impregnations are particularly interesting for applications that require high thermal resistance, as most polymers usually present low thermal glass temperature transition [118].

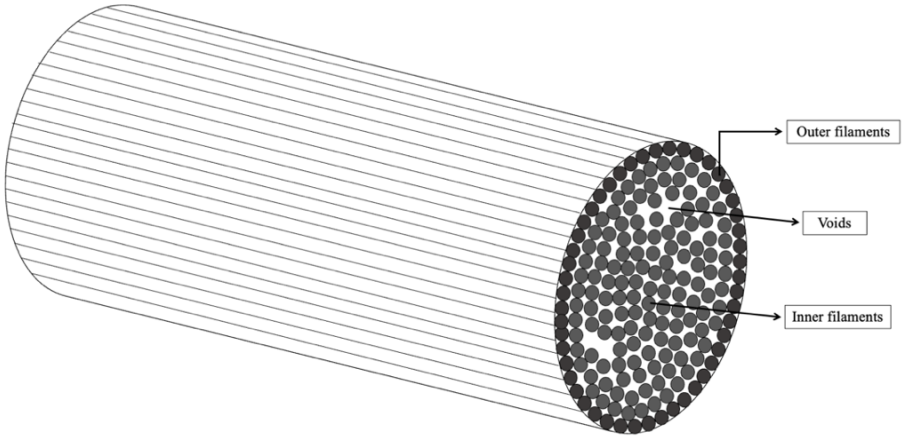


Figure 2.7 - Multifilament yarn.

The type of polymeric coating has a direct influence on the mechanical performance of TRC, as different polymers present different chemical compositions and penetration capacities, making the bond of the reinforcement towards the concrete matrix and the stress distribution vary considerably, as can be seen in Figure 2.8. Styrene-butadiene rubber (SBR) coatings, for example, result in composites with inferior mechanical performance compared to other polymer systems, such as epoxy [103] and acrylate [104]. The inferior behavior of TRC with SBR-coated textiles can be attributed to the low bond of this material with the matrix, which is mainly composed by friction, due to a lower impregnation level (see Figure 2.8b), and a superficial chemical bond [113]. Previous studies [78,103,104] have demonstrated that the mechanical response of such composites can be improved by the use of a subsequent coating of SBR-coated fabrics with epoxy and sand. Acrylate coatings present a better bond with the concrete matrix and thus, these coatings result in composites with better performance than SBR; however, their performance is inferior to that of epoxy resin coatings [119].

Typically, solvent-based epoxies are used to impregnate the textiles. Although the impregnation of the fabrics with these epoxies yields TRC composites with higher mechanical properties than SBR and acrylate due to a better stress distribution inside the yarn (Figure 2.8c), prior research [13,14] have reported

delamination between the textile and concrete layers, an indication of a low chemical bond. The opposing nature of hydrophobic solvent-based epoxy coatings and the hydrophilic cementitious matrix can lead to a reduction in water absorption at the fiber-matrix interface [120], causing delamination to occur during tensile loading [13]. While some authors [78,102,103,115] have demonstrated that the use of an additional sand coating on epoxy-impregnated fabrics improves the textile-matrix bond and thus avoids delamination issues, this method does not address the deficient chemical bond. In this way, a possible alternative to improve the chemical bond is the use of water-based epoxies.

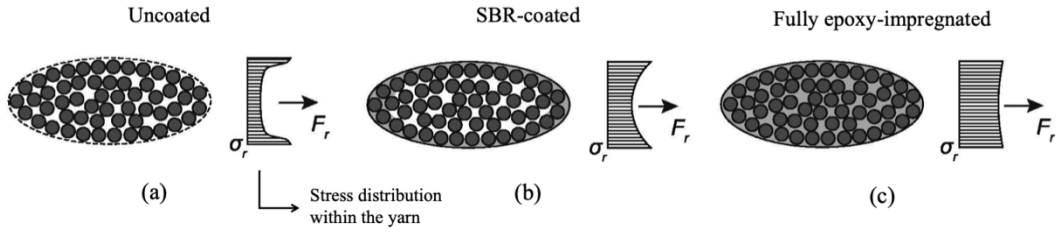


Figure 2.8 - Stress distribution within the yarn of (a) uncoated fabrics, (b) SBR-coated fabrics, and (c) fully epoxy-impregnated fabrics (adapted from [115]).

In a previous study, Scheurer *et al.* [17] evaluated the effect of a water-dispersed epoxy impregnation on the mechanical behavior of TRC. In uniaxial tensile tests, the results obtained for specimens with water-based impregnation cured before and after embedment in concrete (utilizing the aforementioned prepreg approach) were compared. The authors found that the water-based epoxy coating cured before casting yielded an average increase of 165% in the maximum load of the composites compared to the uncoated reference, whereas the composites in which curing occurred inside the cementitious matrix exhibited an average increase of 87%. Carbon rovings coated with solvent-based epoxy resin cured prior to embedment, in turn, presented an increase of 185% in ultimate load in comparison with non-impregnated ones, while those cured within concrete demonstrated an increase of 85%. Compared to the solvent-based epoxy, the waterborne epoxy cured before casting presented a difference in the average ultimate strength of only 7.41%. In the case of the composites with the cured inside coating, the water-based epoxy presented a slight increase in mechanical performance in relation to the epoxy resin. While these results indicate that the water-based epoxy coatings could be an

alternative to the solvent-based epoxy, further investigation into the use of this type of epoxy coating in TRC, at the material and structural levels remains to be done. Furthermore, as the prepreg method could be an easier way to obtain design flexibility even when utilizing coating materials that do not initially allow it, as the waterborne epoxy, further evaluation of this method should be conducted.

2.5. Structural behavior of TRC beams

The use of textile reinforced concrete in the manufacturing of new structural elements has attracted considerable attention in the last decade. In this way, the flexural behavior of textile reinforced concrete beams with different cross-sections and reinforcement layouts has been evaluated by several authors [103,121–126].

Silva and Silva [103] investigated the structural performance of rectangular carbon TRC beams in four-point bending tests. The influence of the addition of dispersed steel fibers to the matrix was also investigated. It was noted that the TRC beams without steel fibers and reinforcement only in the longitudinal direction exhibited load capacities comparable to steel RC beams with 6.3 mm and 8 mm reinforcing rebars, whereas carbon TRC beams with steel fibers achieved load capacities similar to those of RC beams with 10 mm reinforcing bars. The beam that combined longitudinal and transversal reinforcement surpassed the maximum load of an RC beam with 10 mm reinforcing rebars. However, it was observed that the carbon TRC beams exhibited less ductile failure due to the fragile nature of the carbon fabrics and their lack of yielding characteristics. Despite this limitation, both carbon TRC and RC beams showed comparable load-displacement behavior at displacement levels suggested by serviceability limit states in current design standards, indicating that carbon TRC beams could be viable alternatives to RC beams in many practical applications.

Nahum *et al.* [121] evaluated the flexural behavior of carbon TRC rectangular beams with different shear reinforcements (steel rebars and U-shaped carbon fabrics). The beams with the steel rebars as shear reinforcement presented severe delamination between the textile and the concrete layer, leading to a premature failure as the delamination occurred before the total load-bearing capacity of the textile reinforcement could be achieved. In contrast, the beams with U-shaped

fabrics did not exhibit delamination and thus presented a higher load-bearing capacity at failure.

Although the previous studies [103,121] have demonstrated the feasibility of carbon TRC at a structural level, the possibility of utilizing the corrosion resistance of the reinforcements to cast very thin elements in various cross-sections, such as thin I- and T-sections, was not thoroughly explored. Goliath *et al.* [126] studied the flexural behavior of carbon TRC I-section beams. The influence of an SHCC matrix and surface sand-coating of the SBR-impregnated carbon fabrics on the structural performance of TRC beams was assessed. The use of sand-coating and an SHCC matrix improved the web-flange junction, avoiding premature failure by shear. It was observed that the sand-coating improved the flexural behavior of the TRC beams in terms of strength and stiffness. While the SHCC matrix presents lower compressive properties, the authors found that the beam with SHCC matrix showed improved crack control, and enhanced stiffness in the cracked state, besides exhibiting apparent ductility due to concrete softening mechanisms.

Despite the several advantages of textile reinforcements, the brittle failure mode of the TRC is considered a limitation in the application of this material in structural elements. In this way, to improve the performance and ductility of TRC beams, the combination of carbon textile reinforcements with other types of reinforcements has been investigated. Valeri *et al.* [122] evaluated the bending and shear response of long carbon TRC I-section beams with high-strength stainless steel rebars in the flexural area in addition to the carbon fabric and with only carbon textiles. The cross-sectional dimensions and reinforcement configuration employed by the authors are shown in Figure 2.9. Although the addition of steel rebars significantly improved the load-bearing and deformation capacity of the beam, both beams exhibited brittle failure. In the case of the carbon TRC beam, it failed primarily due to bending, with the rupture of the longitudinal reinforcement in the bottom flange. In contrast, the beam with the hybrid reinforcement failed as a result of a combined crushing of the web and sliding along delamination cracks. The failure mechanism of this beam involved the formation of four local plastic hinges in the flanges and a quasi-vertical crack, which allowed for the relative sliding of the web with respect to the top flange.

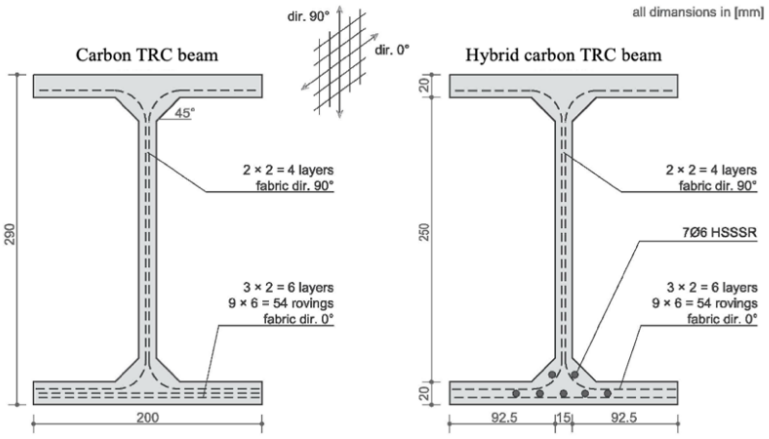


Figure 2.9 - Reinforcement configuration, cross-section dimensions, and test setup used by Valeri, Ruiz, and Muttoni [122].

A combination of carbon and AR-glass textiles as well as carbon Fiber Reinforced Polymer (FRP) bars were used as reinforcements for large-scale I-shaped beams in a study conducted by Bielak *et al.* [123]. Carbon FRP bars were used as the main bending reinforcement (AR-glass textiles were also used in the tensile zone) and carbon fabrics were used for shear and flange reinforcement (Figure 2.10). The authors found that textiles serve as highly effective shear reinforcements for I-beams with large depths, creating a dense crack pattern while efficiently bridging the shear cracks. Moreover, carbon FRP bars and carbon textiles demonstrate strong compatibility when the strain limits of different reinforcement types are considered in the design.

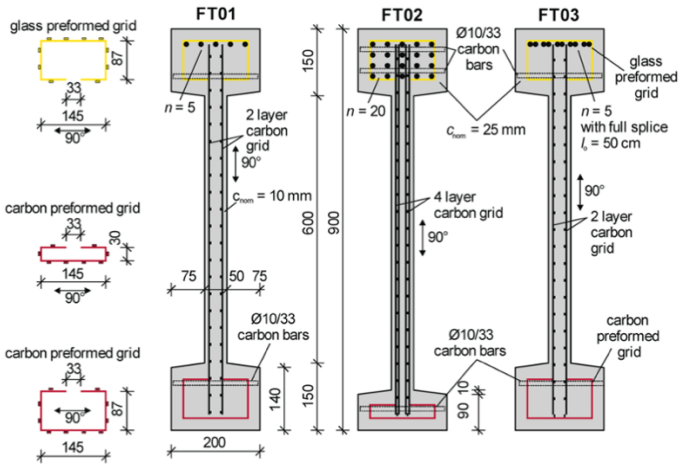


Figure 2.10 - Reinforcement configurations and I-section dimensions analyzed by Bielak *et al.* [123].

The shear behavior of carbon TRC T-beams with a UHPC matrix was investigated by Preinstorfer *et al.* [124]. Hybrid reinforcement configurations, consisting of carbon FRP rods and textiles, were used (Figure 2.11). The authors noted that the shear strength varied depending on the web and flange thickness, type of textile reinforcement, and whether or not prestress was applied to the CFRP rods. It was observed that the shear-carrying capacity improved with thicker web and flange. Regarding the type of textile reinforcement, two types of impregnation materials were used for the carbon fabrics: acrylonitrile-styrene-acrylate copolymers (ASA) and epoxy resin. In both cases, the total tensile strength of the fabrics could not be fully utilized. While the ASA-impregnated textiles exhibited reduced tensile strength due to non-axial loading, epoxy-impregnated textiles experienced early failure due to concrete cover spalling in the web. The use of prestress on the CFRP rods proved to be particularly effective because a 44% increase in the shear capacity was observed for a relatively small prestressing force.

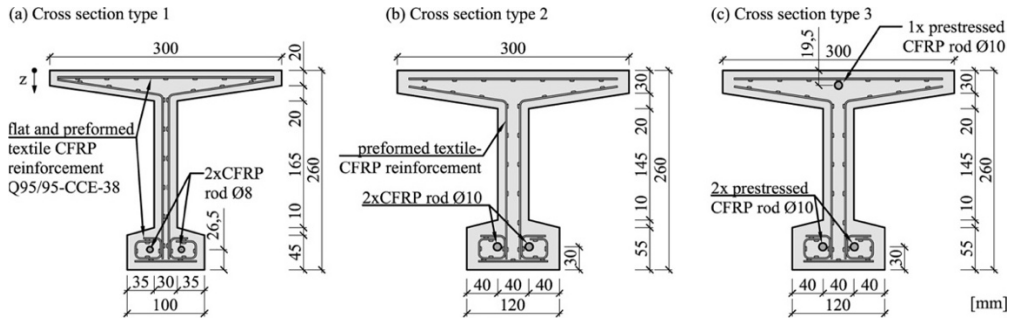


Figure 2.11 - T-beams cross-sections and reinforcement configurations evaluated by Preinstorfer *et al.* [124].

3
Experimental Program

3.1.
Introduction

This chapter aims to present the materials used in the production of the specimens, describe the specimens manufacturing and detail the testing procedures.

3.2.
Materials

3.2.1.
Cementitious matrices

Two types of cementitious matrices were used in this study: a fine-grained concrete and an ultra-high performance concrete (UHPC). In this section, the compositions and mixing procedures of the matrices are described. Moreover, the characterization of the matrices through compressive tests to assess their mechanical properties is detailed.

3.2.1.1.
Fine-grained concrete

The fine-grained concrete, here named conventional matrix, was the same used by Silva [15]. With a mix proportion of 1:1:0.3 (sand: cement materials: water), the matrix consisted of dry materials (sand, cement, mineral additives), water, and a superplasticizer. Industrial sand produced by Jundu with a maximum particle diameter of 1.20 mm [127] was utilized as fine aggregate. Portland cement type CP-II F 32 (ASTM Cement type IL – Portland-Limestone Cement [128]), defined by the Brazilian Standard ABNT NBR 16697 [129], was used. Fly ash from Pozofly® and silica fume from Tecnosil were incorporated as mineral admixtures. To improve the workability of the concrete during casting, a superplasticizer, MasterGlenium® 51 from BASF, with a solid content of approximately 30%, was incorporated. The matrix composition can be seen in Table 3.1.

Table 3.1 - Fine-grained concrete composition [15].

Industrial sand (0-1.20 mm) (kg/m^3)	947.0
Cement CP-II F 32 (kg/m^3)	632.0
Water (kg/m^3)	280.8
Fly ash (kg/m^3)	265.0
Silica fume (kg/m^3)	50.5
Superplasticizer (kg/m^3)	4.74

- **Mixing processes**

The mixing of the fine-grained concrete matrix was carried out in a 20-liter planetary mixer (Amadio model 20LA) for the manufacturing of the composites. The mixture procedure was conducted as described by Silva [15]: first, the dry materials were mixed for one minute at speed one (125 rpm). Then, approximately 90% of the water content was added, and the mixture proceeded for four minutes, with the first 15 seconds at speed one and the remaining time at speed two (220 rpm). Finally, the superplasticizer, previously mixed with 10% of the remaining water content, was incorporated. The mixing continued for five minutes, in which the first 15 seconds were at speed one, followed by another 15 seconds at speed two, and the remainder at speed three (450 rpm).

To produce the structural elements, a 40-liter concrete mixer was used to prepare the fine-grained concrete matrix. The mixture process occurred as follows: initially, the dry materials were stirred for one minute. Then, approximately 90% of the water was incorporated, while mixing, and the mixture continued for five minutes. Subsequently, the superplasticizer and the remaining 10% of water were gradually added, and the materials were mixed for six more minutes.

3.2.1.2. Ultra-high performance concrete

The mix proportion of the ultra-high performance concrete matrix utilized was developed by Santos [127]. Industrial sand, with a limited particle size of 1.20 mm, was used as fine aggregate. Cement CP-V ARI RS (ASTM Cement type III [128]), a high initial resistance cement type defined by the Brazilian Standard ABNT NBR 16697 [129], was utilized. Fly ash from PozoFly®, silica fume 920U and quartz powder SM325 from Elkem were added as mineral admixtures. The

superplasticizer MasterGlenium® 51 from BASF, with a solid content of approximately 30%, was incorporated to improve the workability of the concrete during casting. Short steel fibers (Figure 3.1) produced by Ganzhou Daye Metallic Fibres Co. were used in a volume fraction of 2% (corresponding to 157 kg/m^3 by weight). The main properties of the steel fibers can be seen in Table 3.2. Table 3.3 shows the UHPC composition.

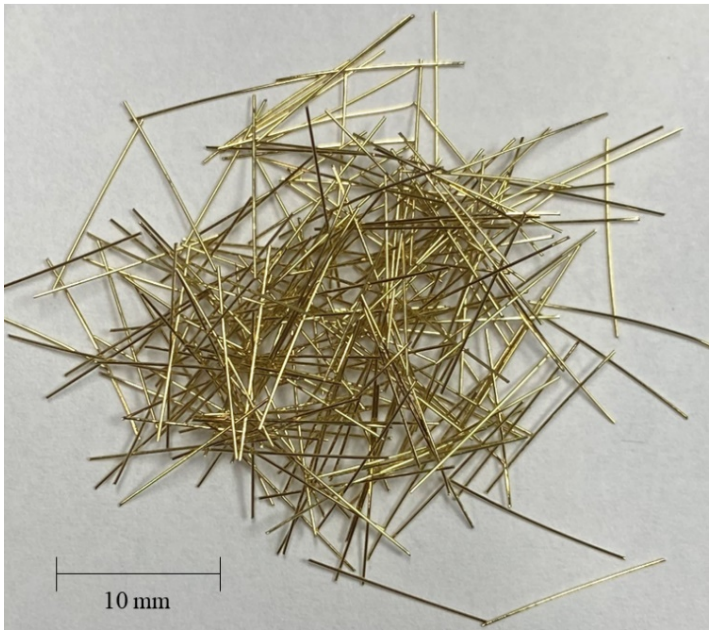


Figure 3.1 - Steel fiber used in the UHPC matrix.

Table 3.2 - Steel fiber properties (according to the manufacturer).

Length (mm)	13.0
Diameter (mm)	0.12
Aspect ratio	108.0
Tensile strength (MPa)	2850
Modulus of elasticity (GPa)	210.0

Table 3.3 - Ultra-high performance concrete composition [127].

Industrial sand (0-1.20 mm) (kg/m^3)	846.2
Cement CP-V ARI RS (kg/m^3)	800.0
Water (kg/m^3)	166.2
Fly ash (kg/m^3)	80.0
Silica fume (kg/m^3)	80.0
Quartz powder (kg/m^3)	200.0
Superplasticizer (kg/m^3)	30.0
Steel fiber (kg/m^3)	157.0

- **Mixing procedures**

A planetary mixer (Amadio model 20LA) with a maximum capacity of 20 liters was utilized for the mixing of the UHPC matrix to manufacture the composites. The process started with the dry materials being mixed for one minute at speed one (125 rpm). Half of the water was added, and the mixture proceeded for another minute at the same speed. The superplasticizer was then incorporated and blended for one minute at speed one. The next step consisted of the addition of the remaining water. The mixing continued for seven minutes, starting with the first 30 seconds at speed one, then another 30 seconds at speed two (220 rpm), and the remaining time at speed three (450 rpm). Finally, in the last step, the steel fibers were slowly added to the mixture to ensure an even distribution, and the mixing continued for two more minutes at speed one.

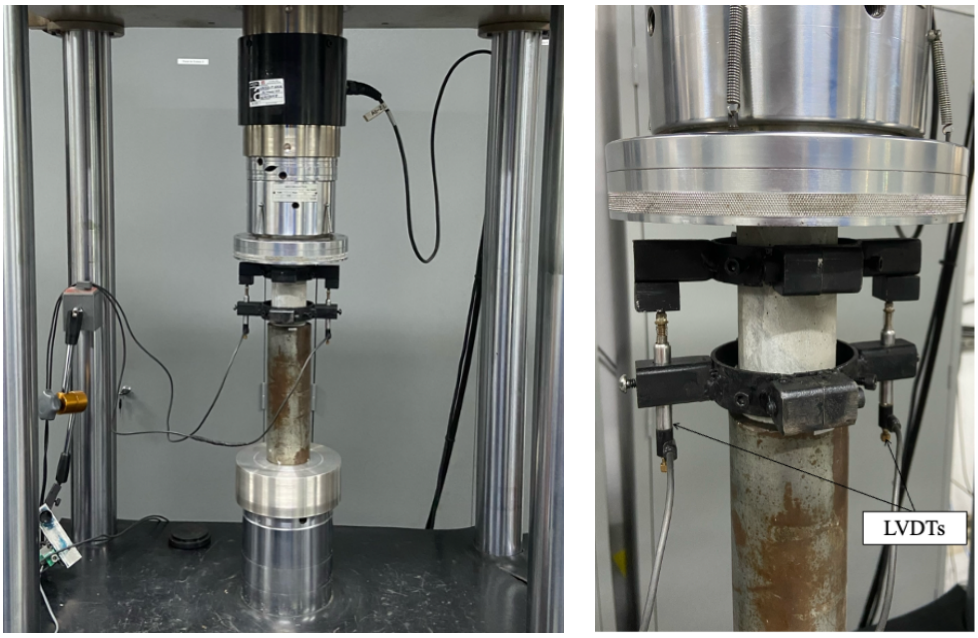
To cast the structural elements with the UHPC matrix, a 600-liter concrete planetary mixer (model Cibi M600) was used. The mixture process differed from the one previously described due to the mixing energy of the mixer. The procedure was carried out as described by Santos [127]: (i) the dry materials, with the exception of the cement, were mixed for five minutes; (ii) the cement was added to the mixture and it proceeded for five minutes; (iii) next, while the materials were stirred, the water and superplasticizer were gradually added for about one and a half minutes. After this, they were mixed for five minutes; (iv) the steel fibers were gradually added for about three minutes, in order to ensure an even distribution, and the mixture continued for five more minutes.

3.2.1.3. Mechanical properties of the matrices

The characterization of cementitious matrices was performed through compression tests to determine important properties of concrete in its hardened state, such as its compressive strength and modulus of elasticity. At least three cylindrical specimens with dimensions of 50 mm × 100 mm (diameter × height), according to the Brazilian Standard ABNT NBR 5738 [130], were cast for each matrix in order to assess their mechanical properties. A 5-liter mixer was used to mix the matrices. The mixing processes were carried out as described in Section 3.2.1.1, for the conventional matrix, and in Section 3.2.1.2, for the UHPC.

The compression tests were conducted on universal mechanical testing machines. An MTS model 810 with a load capacity of 500 kN and an MTS model 311 with a maximum load capacity of 1000 kN were used to test the conventional matrix and the ultra-high performance concrete specimens, respectively. The tests on both matrices were performed using displacement control at a rate of 0.2 mm/min. Both matrices were characterized at 28 days.

Two Linear Variable Displacement Transducers (LVDTs) with a 50 mm reading capacity were used to measure the displacement of the specimens during the test. The LVDTs were attached to the sides of the specimens using two plastic rings positioned approximately 20 mm from the ends: one at the top and the other at the bottom. Figure 3.2 shows the test setup.



(a) (b)

Figure 3.2 - Compression test setup (a) overview and (b) LVDT detail.

The compressive strength was calculated by dividing the measured load values obtained during the test by the cross-sectional area of the specimens (πr^2). The strain was calculated by dividing the arithmetic mean of the displacements measured by the LVDTs by the length covered by the LDVTs (60 mm). The modulus of elasticity for each matrix was obtained between 20% and 70% of the compressive strength.

Figure 3.3a and b present the compressive stress *vs.* strain curves of the fine-grained concrete matrix and UHPC matrix, respectively. The average values of the compressive strength ($\sigma_{c,max}$), strain at the corresponding compressive strength ($\varepsilon_{c,max}$), modulus of elasticity (E), and their standard deviations can be seen in Table 3.4 for both matrices.

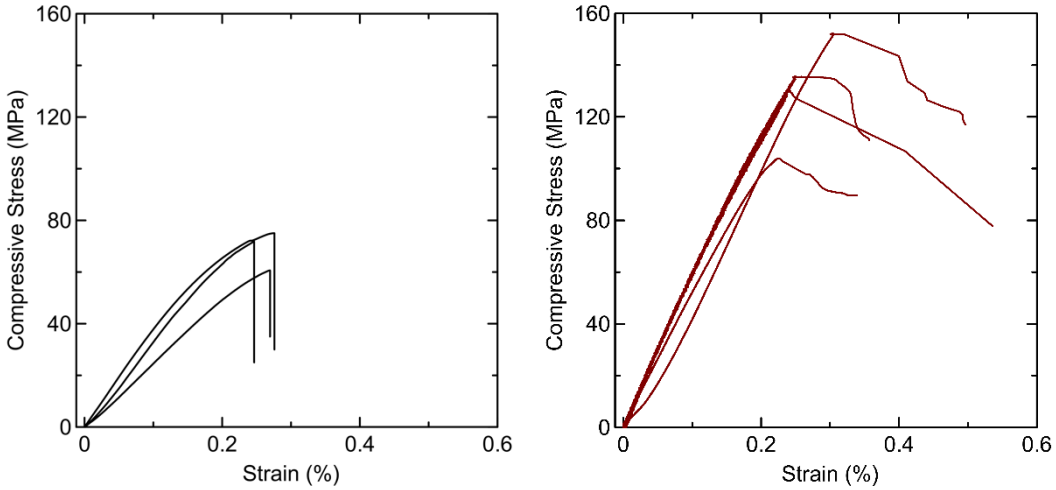


Figure 3.3 - Compressive stress *vs.* strain curves of the (a) fine-grained concrete and (b) ultra-high performance concrete.

Table 3.4 - Average compressive tests results of the matrices.

Matrix	$\sigma_{c,max}$ (MPa)	$\varepsilon_{c,max}$ (%)	E (GPa)
Fine-grained concrete	69.2 (6.18)	0.199 (0.112)	31.5 (4.17)
UHPC	130.6 (17.3)	0.283 (0.0786)	55.1 (1.70)

The average compressive strength and modulus of elasticity of the fine-grained concrete were 69.2 MPa and 31.5 GPa, respectively. These values are in accordance with those obtained by previous studies that utilized the same concrete matrix composition [103,104]. The UHPC matrix achieved a compressive strength of 130.6 MPa and a modulus of elasticity of 55.1 GPa. These results are also in accordance with those found by Santos [127].

3.2.2. Carbon textiles

Carbon textiles with three different coating materials were used to reinforce the composites and structural elements. The first fabric was a commercial carbon textile produced by Solidian GmbH coated with a traditional epoxy resin (GRID Q 140/110–CEP–13/17). The other carbon fabrics were provided by the Institut für Textiltechnik (ITA) of RWTH Aachen University. The second textile was initially received uncoated and later impregnated manually at the laboratory with a water-dispersed epoxy resin (see Section 3.2.2.1). The third fabric was coated with a thermoplastic resin, an aqueous polyacrylate dispersion with a solid content of 50%.

The impregnation process of the carbon textile with the thermoplastic coating was conducted at the ITA.

The mesh opening and mechanical properties of the epoxy-coated textile differed from those of the second and third textiles (see Figure 3.4). The second and third textiles were made of the same fabric, differing only in the coating material. The technical data of the commercial carbon textile from Solidian and the carbon fabrics provided by ITA are presented in Table 3.5 and Table 3.6, respectively.

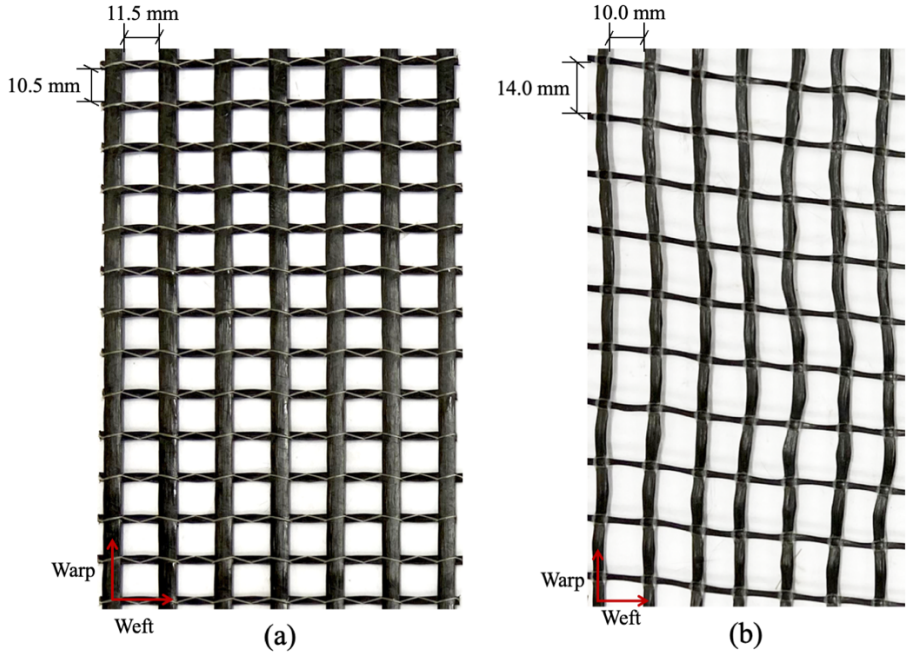


Figure 3.4 - Mesh opening dimensions of the (a) carbon fabric from Solidian and (b) carbon textile provided by ITA.

Table 3.5 - Technical data of the Solidian carbon textile (according to the supplier).

Coating material	Epoxy resin
Nominal cross-section of the strand* (mm^2)	5.44 ± 1.03 (warp) 3.85 ± 0.239 (weft)
Tensile strength (MPa)	2700
Modulus of elasticity (GPa)	270

*According to Silva [15].

Table 3.6 - Technical data of the carbon textiles provided by ITA.

Fineness (tex)	3200 (warp) 800 (weft)
Cross-section of the strand (mm^2)	1.78 (warp) 0.44 (weft)
Tensile strength of the roving (MPa)	4300
Modulus of elasticity of the roving (GPa)	240

3.2.2.1. Water-based epoxy coating process

As previously mentioned, the water-based epoxy coating was performed at the laboratory. For this, a water-dispersed epoxy resin from MC-Bauchemie (MC-DUR 1177 WV-A) was used to impregnate the uncoated textile provided by the ITA. This water-based epoxy resin (WBEP) consists of a base (A) and a hardener (B) component. According to the manufacturer [131], the mixing ratio by weight is 56:44 (base:hardener), and the working time of the resin is 60 minutes, considering the application at 20 ºC and 50% relative humidity. Table 3.7 presents the main technical properties of the WBEP resin obtained from the manufacturer's datasheet.

Table 3.7 - Technical data of the MC-DUR-1177 WV-A resin [131].

Mixing ratio (in weight)	56:44
Density (kg/dm^3)	1.05
Viscosity* (mPa.s)	250
Working time* (min)	60
Accessible after (h)	6
Full resistance (days)	7

*At 20ºC and 50% relative humidity.

In order to coat the textiles with the WBEP resin and achieve uniform level of impregnation across all composite batches, a fixed amount of resin needed to be defined. Scheurer *et al.* [17] used this same water-based epoxy and thus, the amount of resin to be used for the coating process was determined based on their study. An amount of 500 grams of resin per square meter of fabric was defined.

The impregnation procedure was performed manually at the laboratory as follows: the uncoated carbon textile was fixed onto a wooden frame measuring 600 mm × 1120 mm (width × length) using steel angle bars and screws (Figure 3.5a). To ensure the fabric remained straight during the coating process, the textile was stressed by hand in the longitudinal direction, as it was fixed to the frame. In a plastic container, the base component was weighed, and then, in the same container, the hardener was added at a mixing ratio of 56:44. Using a wooden stick, both phases were mixed until the resin was homogeneous, as specified by the manufacturer. After proper mixing, the resin was applied to the fabric using a paint

roller in the longitudinal direction (Figure 3.5b) and on both sides of the fabric (top and bottom). Once the resin was applied, the fabric was left to cure in the air. Before the desired curing time was reached (see Section 3.3.1), the fabrics were cut with scissors to the dimensions of the specimen.

The coating process of textile reinforcement for the beam with the waterborne epoxy was carried out exactly as previously described. The only difference was the length of the frame, which was 2100 mm, whereas the width remained the same (600 mm).

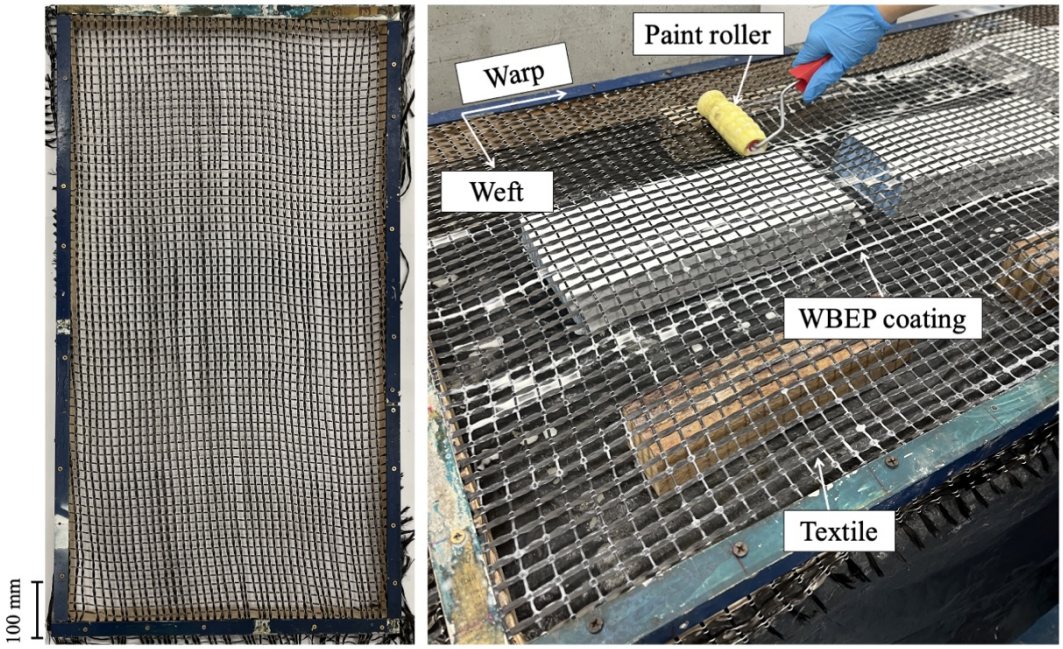


Figure 3.5 - (a) Wooden frame and uncoated textile, and (b) WBEP coating procedure.

3.3. Specimens manufacturing

3.3.1. Composite manufacturing

To investigate the mechanical behavior at the composite level, TRC composites were produced by varying the cementitious matrix and carbon textile. The matrices refer to the fine-grained concrete, here named conventional matrix (CONV), and the ultra-high performance concrete (UHPC) described in Sections 3.2.1.1 and 3.2.1.2, respectively. The carbon textiles are those presented in Section

3.2.2 coated with solvent-based epoxy (EPXY), water-based epoxy (WBEP), and thermoplastic resin (THRM). As described in Section 3.2.2.1, the WBEP coating process was carried out at the laboratory. Thus, the effect of three curing times on the mechanical properties of the composites was studied: four hours (04h), 24 hours (24h), and seven days (07d). Specimens with the uncoated fabric were also evaluated for comparison. The UHPC matrix was used only in combination with the EPXY-coated textile.

The curing time of the water-dispersed epoxy coating corresponds to the time the resin was left to cure in the air after the impregnation process before the composites were cast. These curing times were selected based on previous research [17] and the technical properties of the resin available in the manufacturer's datasheet. The four-hour curing time was chosen to study the mechanical behavior of the TRC composites using the prepreg method analyzed by Scheurer *et al.* [17]. In their study, carbon rovings were impregnated and immediately embedded into concrete. However, in the present study, a longer curing time was used due to the coating process, the time needed to prepare the fabrics for casting, and the need to preserve the fabric's geometry (mesh opening). As explained in Section 3.2.2.1, a larger frame (600 mm width) was used to coat the fabrics, and once the coating process was over, they had to be cut to the desired size by hand with scissors. With the resin still excessively wet, this process would be difficult, and the fabric's geometry would be compromised. The 24-hour curing time was also selected based on the study conducted by Scheurer *et al.* [17], who conducted rolling ball tests to assess the curing time of the resin by relating it to the tack of the impregnation material (higher tacks implying lower distances traveled by the steel ball, and thus, lower degree of curing). The authors conducted the test for several curing times and reported a higher and constant tack of the water-dispersed resin after 24 hours, indicating its cured state. In the case of the 7-day curing time, this age was chosen because it is the time required for the resin to achieve its full resistance, according to the manufacturer (see Table 3.7).

Figure 3.6 illustrates the identification system used in this study for the TRC composites. The nomenclature includes the type of matrix, coating material of the textile reinforcement, and curing time of the resin for composites with the WBEP-coated fabrics. Table 3.8 lists the test variables and the respective specimen identification.

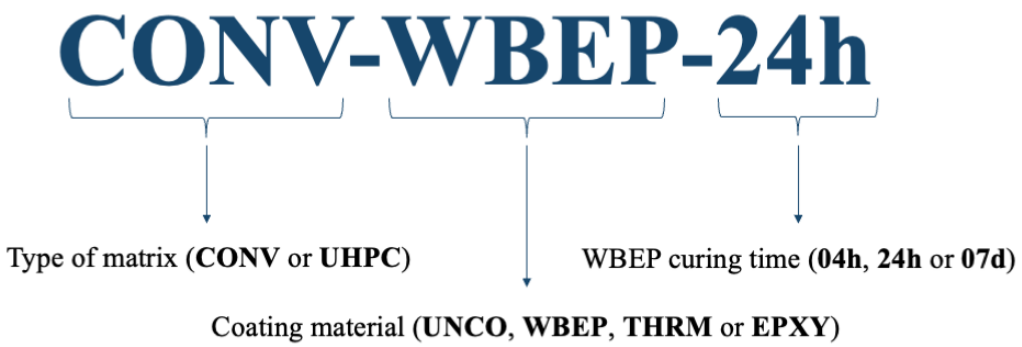


Figure 3.6 - Specimens identification system.

Table 3.8 - Test variables and specimen identification.

Matrix	Carbon textile coating	Curing time of the resin in air	Composite identification
Fine-grained concrete	-	-	CONV-UNCO
Fine-grained concrete	Water-based epoxy	4 hours	CONV-WBEP-04h
		24 hours	CONV-WBEP-24h
		7 days	CONV-WBEP-07d
Fine-grained concrete	Thermoplastic resin	-	CONV-THRM
Fine-grained concrete	Solvent-based epoxy	-	CONV-EPXY
Ultra-high performance concrete	Solvent-based epoxy	-	UHPC-EPXY

For the direct tensile tests, rectangular plates with dimensions of 1000 mm × 120 mm (length × width) and gauge length of 500 mm were cast according to the hand laminating technique [7]. The composite manufacturing process is illustrated in Figure 3.7, and was carried out as follows: a thin layer of cementitious matrix was poured into the mold (Figure 3.7b) and spread on it evenly using a putty knife (Figure 3.7c). Next, the textile reinforcement was positioned on top of the first layer of matrix (Figure 3.7d), and finally, the last matrix layer was added on top of it (Figure 3.7e). In order to induce the specimen's failure in the gauge length, two aluminum plates with a thickness of 1.50 mm were placed in the middle of the mold, one on the bottom (Figure 3.7a) and the other on top of the final matrix layer (Figure 3.7f) to reduce the cross-sectional thickness of the composites in this area. At least four specimens were produced for each composite type.

The use of the aluminum plates resulted in variations in the gauge-length thickness from one specimen to another and at different points within the same specimen. Thus, six thickness measurements were taken for each specimen using a

digital caliper, and the arithmetic mean of these values was calculated to obtain the average thicknesses. Table 3.9 shows the average thickness obtained for each composite type.

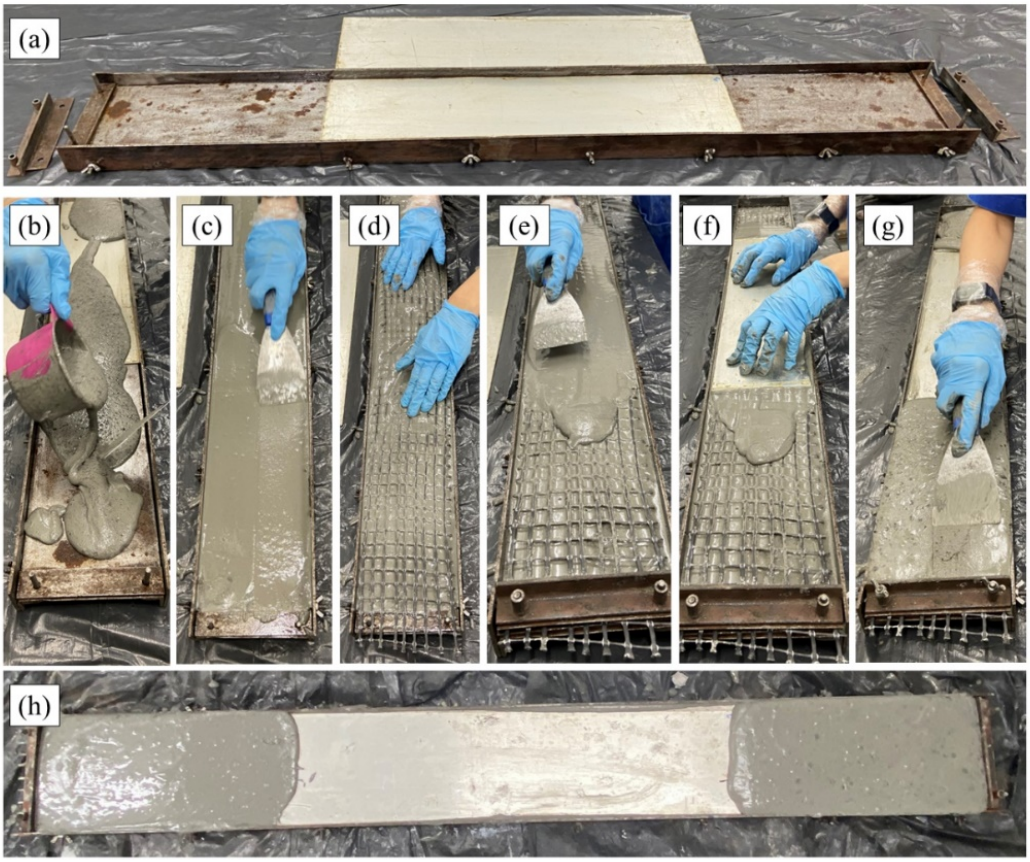


Figure 3.7 - TRC plates for direct tensile tests manufacturing process.

Table 3.9 - Average gauge length thickness of the TRC plates.

Composite	Gauge length thickness (mm)
CONV-UNCO	10.6 ± 0.50
CONV-WBEP-04h	9.87 ± 1.24
CONV-WBEP-24h	9.45 ± 1.00
CONV-WBEP-07d	9.46 ± 0.38
CONV-THRM	9.29 ± 0.81
CONV-EPXY	11.2 ± 2.85
UHPC-EPXY	13.7 ± 1.70

The TRC plates were demolded approximately 24 hours after casting and then stored in a curing room with controlled temperature (20 ºC) and humidity (55%). One day before the test, the specimens were taken out of the curing room and left

to dry in the air. All composites were tested at 28 days. Figure 3.8 shows the TRC composite for direct tensile testing and the reduced gauge length thickness.

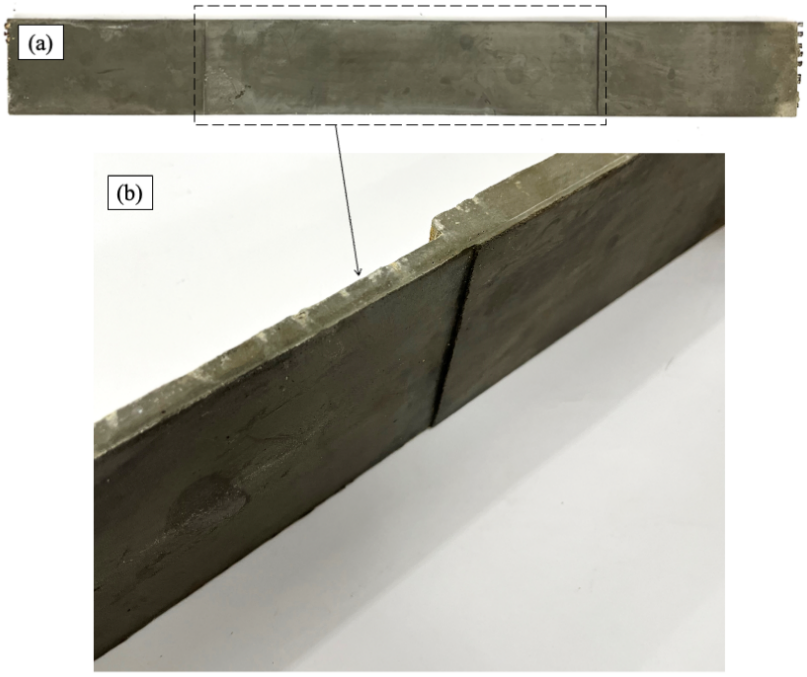


Figure 3.8 - (a) Carbon TRC composite for direct tensile test and (b) detail of reduced gauge length area.

As described in Section 3.2.2, two different fabrics were used. Therefore, the reinforcement area of the composites varied. Table 3.10 lists the number of warp yarns used, the cross-sectional area of the warp yarns, and the total cross-sectional area of the reinforcement used in each type of composite. It is worth noting that the commercial fabric GRID Q 140/110–CEP–13/17 used in this study is no longer fabricated by Solidian, and in the technical datasheet available, there is no information regarding the cross-section of the yarns without coating. Thus, for the epoxy-coated carbon fabric, the area of the GRID Q85-CCE-21 fabric from Solidian was considered because its nominal area was close to the nominal area of the EPXY carbon fabric obtained by Silva [15].

Table 3.10 - Reinforcement area of the composites for the tensile tests.

Specimen	# warp yarns	Cross-section area of the warp yarns (mm^2)	Total cross-section area of the reinforcement (mm^2)
CONV-UNCO	9	1.78	16.02
CONV-WBEP-04h	9	1.78	16.02
CONV-WBEP-24h	9	1.78	16.02
CONV-WBEP-07d	9	1.78	16.02
CONV-THRM	9	1.78	16.02
CONV-EPXY	7	1.81*	12.67
UHPC-EPXY	7	1.81*	12.67

*According to technical datasheet of the GRID Q85-CCE-21fabric.

3.3.2. Structural elements manufacturing

I-section beams were produced to study the structural behavior of carbon TRC with different coatings (water-based epoxy, thermoplastic resin, and solvent-based epoxy) and matrices (fine-grained concrete and UHPC). Furthermore, the influence of the I-section height (240 or 300 mm) on the structural performance was investigated for beams with epoxy-coated textiles. It is important to mention that the effect of the curing time was not addressed in the structural scale as the goal here was to use the fabrics under “commercial conditions”, that is, with the coating fully cured, and with its full resistance. Thus, this fabric was coated at the laboratory and the process occurred 20 days before the casting of the respective beam, taking into consideration the properties of the resin, which takes 7 days to achieve its full resistance, besides the time to prepare, assemble, and instrument the reinforcement with strain gauges.

The identification of the specimen indicates the type of matrix, the coating of the carbon fabrics, and the total I-section height for the structural elements. In this way, a beam identified as CONV-EPXY-240 refers to the beam cast with the conventional matrix using the epoxy-coated fabric with a total section height of 240 mm. Figure 3.9 illustrates the adopted nomenclature and Table 3.11 lists all the testing variables and the respective beam identification.

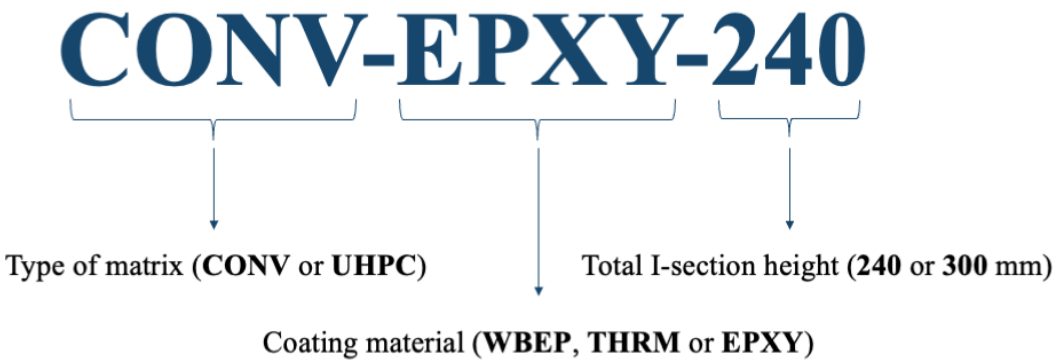


Figure 3.9 - Beam identification structure.

Table 3.11 - Test variables and beam identification.

Matrix	Carbon textile coating	I-section height (mm)	Identification
Fine-grained concrete	Water-based epoxy	240	CONV-WBEP-240
	Thermoplastic resin	240	CONV-THRM-240
	Solvent-based epoxy	240	CONV-EPXY-240
Ultra-high performance concrete	Solvent-based epoxy	240	UHPC-EPXY-240
Fine-grained concrete	Solvent-based epoxy	300	CONV-EPXY-300
Ultra-high performance concrete	Solvent-based epoxy	300	UHPC-EPXY-300

Rectangular wooden formworks measuring 150 mm × 2000 mm × 240 mm (width × length × height) were used to cast the CONV-WBEP-240, CONV-THRM-240, CONV-EPXY-240, and UHPC-EPXY-240 beams. The other beams were cast using wooden formworks with the same width and length (150 mm × 2000 mm, respectively) but with a height of 300 mm. Since the goal was to cast I-section beams with 25 mm of thickness for both the web and flange, the formworks were adapted. Polystyrene foam sheets with 62.5 mm in thickness were glued to the inside of both large sides of the formwork to obtain the desired web and flange measurements. In order to facilitate the demolding process, the polystyrene foams were wrapped in a thick plastic sheet before being glued to the formwork. Figure 3.10 shows the cross-section dimensions of the I-section beams cross-section view from the formwork already adapted with the polystyrene foam sheets and with the assembled I-section textile reinforcement. The assembly process of the carbon fabric reinforcements in the “I” shape is explained below.

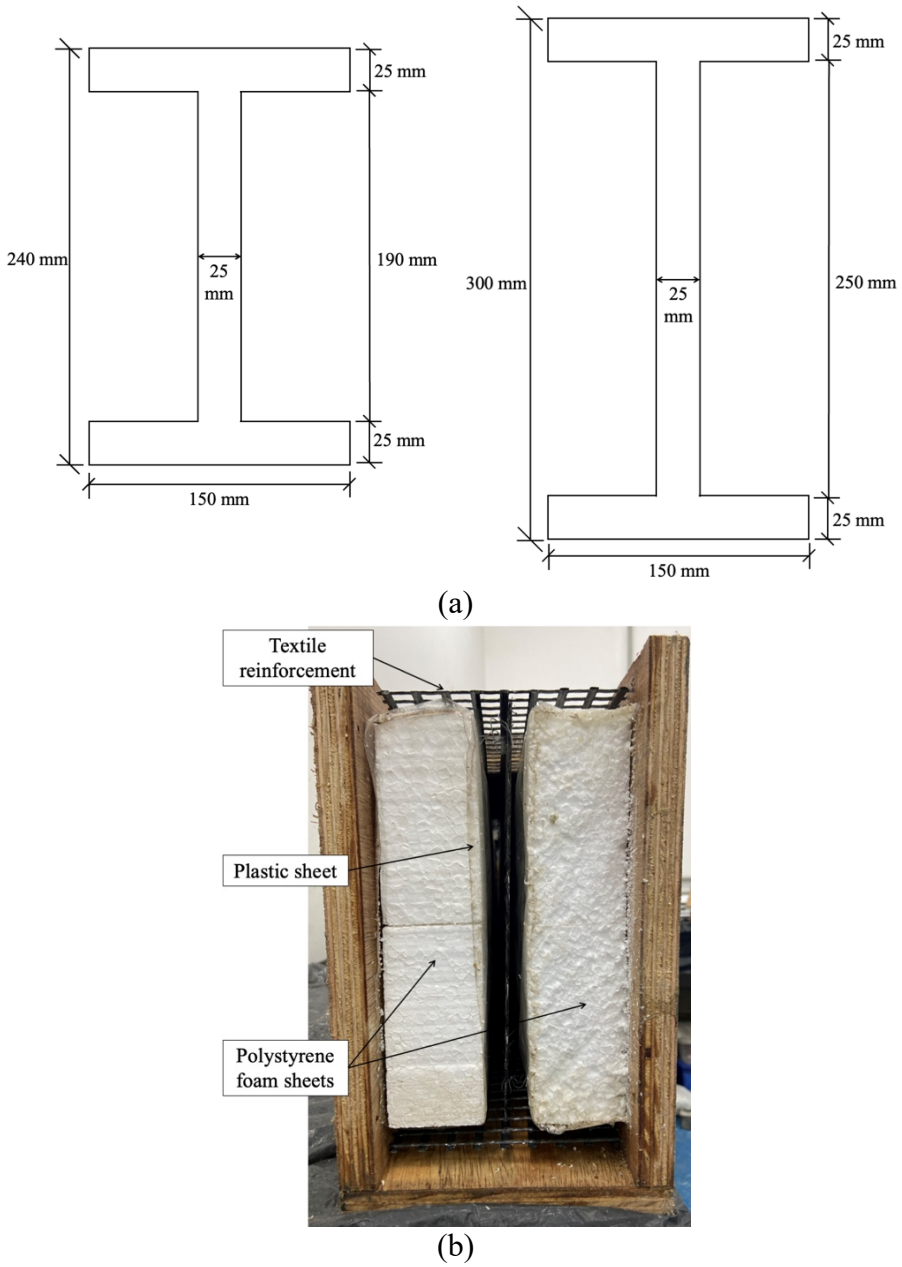


Figure 3.10 - (a) Cross-section dimensions of the I-section beams and (b) cross-section view of the adapted wooden rectangular formwork.

The textile reinforcements for the beams were assembled in an I-section geometry using wires to form the web-flange connections (see Figure 3.11). The initial idea for the fabric with the thermoplastic coating was to only use the properties of the resin to form the web-flange connections. This resin can be heated, melted, and then return to its original state after cooling, allowing it to act as a "glue" for the connection. However, it was found that the connection was fragile on its own and would not make it possible to cast the structural element without losing

the connection. Thus, wires were added at certain points to improve the web-flange junction.

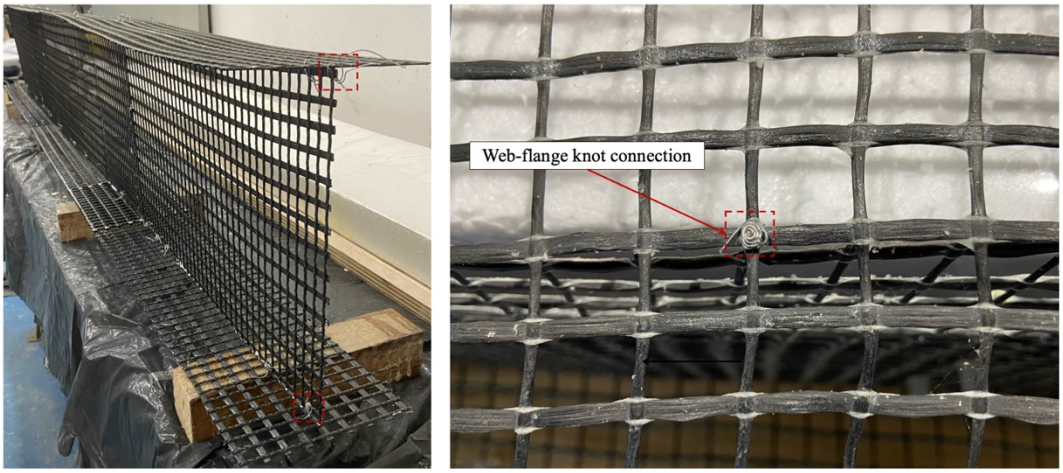


Figure 3.11 - (a) I-section carbon textile reinforcement assembled and (b) detail of web-flange connection.

As the carbon fabric coated with the solvent-based epoxy (EPXY) was available with a limited size in the warp direction, overlaps of 200 mm were made to achieve the desired reinforcement length of 2000 mm, as Figure 3.12 illustrates.

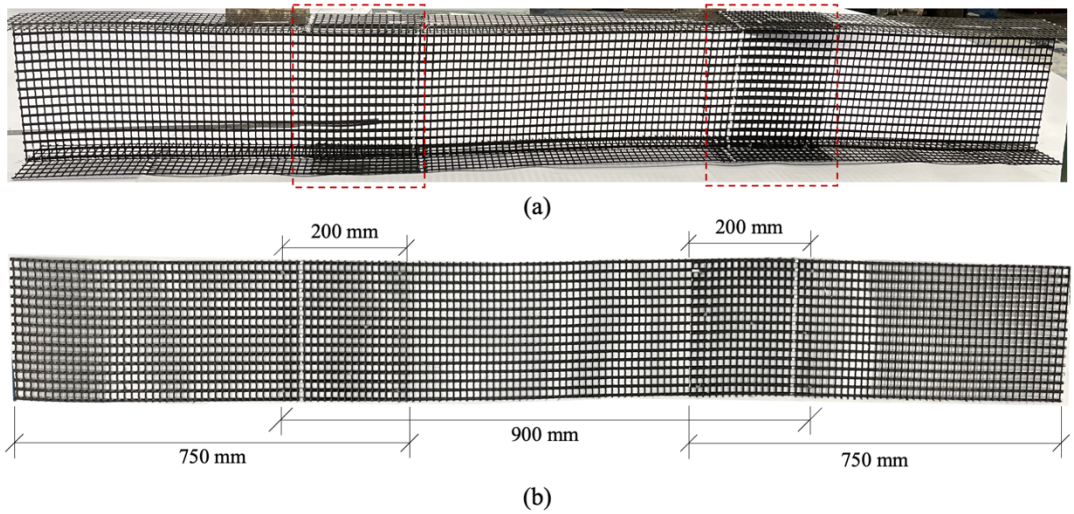


Figure 3.12 - Epoxy-coated carbon fabric: (a) overlap region and (b) overlap dimensions.

Hot glue sticks were used as spacers to ensure that the reinforcement was positioned at the midpoint of the specimen's thickness. Figure 3.13 shows the hot glue stick spacers used to achieve the 12.5 mm cover.

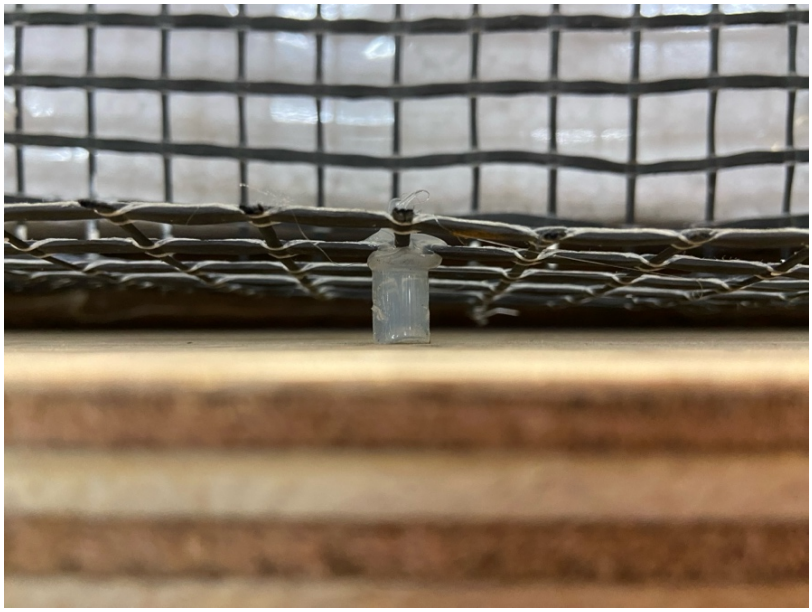


Figure 3.13 - Hot glue stick spacer.

A release agent was applied to the bottom and sides of the formworks to facilitate the subsequent demolding process. The reinforcement was placed in the formwork with one of the larger sides still open. After that, the formwork was fully assembled and positioned to cast the beams. The matrices were mixed as previously described in Sections 3.2.1.1 and 3.2.1.2, and the manufacturing procedures of the beams are detailed below.

- **Casting process of the beams with the conventional matrix**

The casting process of the beams with the conventional matrix was similar to that of a steel-reinforced concrete beam. The formwork was positioned on a leveled base and the concrete was poured directly into it. A rubber hammer was used to help the compaction of the cementitious matrix into the formwork. At the end of the casting process, steel rebar clamps were placed near the top of the formwork to prevent the sides from opening due to the internal pressure exerted by the concrete. Figure 3.14 illustrates the casting process previously described.

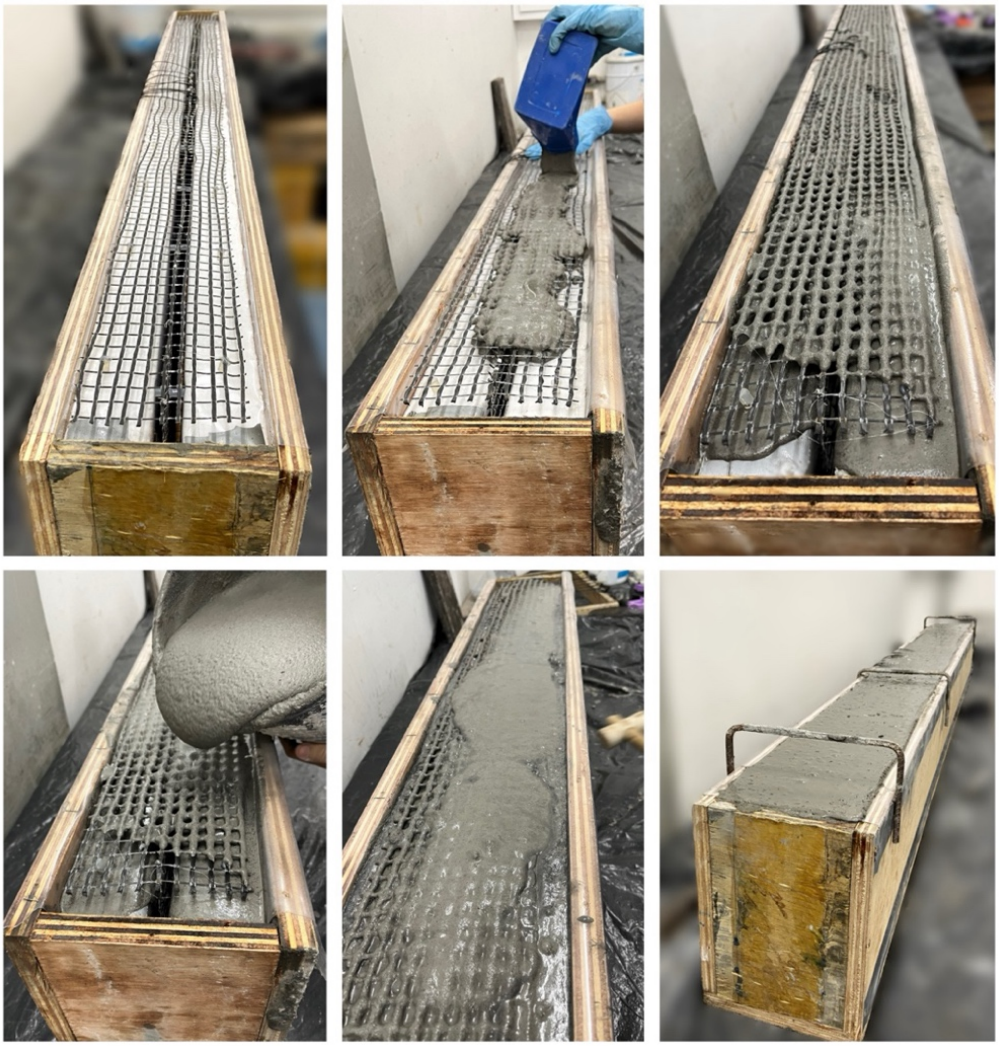


Figure 3.14 - Casting process of the beams with the conventional matrix.

- **Casting process of the beams with the UHPC matrix**

Initially, the casting process of the first beam with the UHPC matrix was the same as that previously described. However, early in the process, it was observed that the steel fibers were accumulating in the mesh openings of the textile reinforcement on the top flange, blocking the flow of concrete to the lower part of the formwork, as shown in Figure 3.15a. Therefore, the manufacturing procedure was modified to address this issue.

To cast both the UHPC-EPXY-240 and UHPC-EPXY-300 beams, one end side of the formwork was opened and adapted (see Figure 3.15b) so that the concrete could be poured through that side (Figure 3.16a), and the formwork was tilted to facilitate the flow of concrete inside (Figure 3.16b and c). In addition, part of the mold was placed on a vibrating table, which remained on throughout the

casting process. Once it was observed that the poured concrete had filled the area corresponding to the web, the end side was closed, and the formwork was repositioned horizontally (Figure 3.16d). The top flange reinforcement was manually lifted to pour the concrete underneath it until half of the top flange was filled (Figure 3.16e). After that, the concrete was poured normally to complete the other half of the top flange. At the end of the casting process, steel rebar clamps were placed near the top of the formwork to prevent the sides from opening due to the internal pressure exerted by the concrete (Figure 3.16f).

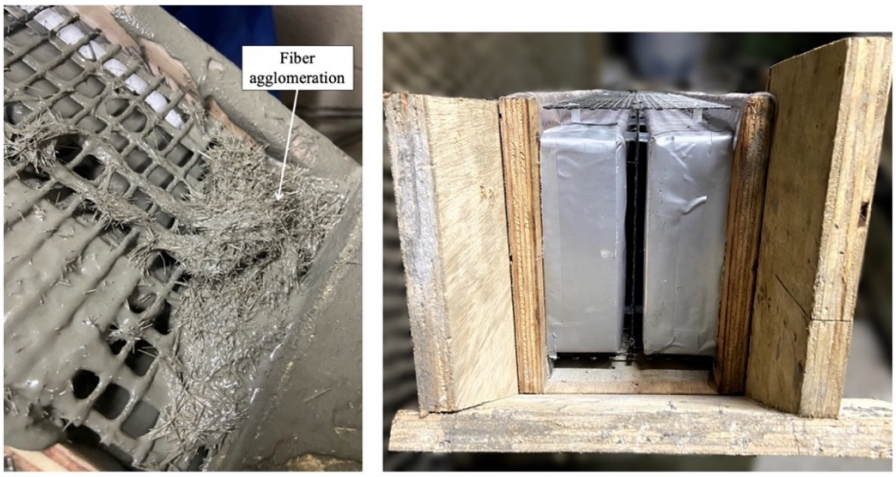


Figure 3.15 - (a) Fiber agglomeration on the mesh opening of the textile reinforcement and (b) adapted end side of the formwork to cast the beams with the UHPC matrix.

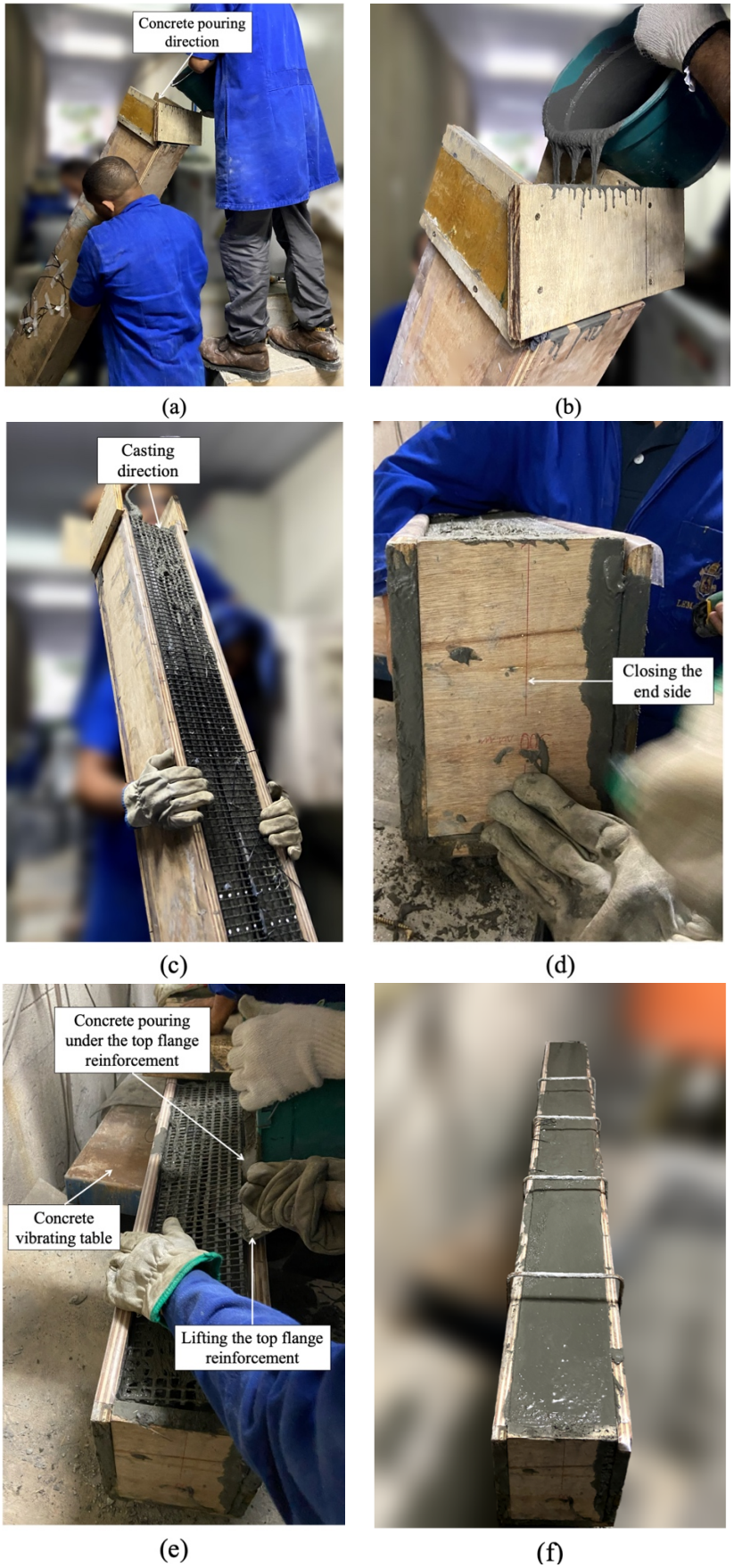


Figure 3.16 - Casting process of the carbon TRC I-section beams with the UHPC matrix.

All beams were demolded approximately 48 hours after casting and the curing process was performed in air for 27 days. The cross-section of one of the I-section beams after demolding can be seen in Figure 3.17.



Figure 3.17 - Carbon TRC I-section beam.

3.4. Testing procedures

3.4.1. Scanning Electron Microscopy (SEM)

The level and quality of impregnation of the carbon fabrics were evaluated using scanning electron microscopy. An ultra-high resolution scanning electron microscope, model TESCAN Clara, was used to obtain the images of the warp yarns and their cross-sections. It was operated at 10 kV, a high vacuum mode. The samples were sputter coated with gold to ensure conductivity.

3.4.2. Contact angle tests

The effect of the coating material on the wettability of carbon fibers was evaluated through water contact angle tests. The samples consisted of a carbon yarn of approximately 60 mm collected from the warp direction. The impregnation materials evaluated were the solvent-based epoxy (EPXY), water-based epoxy

(WBEP), and thermoplastic resin (THRM). The influence of the curing time of the WBEP resin (1 hour, 4 hours, 24 hours, and 7 days) on the wettability of the carbon yarns was also assessed.

An automatic drop tensiometer and dilatational interfacial rheometer from Teclis Scientific (model TRACKER^{TM}) were used to conduct the contact angle tests. The test consisted of placing a 1 μL drop of ultrapure water (18.2 MΩ.cm) on the surface of the carbon yarn using an aluminum needle with a diameter of 0.91 mm. The water contact angle was determined from images captured by the tensiometer and analyzed using the Wdrop software from Teclis. The value obtained after 60 seconds, when the shape of the drop had already stabilized, was considered as the final contact angle. The uncertainty associated with the contact angle measurements was estimated at ± 2°. The tests were performed at a controlled room temperature (20.3 °C) and relative humidity of 56%. Three independent measurements were performed at different points of each sample. The test setup can be seen in Figure 3.18. Figure 3.19 shows the detail of the water droplet.

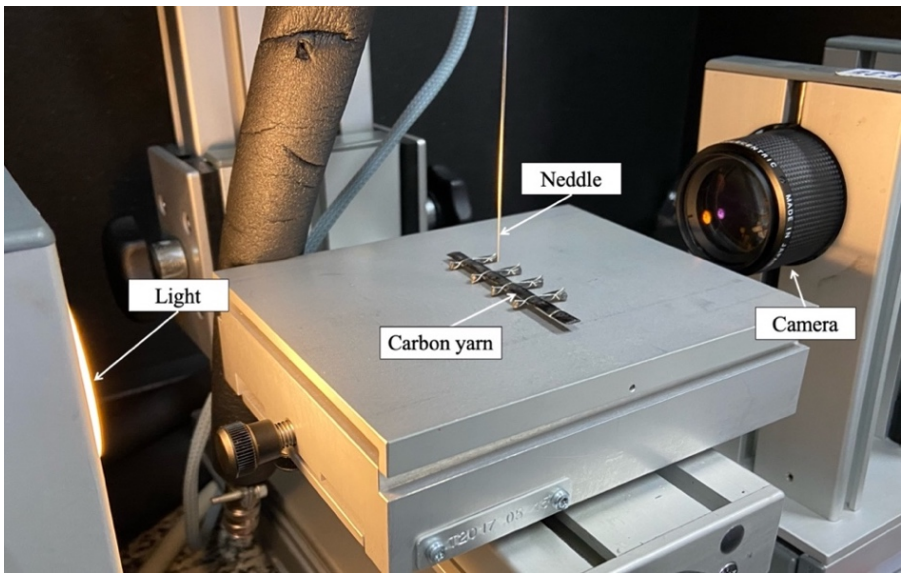


Figure 3.18 - Water contact angle test setup.

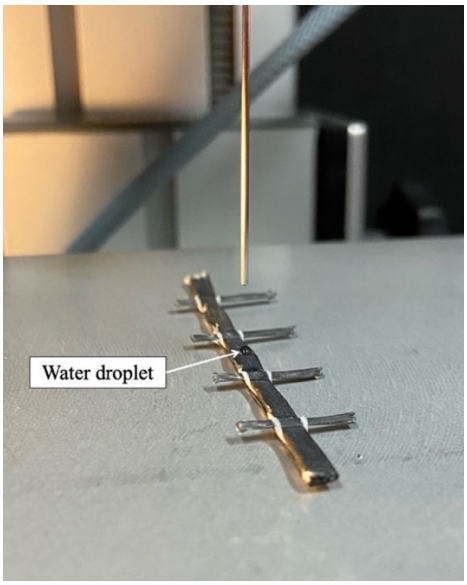


Figure 3.19 - Detail of the water droplet.

3.4.3. Three-point bending tests

Three-point bending tests were conducted to evaluate the effect of different coating materials on the stiffness of the carbon fabrics. The specimens consisted of textiles with dimensions of 100 mm × 1100 mm (width × length). In addition to the fabrics presented in Section 3.2.2 (coated with the solvent-based epoxy, fully cured water-based epoxy (WBEP), and thermoplastic resin (THRM)), carbon textiles with SBR coating were tested, as shown in Figure 3.20. The carbon fabrics coated with SBR were produced by V. Fraas. According to the manufacturer, the tensile strength and modulus of elasticity of this textile (model SITgrid017KB) are 4000 MPa and 250 GPa, respectively. The nominal cross-sectional areas of the warp and weft yarns are 3.34 and 3.30 mm^2, respectively, according to Silva [15].

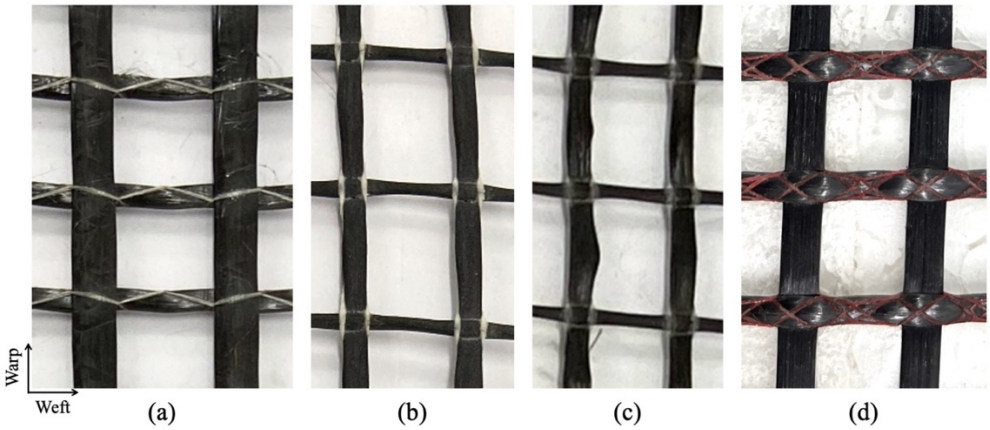


Figure 3.20 - Textiles subjected to the three-point bending tests: (a) solvent-based epoxy (EPXY), (b) water-based epoxy (WBEP), (c) thermoplastic resin (THRM), and (d) SBR.

The tests were performed in an MTS servo-hydraulic system with 100 kN loading capacity and were controlled by displacement at a rate of 6.5 mm/min. A displacement transducer with a 100 mm reading capacity was utilized to measure the mid-span deflection of the specimen during the test. A 100 N load cell was used to measure the load applied to the textile and the total span length was 600 mm. Figure 3.21 presents the test setup.

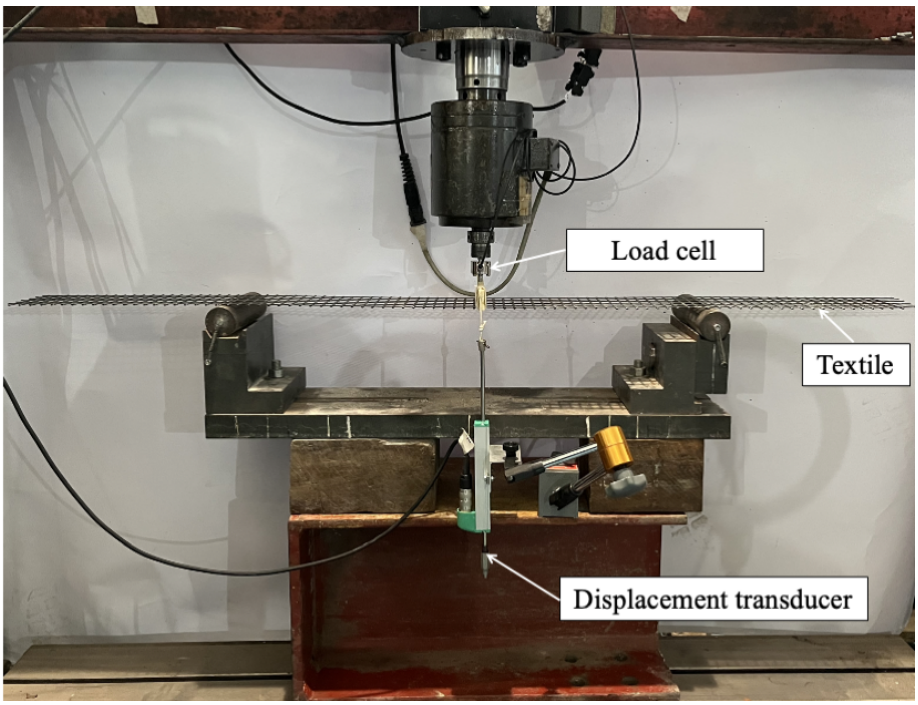


Figure 3.21 - Textile bending test setup.

3.4.4. Direct tensile tests

The mechanical behavior of the carbon TRC composites was evaluated using direct tensile tests. The tests were conducted using a universal testing machine (MTS 311) with a maximum load capacity of 1000 kN at a displacement rate of 0.5 mm/min.

Figure 3.22 presents the direct tensile test setup. Two Linear Variable Displacement Transducers (LDVTs) with a reading capacity of 250 mm were used to measure the displacement of the specimens. Aluminum extensors with a length of 250 mm were attached to the end of each LVDT to meet the required gauge length (500 mm). The LVDTs were fixed to the lateral ends of the specimens using an aluminum frame. To connect the specimen to the testing machine, both ends of the TRC composites were clamped onto steel plates with screws. A click-type torque wrench was used to bolt the screws with the same desired torque. The boundary conditions adopted in this study were the clamping area, number of screws, and torque on the screws. These boundary conditions were determined based on the study conducted by Silva [15].

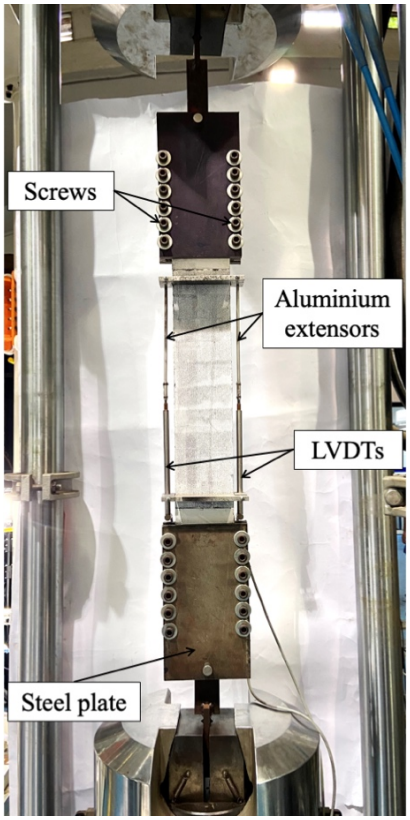


Figure 3.22 - Direct tensile test setup.

For direct tensile tests on carbon TRCs with epoxy-coated textiles, Silva [15] defined 26,400 mm^2 for the contact surface, 12 screws, and 29 Nm of torque as values for the boundary conditions. These values were initially as the boundary conditions for all composites in this study. However, these conditions proved to be inadequate for specimens with the UHPC matrix and carbon textile with the solvent-based epoxy coating. It was observed during the testing of the first composite of the UHPC-EPXY series that the specimen began to slip within the steel plates. A clear indication of the slippage of the specimen was the slow and gradual drop in the load applied by the machine from a certain point, even though the specimen had not failed yet. Therefore, it was necessary to modify one of the boundary conditions to test the UHPC-EPXY composites. It was decided to maintain the contact area between the steel plates and the composite and the number of screws, and only to increase the torque applied to the screws from 29 to 40 Nm. Table 3.12 summarizes the boundary conditions for each composite type.

Table 3.12 - Direct tensile tests boundary conditions.

Specimen	Contact surface (mm^2)	Number of screws	Torque (Nm)
CONV-UNCO	26,400	12	29
CONV-WBEP-04h	26,400	12	29
CONV-WBEP-24h	26,400	12	29
CONV-WBEP-07d	26,400	12	29
CONV-THRM	26,400	12	29
CONV-EPXY	26,400	12	29
UHPC-EPXY	26,400	12	40

Digital Image Correlation (DIC) technique was used to evaluate the deformation and cracking patterns of the carbon TRC composites. For this purpose, a black and white speckle pattern was painted on one side of the specimens in the gauge length area. The DIC setup consisted of a high-resolution camera (5 MP) to capture images at a rate of 10 images every 3 seconds and two lights for uniform illumination of the specimen, as presented in Figure 3.23. The images obtained from each test were analyzed using the VIC-2D software [132] from Correlated Solutions.

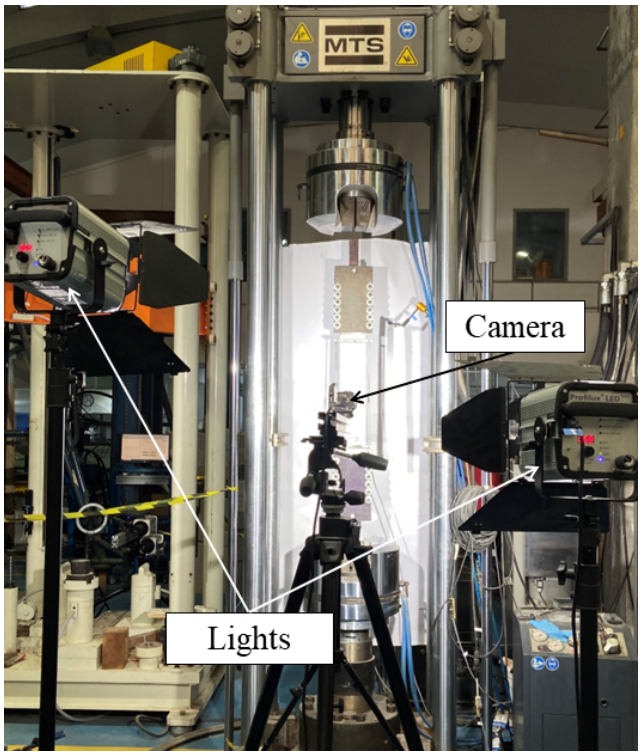


Figure 3.23 - DIC setup for direct tensile test.

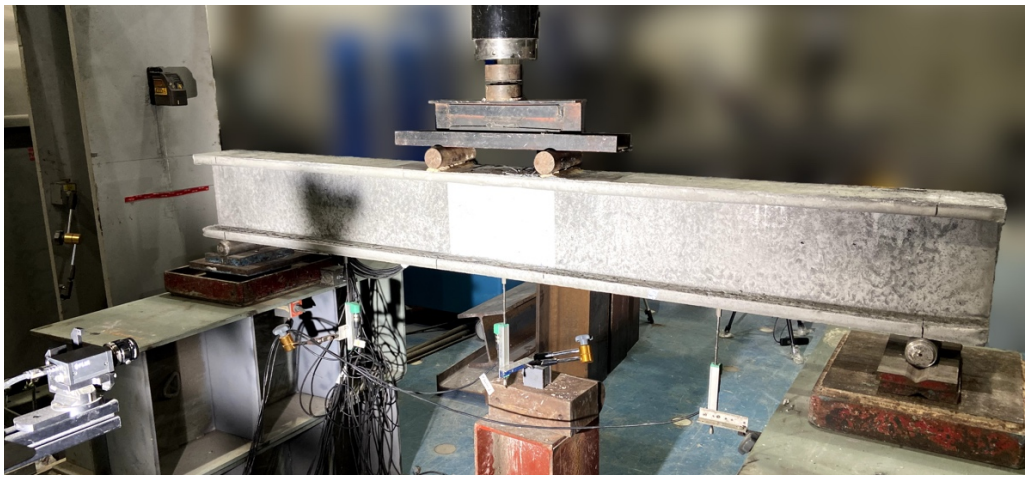
3.4.5. Four-point bending tests

Four-point bending tests were conducted to analyze the flexural behavior of the carbon textile reinforced concrete I-section beams. An MTS servo-hydraulic system with 500 kN capacity was used to perform the tests, and the tests were controlled by displacement at a 1 mm/min rate. All beams were tested at 28 days.

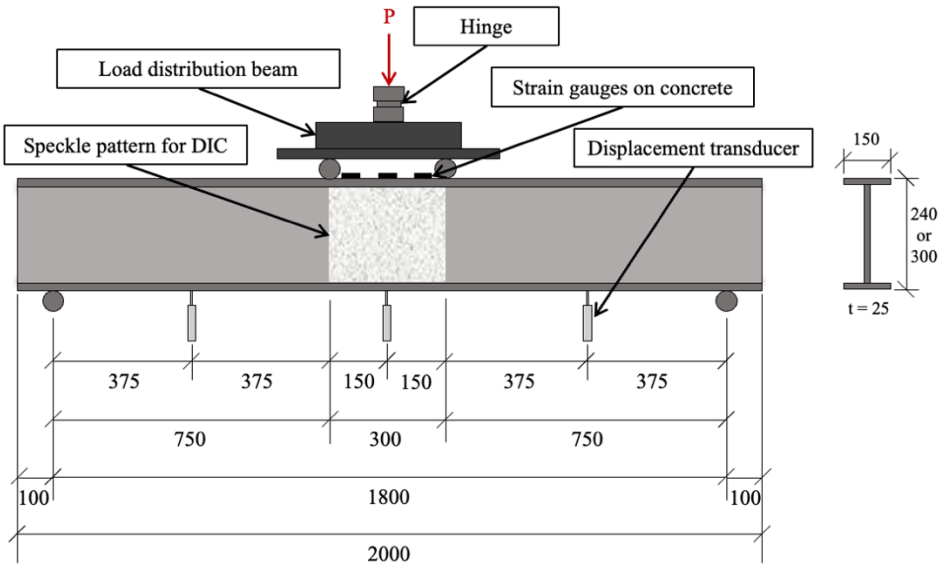
The beams were tested under isostatic conditions using a pinned support and a roller support to allow horizontal displacement during the test. An 1800 mm span was considered. The load was applied by the actuator on a hinge placed over a load distribution beam. The deflection at three different points was measured using three displacement transducers, one positioned at the mid-span and the other two positioned 375 mm from each support (see Figure 3.24). Strain gauges were used to measure the strain values. The number of strain gauges and their placements varied as follows: for the CONV-EPXY-300 and UHPC-EPXY-300 beams, nine strain gauges were placed on the concrete (three on the top flange, three on the web, and three on the bottom flange). For the other beams, 12 strain gauges were used in total: nine on the textile reinforcement (three on the top reinforcement flange, three on the reinforcement web, and three on the bottom reinforcement flange) and three

on the concrete (on the top flange of the beam). The strain gauges distanced 5 cm from each other. Figure 3.25 shows the detail of the strain gauges placed on the top flange (Figure 3.25a) and web (Figure 3.25b) textile reinforcement, both in the warp direction. It is worth noting that the strain gauges placed on the reinforcement were covered with a thin layer of hot glue to avoid being damaged by the water in the concrete mixture during the casting process of the beams.

Digital Image Correlation (DIC) technique was used to evaluate the cracking pattern of the carbon TRC I-section beams on the web in the constant moment region during the test, as illustrated in Figure 3.24. The setup consisted of a high-resolution camera (5 MP) to capture images at a rate of 1 image every 3 seconds and lights to guarantee proper illumination of the specimen. The images obtained from each test were analyzed using the VIC-2D software [132] from Correlated Solutions.

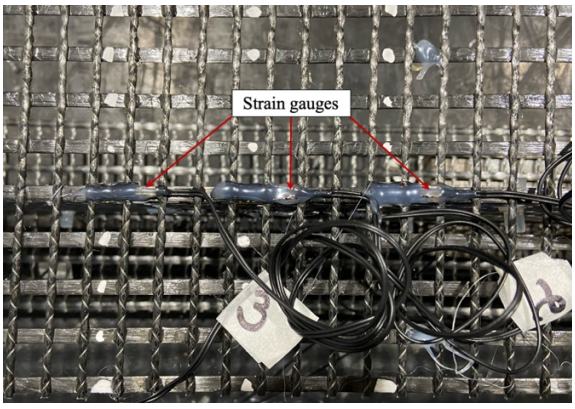


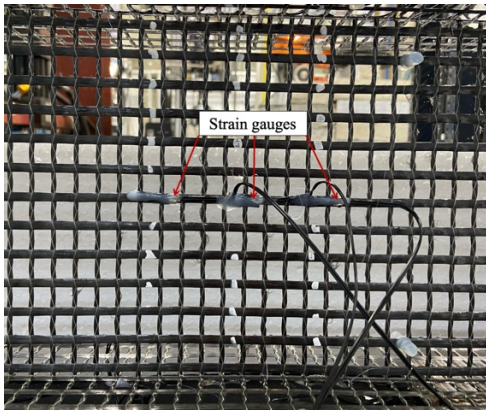
(a)



(b)

Figure 3.24 - Four-point bending test setup: (a) overview and (b) schematic representation (dimensions in mm).





(a) (b)

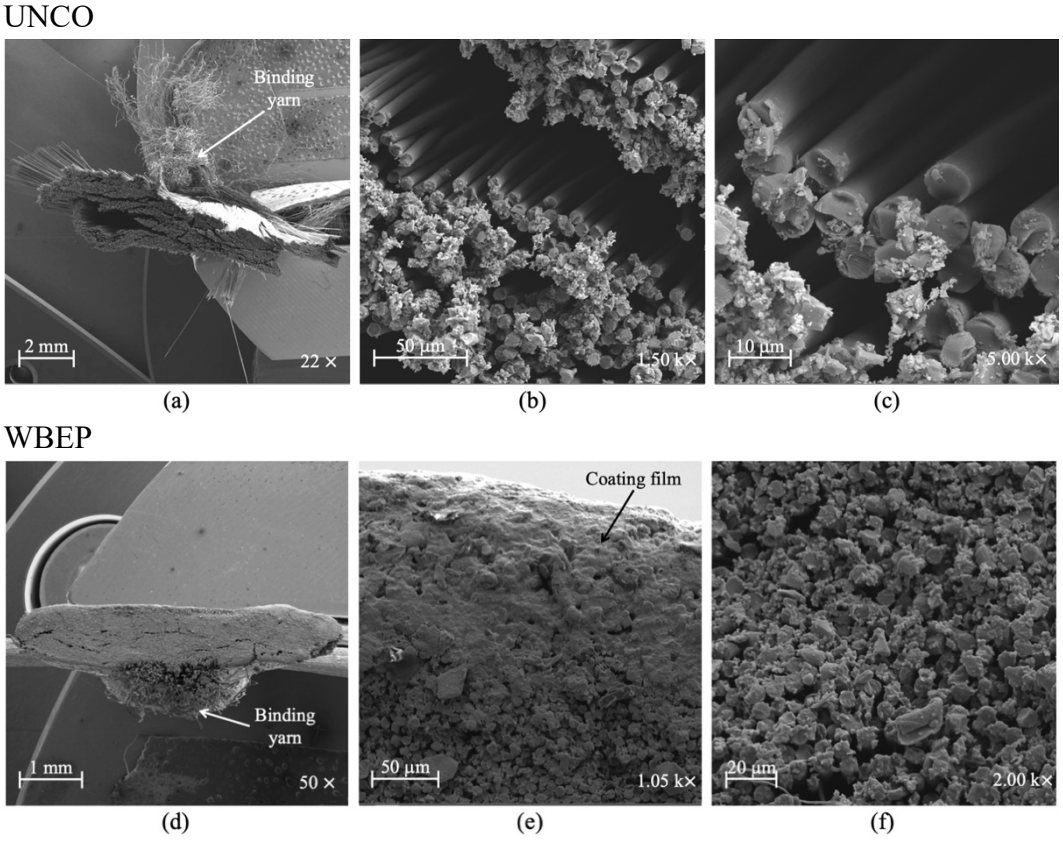
Figure 3.25 - Strain gauges placed on the (a) top flange textile reinforcement and (b) on the web textile reinforcement.

4
Results and Discussion

4.1.
Effect of surface coating on the physical and mechanical properties of carbon textiles

4.1.1.
Morphological characterization

The morphological characteristics of the coated and uncoated carbon textiles were analyzed using a Scanning Electron Microscope (SEM). The cross-sectional structure and the level of impregnation were observed. Figure 4.1 presents the cross-section micrographs at different magnitudes of the carbon textiles without coating (UNCO) and with coating (WBEP, THRM, and EPXY). It is important to mention that magnitudes varied according to the sample, since the objective was to visualize the key characteristics of each yarn type.



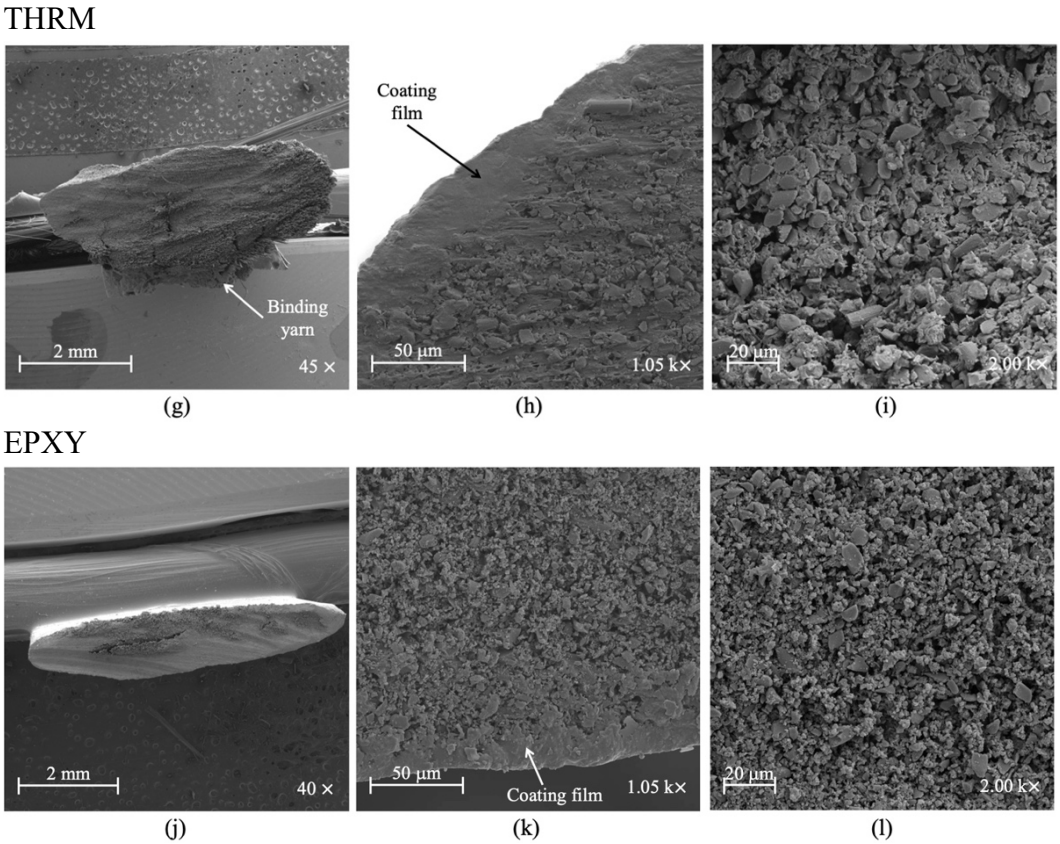


Figure 4.1 - SEM images of the cross-sections of the (a, b, c) uncoated, (d, e, f) water-based epoxy-coated, (g, h, i) thermoplastic resin-coated, and (j, k, l) epoxy-coated carbon textiles warp yarns.

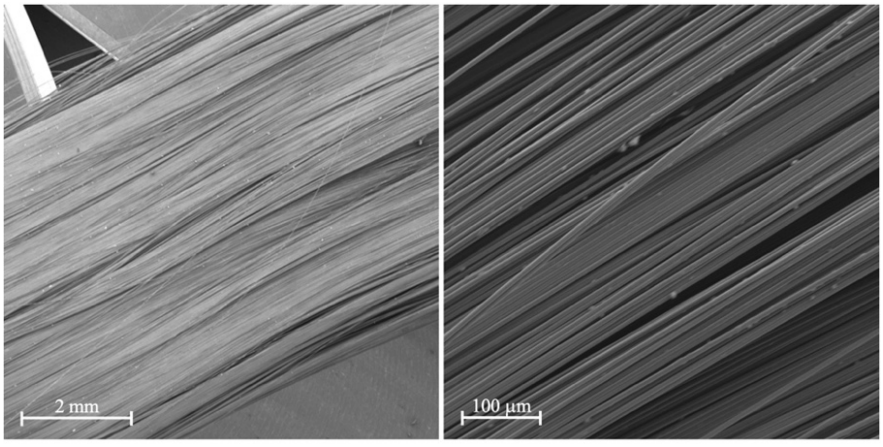
In Figure 4.1a, b, and c, it is possible to note the multiple filaments and voids that compose the uncoated carbon textiles. Uncoated carbon textiles present poor dimensional stability, and the filaments are able to move freely. Thus, the cross-section of this yarn varied considerably in relation to the other samples analyzed, presenting a more open geometry.

Figure 4.1d, e, and f show the fabric coated with the water-based epoxy resin. It can be seen that the WBEP coating provided greater dimensional stability to the carbon fabric, displaying a relatively well-defined elliptical shape. The outermost region of the sample is displayed in Figure 4.1e. It is possible to observe that the WBEP resin formed a “film” around the fabric, resulting in the union of the filaments and forming a cohesive structure. Nevertheless, it can also be noted in the same figure that the more uniform coating is limited to the outermost filaments and the inner filaments can be seen on the lower part of the image. Figure 4.1f shows a more central region of the yarn, revealing some voids between the filaments and a lower degree of impregnation in this area.

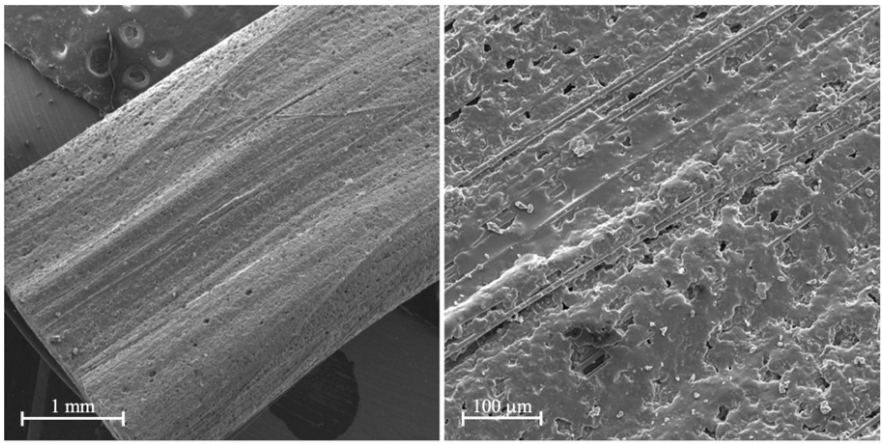
The cross-section of the fabric with the thermoplastic resin coating is shown in Figure 4.1h, j, and i. It is interesting to observe that although the WBEP and THRM samples utilized the same type of carbon textile, their cross-sections differed in shape, possibly due to the different impregnation methods used. The THRM yarn exhibits a narrower elliptical form than the WBEP specimen. Furthermore, it is observed that the THRM sample has fewer voids compared to the WBEP, indicating a better level of impregnation, with the resin penetrating deeper into the yarn, as can be seen in Figure 4.1i.

Figure 4.1j, k, and l display the cross-section of the commercially available carbon fabric impregnated with a solvent-based epoxy resin. This fabric presents a well-defined elliptical shape. Figure 4.1j shows a much more uniform cross-section compared to the WBEP textile. There are no significant voids within the yarn, and the resin appears to have fully impregnated the yarn, even in its central region (see Figure 4.1l). It is important to note that the EPXY fabrics underwent an industrial coating process; therefore, a higher level of impregnation was expected compared to the other samples.

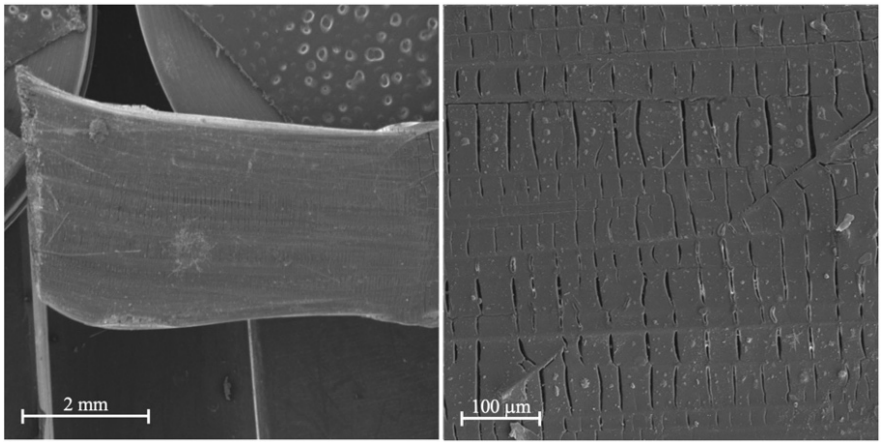
The longitudinal view of the warp yarns of the carbon fabrics obtained with SEM can be observed in Figure 4.2. The images reveal the varying surface roughness induced by different coating materials.



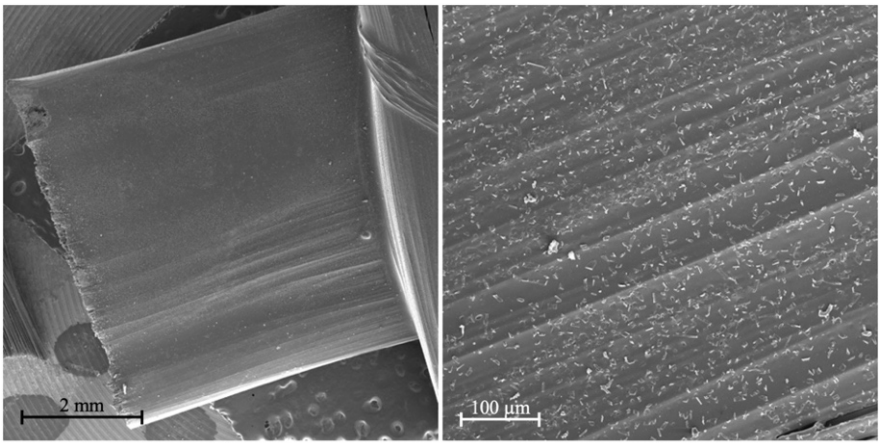
(a) UNCO



(b) WBEP



(c) THRM



(d) EPXY

Figure 4.2 - SEM images of the warp yarns of the (a) uncoated, (b) water-based epoxy-coated, (c) thermoplastic resin-coated, and (d) solvent-based epoxy-coated carbon textiles.

The uncoated fabrics present a smooth surface, and the empty spaces between filaments can clearly be seen (Figure 4.2a). The carbon textile coated with the water-based epoxy, on the other hand, exhibits a slightly uneven and rough surface (Figure 4.2b), which could be linked to the manual coating process employed to

apply the resin on the fabric. No significant empty spaces can be observed among the filaments due to the film formed by the coating around the perimeter of the yarn.

The fabric with thermoplastic resin presented a smoother surface than the WBEP fabric. In Figure 4.2c, some carbon filaments and some small cracks on the surface of the yarn can be seen. These cracks on the resin might have been caused by the process of preparation of the samples for the SEM analysis. The fabrics needed to be cut, and this might have generated these cracks on the resin since thermoplastic materials present lower resistance than thermoset resins [19]. The sample with solvent-based epoxy impregnation also had a smooth surface (Figure 4.2d), mostly likely as a result of the coating process performed on an industrial level.

4.1.2. Analysis of the hydrophobicity of carbon textiles

The chemical composition of the coating materials plays a significant role on the bond with the cementitious matrix. Hydrophobic materials tend to lead to a weaker textile-matrix interface due to the repelling nature of these materials towards the hydrophilic concrete. In this way, assessing the wettability of carbon yarns coated with different materials is essential to evaluate their influence on the mechanical performance of the TRC composites. Table 4.1 presents the results of the measured water contact angles at 10 and 60 s after placing the water droplet on the surface of the yarn, which was considered the final contact angle.

Table 4.1 - Average measured contact angles of the carbon yarns.

	Contact angle at 10 s (°)	Contact angle at 60 s (°)
WBEP-01h	41.8 (0.51)	21.5 (1.87)
WBEP-04h	73.6 (0.424)	60.8 (2.55)
WBEP-24h	71.3 (0.363)	69.2 (0.296)
WBEP-07d	71.3 (0.794)	67.9 (1.07)
THRM	39.6 (2.51)	34.9 (2.78)
EPXY	50.3 (4.98)	47.3 (4.67)

The difference in the shape of the water droplet on the carbon yarns are illustrated in Figure 4.3. The variation in the contact angle measured after 60 s and 10 s on the WBEP-01h series was approximately 48.5%. For the WBEP coating

cured for 4 hours, the variation in contact angle was about 17.4% between the angles measured at 60 s and 10 s. The subsequent increase in the curing time for 24 hours and 7 days significantly decreased this difference at about 3.03% and 5%, respectively. In the case of the THRM, the contact angle was approximately 11.8% lower at 60 s, and as for the EPXY, the variation was about 5.90%.

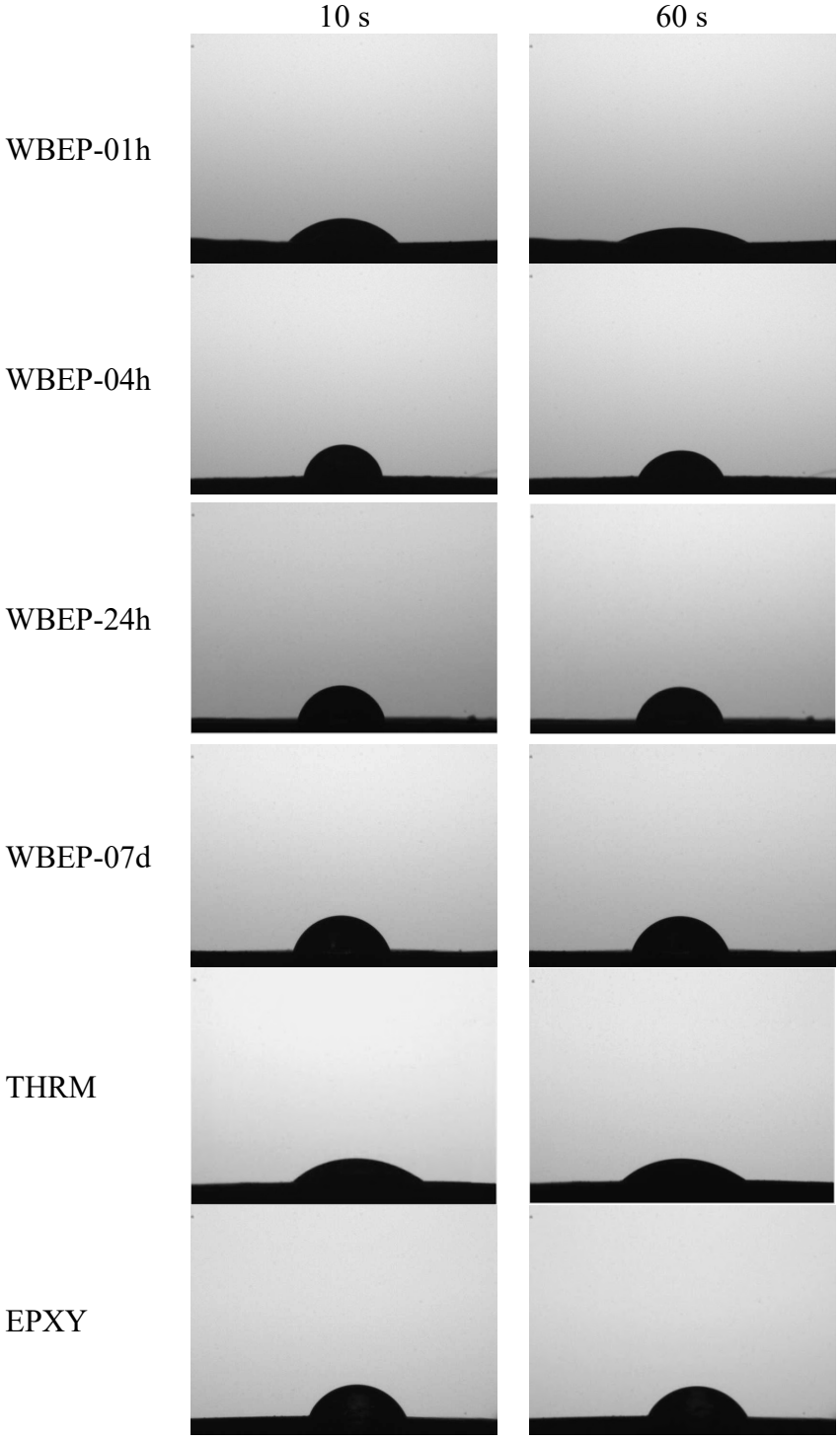


Figure 4.3 - Images from the contact angle tests images for different times (10 and 60 s) for the carbon yarns.

Lower contact angles suggest an affinity of the material with water, indicating higher wettability and a more hydrophilic nature. The carbon yarns with the water-based epoxy cured for one hour presented the lowest final contact angle (at 60 s) among the other series. This can be explained by the fact that at an early stage of curing, the water present in the hardener component has not evaporated completely yet and as a consequence, the carbon yarn absorbs or attracts the water, resulting in a lower final contact angle.

In the case of the WBEP-04h, part or most part of the water has evaporated due to the ongoing chemical reactions. In this way, the hydrophobicity of the yarn significantly increased in relation to the WBEP-01h. The contact angle at 60 s was 64.6% higher. With the advanced curing process, all of the water in the WBEP resin evaporated, and the material became increasingly more hydrophobic, presenting higher final contact angles, as can be seen in Table 4.1. Furthermore, as the curing progressed, the coating material hardened, forming a more cohesive structure and preventing the water from penetrating between these small spaces.

The results show that the water-dispersed epoxy coating with higher curing times yields carbon yarns with a more hydrophobic nature than the solvent-based epoxy, and the thermoplastic resin. The carbon yarns coated with the thermoplastic resin presented the second lowest contact angle after one minute, possibly indicating the more hydrophilic nature of this coating material (an aqueous polyacrylate dispersion). It is important to mention, however, that the contact angle depends on the surface tension, the hydrophobicity of the material and the surface roughness [133,134]. SEM analysis of the fabrics illustrates the roughness of carbon fabrics with different impregnations and helps understanding the results of the water contact angle tests. As mentioned earlier, the textiles with the WBEP coating exhibit a considerably rougher surface than those with the EPXY and THRM coatings (see Section 4.1.1). This might explain the higher contact angles observed on the WBEP specimens (with the exception of the WBEP-01h) than on the other types of coatings. The slight difference between the WBEP-07d and WBEP-24h can also be attributed to the different surface roughness, as these fabrics were coated in separate instances.

4.1.3.
Analysis of the stiffness of carbon textiles

The stiffness conferred by different coating materials directly affects the design flexibility of TRC. Thus, it is important to know this mechanical property of each coated-textile. The representative load *vs.* deflection curves for each type of carbon fabric subjected to the three-point bending tests are shown in Figure 4.4. Table 4.2 lists the average loads and flexural stiffness at a deflection of 80 mm, as well as their respective standard deviations. The flexural stiffness of the fabrics (*EI*) was determined according to Equation 4.1. Due to the testing conditions, the maximum deflection of the specimens was defined as 80 mm. Thus, the flexural stiffness was calculated at a maximum mid-span deflection of 80 mm.

$$EI = \frac{PL^3}{48\delta} \tag{4.1}$$

in which P, L, and δ are the applied load (N), span (cm), and mid-span deflection (cm), respectively.

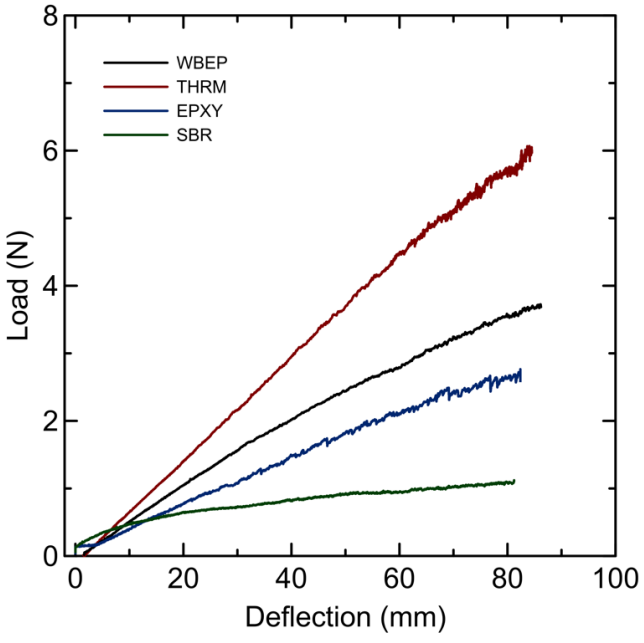


Figure 4.4 - Representative load *vs.* deflection curves for the WBEP, THRM, EPXY and SBR carbon textiles obtained from the three-point bending tests.

Table 4.2 - Average load and flexural stiffness results of three-point bending tests on the carbon fabrics at an 80 mm mid-span deflection.

Textile	P_{80} (N)	$(EI)_{80}$ (Ncm^2)
WBEP	3.39 (0.323)	1908.9 (181.1)
THRM	5.44 (0.377)	3057.3 (211.9)
EPXY	2.53 (0.100)	1425.4 (56.2)
SBR	1.13 (0.0346)	633.5 (19.4)

As can be seen in Table 4.2, the SBR fabrics required the lowest average load to achieve a mid-span deflection of 80 mm, followed by the EPXY, WBEP, and THRM series, respectively.

From Equation 4.1, the bending stiffness (EI) was calculated. The stiffness of the fabric is directly related to its flexibility: the higher the stiffness, the lower the flexibility, which may limit its use in certain situations. As expected, the SBR-coated fabrics presented the lowest bending stiffness with an average of 633.5 Ncm^2. SBR coatings are well known for resulting in flexible textiles that can be used in a variety of applications. In contrast, the solvent-based epoxy resin (EPXY) impregnations produce much more rigid textiles compared to SBR. The average bending stiffness of the EPXY series was approximately 125.01% higher than the SBR.

Despite not being fully impregnated (see Figure 4.1f), the WBEP fabric showed a stiffness approximately 201% greater than that of the SBR. In relation to the EPXY, the stiffness was approximately 34% higher. Nonetheless, these results are not in line with those reported by Scheurer *et al.* [17]. The authors performed cantilever tests on carbon rovings and observed that impregnation with WBEP resin resulted in a fabric slightly more flexible than that with SBR coating, with an average bending stiffness of approximately 414 Ncm^2.

While there is a significant discrepancy in the values of flexural stiffness of specimens coated with water-based epoxy obtained in this study, and in the one conducted by Scheurer *et al.*, the average results of the EPXY and SBR series were about the same range (1389.9 Ncm^2 and 566.6 Ncm^2, respectively). The different impregnation methods used for the WBEP specimens might be a reason for the discrepant values. Scheurer *et al.* [17] used a discontinuous impregnation method with rollers of a Labcoater, and the process was done vertically. In the present study, the carbon textiles were coated horizontally with a paint roller, which led to some

accumulation of resin in some regions of the bottom side of the textile. In the impregnation method employed in [17], the resin excess was removed by squeezing the carbon rovings between the rollers.

The fabric impregnated with the thermoplastic resin presented the highest bending stiffness among all specimens. In comparison to the solvent-based epoxy (EPXY) fabric, which is commercially known as a stiff reinforcement, THRM exhibited a stiffness approximately 114% greater. Compared to SBR, this stiffness was 382% higher. While THRM displayed the greatest rigidity and the least flexibility, the thermoplastic resin offers the advantage of being reshaped upon heating, as Figure 4.5 illustrates. Once the resin is cured, it retains high rigidity, having the potential to not influence the performance of the composite. Therefore, despite the higher flexural stiffness of the THRM fabric compared to both EPXY and SBR, this does not imply that the thermoplastic coating would limit the versatility of the TRC.



Figure 4.5 - Reshaped carbon textile with the thermoplastic resin coating.

4.2.
Mechanical behavior of carbon TRC composites

4.2.1.
Influence of surface coating

The influence of the impregnation material on the mechanical performance of the carbon TRC is discussed below. It is important to mention that, for the water-based epoxy coating, only the CONV-WBEP-07d series will be considered for comparison with the other coatings, as the objective here is to evaluate the fabrics under commercial conditions, that is, textiles that have been impregnated and have undergone the full curing process before sale. The effect of the curing time of the WBEP resin on the tensile properties of the TRC composites is examined in the following section.

The representative tensile stress *vs.* strain curves of the TRC composites with the conventional matrix and UNCO, WBEP-07d, THRM, and EPXY textiles are presented in Figure 4.6. Table 4.3 lists the average results for the first crack tensile stress (σ_{cr}), strain at the first crack stress (ε_{cr}), tensile strength (σ_{max}), strain at tensile strength (ε_{max}), and the standard deviation of the average results obtained for these composites.

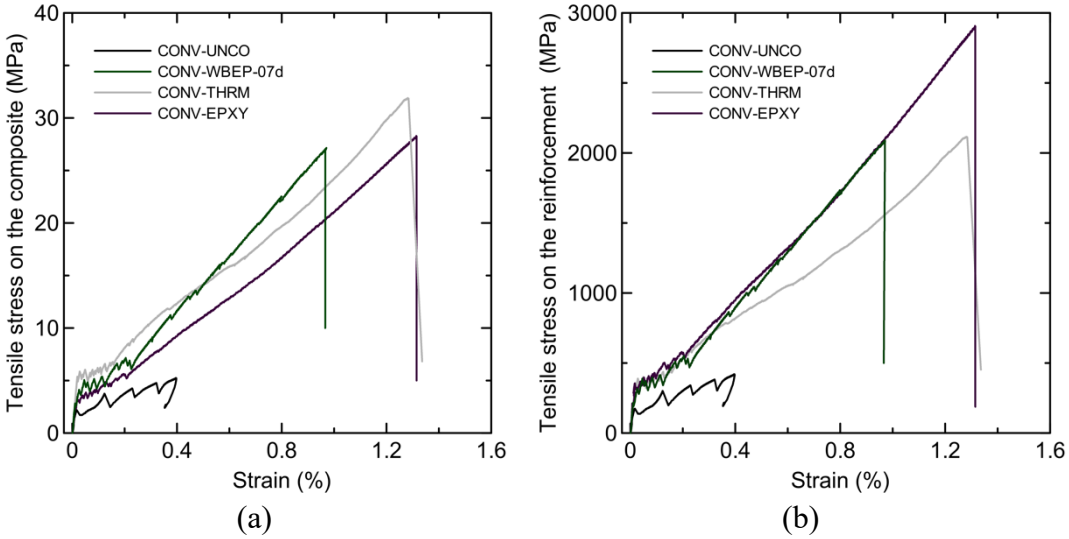


Figure 4.6 - Representative tensile stress *vs.* strain curves for the CONV-UNCO, CONV-WBEP-04h, CONV-WBEP-24h, CONV-WBEP-07d, CONV-THRM and CONV-EPXY carbon TRC composites calculating the stresses with the (a) composite area and (b) reinforcement area.

Table 4.3 - Average results of the direct tensile tests for the CONV-UNCO, CONV-WBEP-07d, CONV-THRM, and CONV-EPXY carbon TRC composites.

Composite	$\sigma_{cr,CA}$ (MPa)	ε_{cr} (%)	$\sigma_{max,CA}$ (MPa)	$\sigma_{max,RA}$ (MPa)	ε_{max} (%)
CONV-UNCO	2.00 (0.189)	0.0205 (0.00537)	4.70 (0.444)	378.6 (29.7)	0.309 (0.0863)
CONV-WBEP-07d	2.51 (0.568)	0.0128 (0.00532)	28.6 (1.10)	2060.3 (87.5)	0.966 (0.0457)
CONV-THRM	3.86 (0.933)	0.0199 (0.00747)	31.2 (2.88)	2189.9 (81.1)	1.33 (0.0743)
CONV-EPXY	2.89 (1.38)	0.0107 (0.00651)	31.4 (11.9)	3068.7 (405.2)	1.27 (0.151)

$\sigma_{cr,CA}$ – first crack stress (obtained using the cross-sectional area of the composite).
ε_{cr} – first crack strain.
$\sigma_{max,CA}$ – ultimate tensile strength (obtained using the cross-sectional area of the composite).
$\sigma_{max,RA}$ – ultimate tensile strength (calculated using the reinforcement area).
$\varepsilon_{\sigma,max}$ – ultimate strain.

All the composites with the coated textiles exhibited the characteristic strain-hardening behavior of TRC under tensile loads. The typical tensile stress *vs.* strain curves can be divided into three distinctive stages [7]. Initially, the specimens exhibited a linear response, similar to that presented by traditional steel RC. In this stage (known as linear elastic stage or Stage I), the stiffness of the composite was governed by the stiffness of the uncracked matrix, and the load increased until the matrix reached its tensile strength, forming the first crack. Once the first crack was formed, the multiple-cracking stage, also called Stage II, initiated. In this stage, several small cracks opened as the applied load increased. When the formation of new cracks ended, the post-cracking stage (Stage III) started, and an increase in tensile stress and the widening of the cracks were observed until the specimen's rupture [17], caused by the reinforcement failure or its pull-out.

It is possible to observe in Figure 4.6 that the TRC composites with the uncoated carbon textile did not exhibit the characteristic strain-hardening behavior previously described. Moreover, this series presented a significantly inferior mechanical performance compared to the other composites. However, the lack of a strain-hardening response and a lower tensile response was expected for these composites. Although the obtention of a strain-hardening response in TRC composites is relatively easy due to the high volume fraction provided by the textile reinforcements [61], this type of behavior is also highly dependent on the textile-matrix bond.

Achieving proper bond strength in carbon TRC with uncoated textiles is difficult because of the multifilament nature of the yarns composing the fabrics. As explained in Section 2.4, the incompatible dimensions of the cement grain diameters and the spaces between the filaments prevent the impregnation of the cementitious matrix within the yarn. As a consequence, only the external filaments are properly anchored to the matrix, and the main stress transfer mechanism within the roving is friction. Because this stress transfer mechanism is highly inefficient, the internal filaments do not properly contribute to the load-bearing capacity of the composite, considerably decreasing the mechanical properties of the carbon TRC.

Additionally, carbon fabrics exhibit poor bonding with cementitious matrices due to the hydrophobic nature of these fibers [11]. As concrete is a hydrophilic material, the opposing nature of these materials leads to a weaker densification of the reaction products of the cementitious matrix around the reinforcement, which compromises the textile-matrix interface, and consequently, the bond between these two phases.

Besides presenting a strain-hardening behavior, it can be noted in Figure 4.6 that the TRC composites with coated fabrics exhibited significantly superior mechanical performances than the series with the uncoated textiles. In the case of the WBEP coating, the maximum tensile stress increased by 509% in comparison to the CONV-UNCO series when the stresses were obtained using the composite area. When the tensile stresses were calculated using the reinforcement area, this improvement was 444%. Moreover, the strain capacity of the composites increased by 213%. Similarly, the thermoplastic coating positively contributed to improving the mechanical performance of the carbon TRC composites. The tensile strength and strain capacity increased by approximately 564% and 330%, respectively, in relation to those of the composites without textile coating. These results indicate that the bond strength and, consequently, the stress transfer within the multifilament yarns were successfully improved by these coatings, leading to the desired strain-hardening response, and to a better cracking behavior. Nevertheless, the overall mechanical behavior of the resulting TRC composite varied according to the type of coating.

The TRC with the THRM-coated fabric presented a slightly better mechanical performance than the one with the WBEP-07d. It was observed a difference of approximately 9.09% in the tensile strength and 37.7% in the strain capacity. When

the reinforcement area was considered for the obtention of the stresses, this difference decreased to 6.29%. In TRC composites, when an adequate bond is achieved for a strain-hardening response to occur, the ultimate tensile strength depends mainly on the textile reinforcement, since in the post-cracking stage (Stage III), the stresses are being carried by this phase. Therefore, the approximate results for the tensile strength were expected because, as mentioned before, both series utilized the same carbon textile. The high variation in the strain capacity, however, could be attributed to the better impregnation observed in fabrics with the thermoplastic resin. Since the coating material was able to penetrate deeper into the yarn (see Section 4.1), more filaments were activated once the load was introduced and as a consequence, more filaments were able to contribute to the strain capacity of the composite.

The CONV-EPXY composites presented the highest mechanical performance overall. Although the standard variation was significant, when the stresses were obtained with the composite area, these composites reached a tensile strength of 31.4 MPa, similar to the CONV-THRM series. In comparison to the CONV-WBEP-07d composites, the CONV-EPXY specimens presented a slightly higher average (about 9.79%). Nonetheless, the difference in ultimate strength of this series to the other TRC composites was quite significant when the reinforcement area was used to obtain the stresses. In this case, the tensile strength was approximately 40% and 49% higher than the ones of the CONV-THRM and CONV-WBEP-07d specimens, respectively.

The mechanical behavior of a composite depends on the properties of the matrix, the reinforcement, and the adhesion between them [113]. The weakest variable controls the performance of the material. The enhanced mechanical behavior of the TRC with the solvent-based epoxy fabric can be explained by the better impregnation level of this textile. With better impregnation, more filaments are able to contribute to the load-bearing capacity of the TRC. As discussed in Section 4.1, the higher impregnation level of the EPXY yarns is related to the commercial nature of this fabric, in which the coating process was conducted on an industrial scale and not manually, as was the case of the THRM and WBEP-07d textiles.

Furthermore, the superior tensile response of the CONV-EPXY could be attributed to a higher bond strength formed by this reinforcement with the

cementitious matrix. Although an adequate bond seems to have been formed in all three composites, the EPXY-coated textile appeared to have achieved a higher bond strength with the matrix. This assumption can be corroborated by the conducted DIC analysis, as the number of cracks and the distance between them can be related to the textile-matrix bond.

The cracking pattern of the composites was analyzed through Digital Image Correlation (DIC) technique. The cracking pattern of the CONV-UNCO, CONV-WBEP-07d, CONV-THRM, and CONV-EPXY specimens at ultimate strength, just before failure, can be seen in Figure 4.7. Table 4.4 shows the number of cracks in the transversal direction (# cracks), average cracking opening ($w_{m,max}$) and mean crack spacing ($s_{m,max}$) at the ultimate tensile strength in the direct tensile tests.

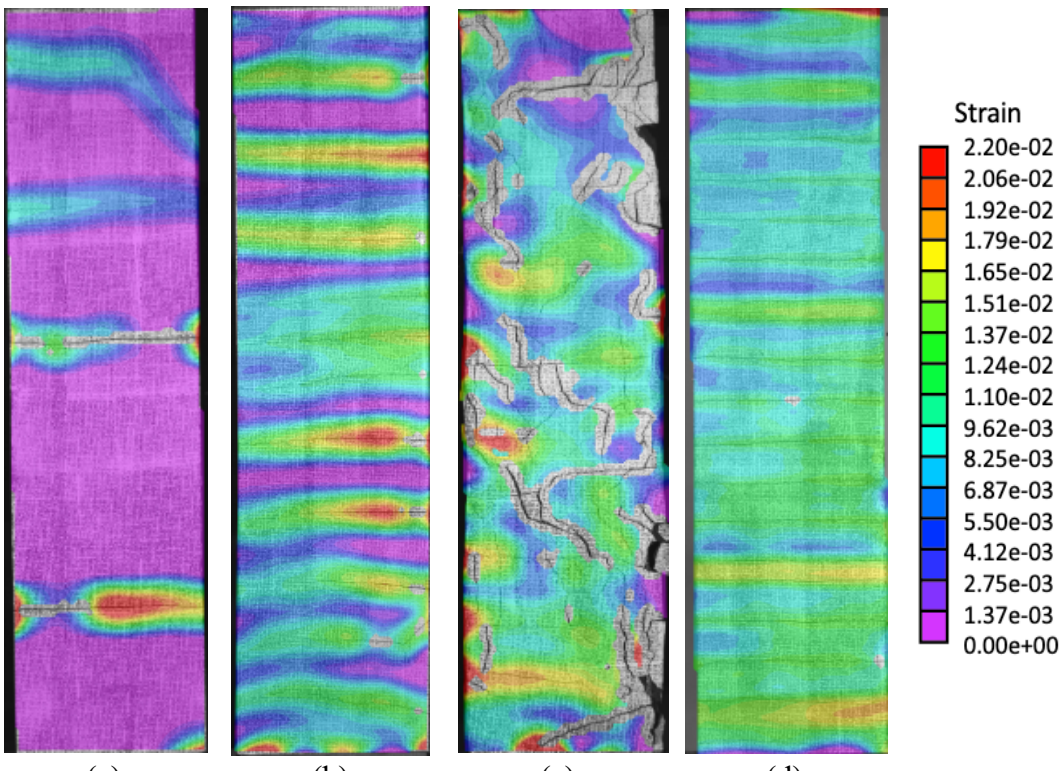


Figure 4.7 - Crack pattern before failure of carbon TRC composites: (a) CONV-UNCO, (b) CONV-WBEP-07d, (c) CONV-THRM, and (d) CONV-EPXY.

Table 4.4 - Average results of DIC cracking analysis of the CONV-UNCO, CONV-WEBP-07d, CONV-THRM, and CONV-EPXY composites at the ultimate load.

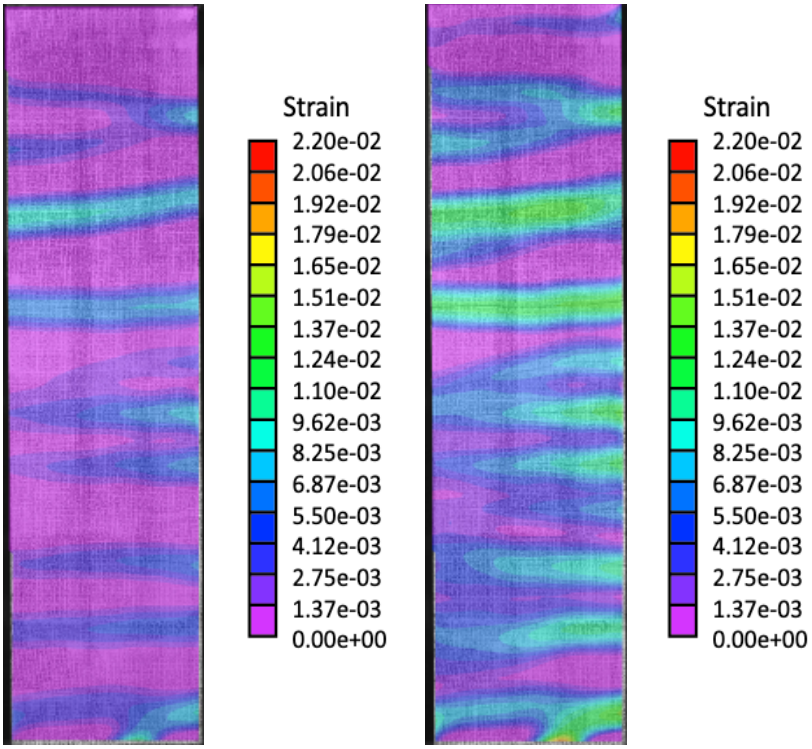
Composite	# cracks	$w_{m,max}$ (μm)	$s_{m,max}$ (mm)
CONV-UNCO	3.50 (0.866)	184.7 (121.0)	251.6 (125.4)
CONV-WBEP-07d	13.6 (1.20)	62.4 (12.7)	30.7 (4.95)
CONV-THRM	9.40 (1.02)	116.7 (63.1)	43.7 (3.53)
CONV-EPXY	17.4 (3.38)	47.4 (13.9)	28.1 (5.15)

As seen in Figure 4.7, the CONV-EPXY series presented more cracks than the CONV-WBEP-07d and CONV-THRM composites, and these cracks were less spaced and smaller (see Table 4.4) on average. The formation of smaller and less spaced cracks indicates a more efficient stress transfer between the matrix and reinforcement [61], achieved by better textile-matrix bond. This also explains why both CONV-WBEP-07d and CONV-THRM series exhibited a higher number of finer and less spaced cracks than the CONV-UNCO composites, as can be noted in Table 4.4.

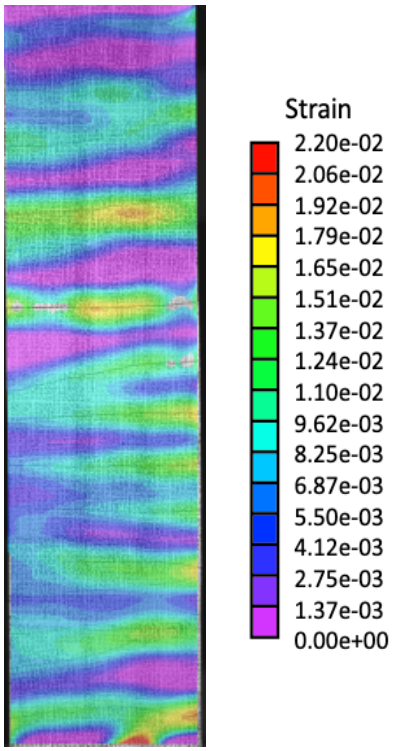
Overall, the CONV-THRM composites exhibited the worst cracking pattern among the series with the coated textiles. These composites showed a significant diffused cracking pattern, characterized by cracks in multiple directions. In comparison, the cracks in the CONV-WBEP-07d specimens were more evenly distributed and considerably narrower (46.5%).

Figure 4.8 exhibits the evolution of the cracks of the CONV-WBEP-07d, CONV-THRM, and CONV-EPXY composites throughout the test. It is possible to see in Figure 4.8 that, in the CONV-THRM composites, the cracks initially appeared in the horizontal direction, similar to the specimens of other variables. However, as the test progressed, vertical cracks began to emerge. During the post-cracking stage, the vertical cracks eventually “merged” with the horizontal ones due to the widening of the cracks, resulting in a network of cracks in multiple directions.

CONV-WBEP-07d



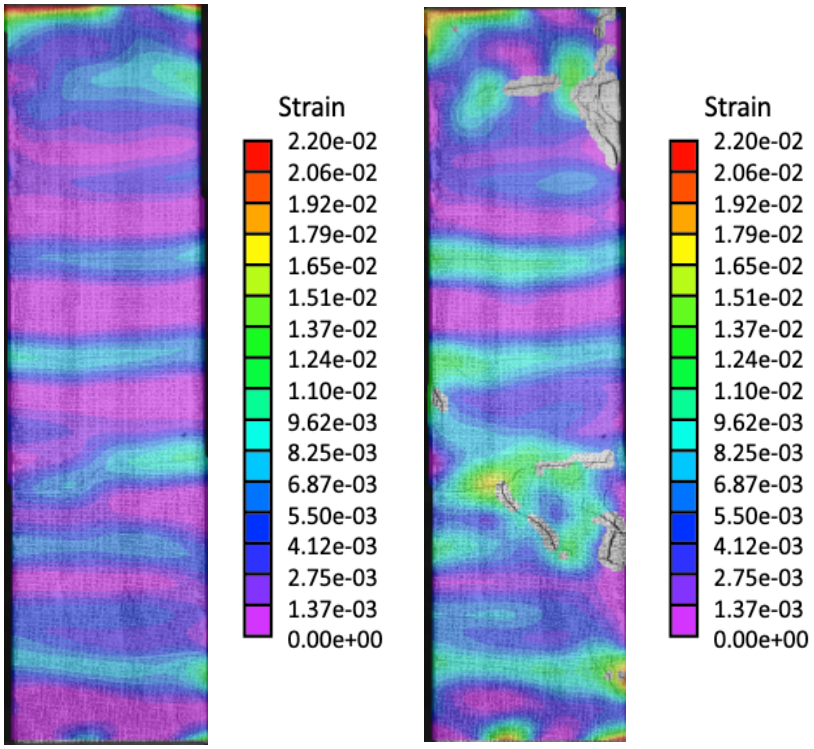
Strain 0.30% Strain 0.60%



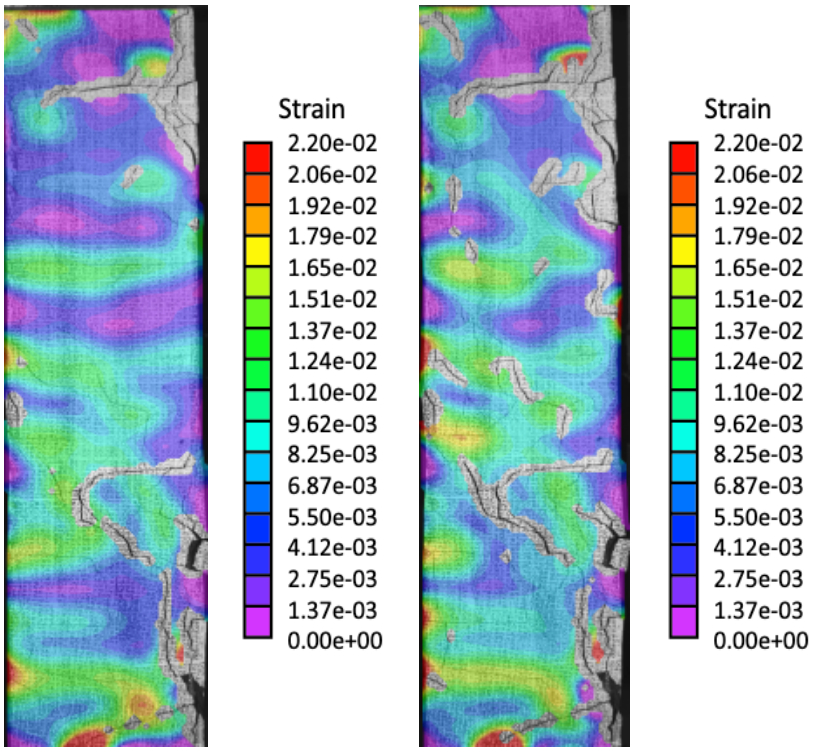
Strain 0.90% /

Strain 1.10%

CONV-THRM



Strain 0.30% Strain 0.60%



Strain 0.90% Strain 1.10%

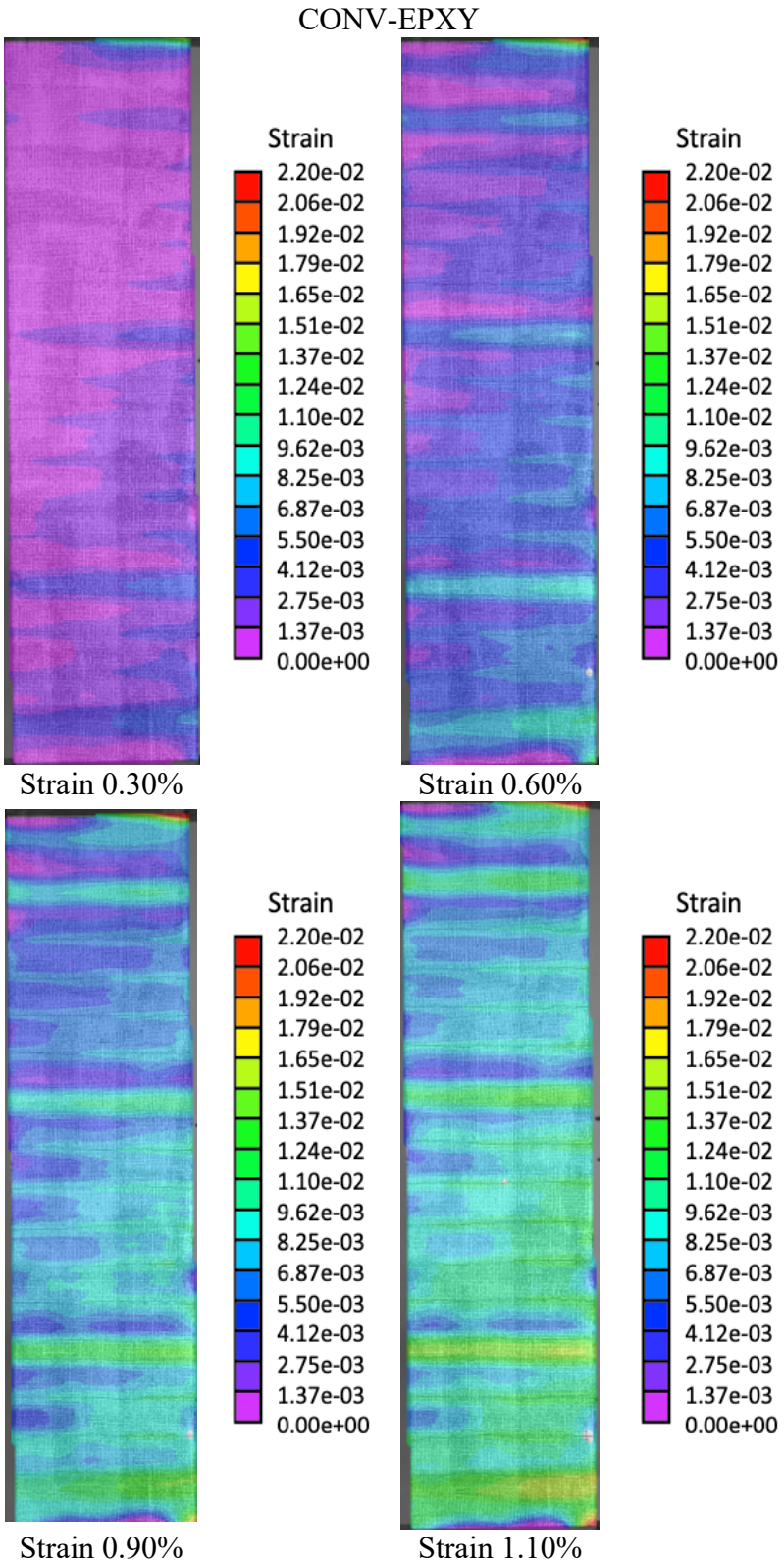


Figure 4.8 - Crack pattern on the CONV-WBEP-07d, CONV-THRM, and CONV-EPXY composites at various strain levels.

Although all three composites presented a brittle failure, characterized by the sudden drop in the load-bearing capacity of the specimens, different failure modes

were observed. In the case of the CONV-EPXY and CONV-THRM composites, the failure was characterized by concrete spalling in the gauge length region, with the THRM variation presenting severe spalling (see Figure 4.9). For the CONV-WBEP-07d, no spalling was observed and these composites failed in the clapping zone, possibly due to stress concentration caused by the manual application of the torque on the screws.

The occurrence of concrete spalling is related to the lack or a poor chemical adhesion between the textile reinforcement and the cementitious matrix [113]. Thus, it can be assumed that mechanical interlock is the main bond mechanism developed by both EPXY and THRM coatings. Moreover, the considerable spalling observed in the CONV-THRM series could be attributed to cross-sectional geometry of the reinforcement. As discussed in Section 4.1, the warp yarns of the fabric with the thermoplastic coating presented a narrower elliptical geometry than the other textiles. Circular or narrower elliptical shapes may cause the formation of cracks in the longitudinal direction [113], which can lead to spalling of the concrete cover [135].



Figure 4.9 - TRC with the thermoplastic-coated textile after the direct tensile test.

The thermoplastic coating yields composites with a significantly superior mechanical performance compared to the SBR coating. Previous studies have reported [103,104] tensile strengths for TRC with SBR-coated fabrics in the range of 6.33-6.49 MPa. Moreover, through a DIC analysis, Goliath *et al.* [104] reported a mean crack width at the ultimate strength of 0.52 mm for these composites. Thus, in terms of tensile strength and cracking behavior, the thermoplastic coating offers a significant advantage over SBR, showing an ultimate strength of about 381% greater and finer cracks (approximately 345% smaller). In this way, this coating could be a suitable alternative to SBR in applications that require textile

reinforcements with design flexibility, as the thermoplastic coating allows for the modification of the fabrics' geometry once the resin is heated. Nonetheless, the viability of thermoplastic coatings as an alternative to SBR coatings hinges on the implementation of simple and effective methods for reshaping fabrics with thermoplastic impregnation. This is because, for example, when bending a textile, all warp yarns in the desired area must be heated simultaneously.

While the WBEP-07d coating did not exhibit the same level of performance as EPXY, it still provided composites with good tensile response. Given that the impregnation was performed manually, it was anticipated that specimens with the solvent-based EPXY-coated textiles would perform better. With a higher level of impregnation, potentially achieved through industrial processes with better technological control, it is possible that the WBEP-07d coating could match EPXY's tensile strength. Despite these differences, the results highlight the promising potential of the WBEP coating as an alternative to EPXY, particularly due to its possible contribution to a better chemical bond and the sustainability advantages it offers, related to its lower levels of VOC emissions.

4.2.2. Influence of the curing time of the WBEP resin coating

Figure 4.10 exhibits the representative tensile stress *vs.* strain curves of the composites with the different curing times of the WBEP coating. The average results for the first crack tensile stress (σ_{cr}), strain at the first crack stress (ε_{cr}), tensile strength (σ_{max}), strain at tensile strength (ε_{max}), and the standard deviation of these composites are presented in Table 4.5.

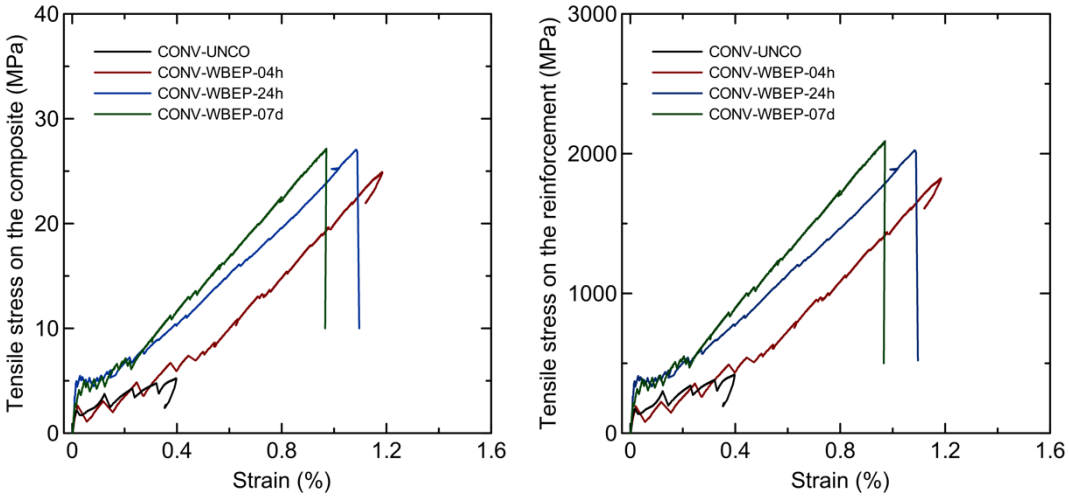


Figure 4.10 - Representative tensile stress *vs.* strain curves for the CONV-UNCO, CONV-WBEP-04h, CONV-WBEP-24h, CONV-WBEP-07d, CONV-THRM and CONV-EPXY carbon TRC composites, calculating the stresses with the (a) composite area and (b) reinforcement area.

Table 4.5 - Average results of the direct tensile tests for the CONV-WBEP-04h, CONV-WBEP-24h, and CONV-WBEP-07d carbon TRC composites.

Composite	$\sigma_{cr,CA}$ (MPa)	ε_{cr} (%)	$\sigma_{max,CA}$ (MPa)	$\sigma_{max,RA}$ (MPa)	ε_{max} (%)
CONV-UNCO	2.00 (0.189)	0.0205 (0.00537)	4.70 (0.444)	378.6 (29.7)	0.309 (0.0863)
CONV-WBEP-04h	2.94 (1.62)	0.0390 (0.0345)	26.4 (5.10)	1942.9 (116.8)	1.22 (0.321)
CONV-WBEP-24h	2.65 (0.508)	0.0123 (0.00274)	30.0 (2.85)	2146.0 (84.8)	1.10 (0.119)
CONV-WBEP-07d	2.51 (0.568)	0.0128 (0.00532)	28.6 (1.10)	2060.3 (87.5)	0.966 (0.0457)

$\sigma_{cr,CA}$ – first crack stress (obtained using the cross-sectional area of the composite).
ε_{cr} – first crack strain.
$\sigma_{max,CA}$ – ultimate tensile strength (obtained using the cross-sectional area of the composite).
$\sigma_{max,RA}$ – ultimate tensile strength (calculated using the reinforcement area).
$\varepsilon_{\sigma,max}$ – ultimate strain.

In Figure 4.10, it can be observed that all three variations of the WBEP series exhibited a considerable enhanced tensile response in comparison to the composites with the uncoated textiles. The tensile strength increased in 462%, 538%, 509% for the CONV-WBEP-04h, CONV-WBEP-24h, CONV-WBEP-07d composites, respectively, in comparison to the CONV-UNCO series, when the stresses were obtained using the composite area. When the tensile stresses were calculated using the reinforcement area, this improvement was 413% (CONV-WBEP-04h), 467% (CONV-WBEP-24h), 444% (CONV-WBEP-07d). Moreover, the strain capacity of the composites was improved in 296% (WBEP-04h), 255% (WBEP-24h), 213%

(WBEP-07d). This indicates that the bond with the cementitious matrix was improved by all three curing times in relation to the uncoated textiles.

It is interesting to note that the curing time of the WBEP resin did not seem to have a significant influence on the tensile strength of the carbon TRC, as can be seen in Figure 4.10. While the standard deviation of the CONV-WBEP-04h series was relatively high, the variations in the maximum tensile stresses between the different series were not higher than 13.6% when considering the obtention of the tensile stresses with the composite area. When the tensile strength was calculated using the reinforcement area, this difference was not higher than 10.5% (WBEP-24h *vs.* WBEP-04h). As explained, while in the linear elastic stage and in the multiple-cracking stage the stresses are carried by the matrix and by both phases, respectively, in the post-cracked stage (Stage III), the tensile strength of TRC is generally dependent on the mechanical properties of the textile reinforcement, as only the reinforcement contributes to the load-bearing capacity of the composite. Hence, considering that all three WBEP series utilized the same textile reinforcement and the same coating material, it was expected they presented similar tensile strengths.

Despite not having a substantial effect on the tensile strength, the curing time of the water-dispersed epoxy resin had a considerable impact on the multiple-cracking behavior of the composites, which was analyzed with a DIC technique. Table 4.6 presents the results of the DIC analysis for the number of cracks in the transversal direction (# cracks), average cracking opening ($w_{m,max}$) and mean crack spacing ($s_{m,max}$) at the ultimate tensile strength in the direct tensile tests. Figure 4.11 shows the cracking pattern of the composites with the water-based epoxy-coated textile before failure.

Table 4.6 - Average results of DIC cracking analysis of the TRC composites at the ultimate load.

Composite	# cracks	$w_{m,max}$ (μm)	$s_{m,max}$ (mm)
CONV-UNCO	3.50 (0.866)	184.7 (121.0)	251.6 (125.4)
CONV-WBEP-04h	6.80 (1.47)	134.2 (32.6)	68.2 (14.1)
CONV-WBEP-24h	11.8 (1.94)	72.4 (35.0)	36.6 (11.4)
CONV-WBEP-07d	13.6 (1.20)	62.4 (12.7)	30.7 (4.95)

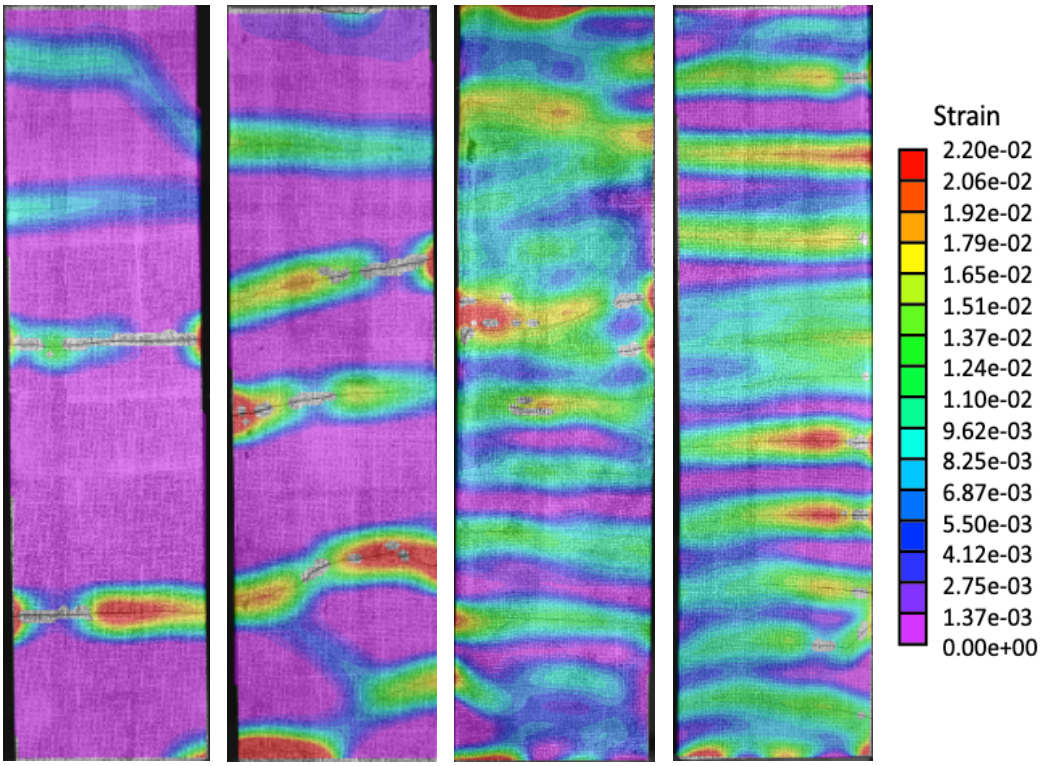


Figure 4.11 - Crack pattern before failure of carbon TRC composites: (a) CONV-UNCO, (b) CONV-WBEP-04h, (c) CONV-WBEP-24h, and (d) CONV-WBEP-07d.

From Figure 4.11, it is possible to note that lower curing times (in this case 4 hours) led to fewer and more widely spaced cracks. Moreover, through the DIC analysis, it was observed that these cracks were also bigger (see Table 4.6). Whereas the CONV-WBEP-24h series presented better multiple-cracking behavior than the CONV-WBEP-04h, the subsequent increase in the curing time of the resin up to 7 days led to an even better enhancement of the cracking pattern. The DIC analysis showed that the TRC composites with the 7 day-cured water-based epoxy fabric exhibited a more uniform cracking pattern than the specimens with the textiles where the coating cured for 24 hours. Not only the cracks were formed mainly in the horizontal direction in CONV-WBEP-07d variation, but they were also less spaced and smaller in comparison to the CONV-WBEP-24h series, as can be observed in Table 4.6.

The inferior cracking behavior of the composites with the WBEP-04h fabric could be attributed to a weaker bond strength between the cementitious matrix and the textile reinforcement. As mentioned before, smaller and less spaced cracks are formed when higher bond strengths are obtained due to a more efficient stress transfer between these two phases [61]. The lower bond of the fabrics with the

matrix in this series could be linked to a weaker interface. Due to the water-based nature of the resin, the matrix might have absorbed part of the water that was still present in the resin after only four hours of curing in the air. This could have resulted in a higher water-cement ratio in this region, creating a more porous interface and as a consequence, a poorer bond.

Furthermore, the manipulation of the WBEP-04h fabrics, which were removed from the frame and cut to the desired size right before casting the composites, might have caused a misalignment of the internal filaments, since the incomplete curing of the resin allows the filaments to move relatively freely. As a result of the misalignment of the inner filaments, an uneven stress distribution and the inability to activate all filaments might have occurred, leading to the inferior multiple cracking behavior.

As already mentioned, the curing process of the WBEP resin takes approximately 24 hours, according to Scheurer *et al.* [17]. Therefore, by the time the fabrics were handled and prepared for casting the CONV-WBEP-24h and CONV-WBEP-07d composites, the filament movement was restrained by the cured coating, thereby explaining the superior cracking pattern observed in these two series in comparison to the CONV-WBEP-04h specimens.

The difference in the cracking pattern between the CONV-WBEP-24h and CONV-WBEP-07d series could be attributed to the technical properties of the water-dispersed epoxy resin. According to the manufacturer's datasheet [131], the full resistance of this resin is achieved after 7 days. Thus, since the full resistance of this material was not achieved in the composites with textiles that the resin cured in the air for 24 hours prior to casting, the concrete environment might have affected, slowed or even inhibited somehow the chemical reactions responsible for the resistance gain once the reinforcement was cast into concrete. Conversely, in the case of the CONV-WBEP-07d specimens, the resin was able to achieve its full strength before the composites were cast, resulting in a superior cracking behavior.

These results differ from those obtained by Scheurer *et al.* [17], who compared the tensile behavior of TRCs with carbon rovings coated with the water-dispersed resin cured inside (cast inside immediately after impregnation) and outside concrete. The authors reported that the composites with the cured inside resin only reached about 70.4% of the average tensile strength of those with the

cured outside. Additionally, it was observed that the cured inside series presented slightly more evenly distributed cracks.

The failure mode of the composites with the WBEP-coated fabrics was also affected by the curing time. The CONV-WBEP-04h series had a failure mode characterized by the textile pull-out instead of its rupture, similar to the failure observed in the composites with uncoated textiles. This corroborates the argument that the textile-matrix bond is inferior in composites in which the resin cures inside than the ones where the curing process of the resin is more advanced prior to the composite manufacturing. For the CONV-WBEP-24h composites, a brittle failure with partial rupture of the outer filaments in the gauge length region was observed, as illustrated in Figure 4.12. The failure of outer filaments indicates that the full mechanical properties of the carbon fabrics were not utilized due to the more superficial coating of this resin (see Section 4.1). In addition, some specimens of this series exhibited concrete spalling. While the CONV-WBEP-07d series did not present spalling, as previously mentioned, the specimens had a premature failure in the clapping zone, which could be a result of stress concentration caused by the manual application of the torque on the screws.

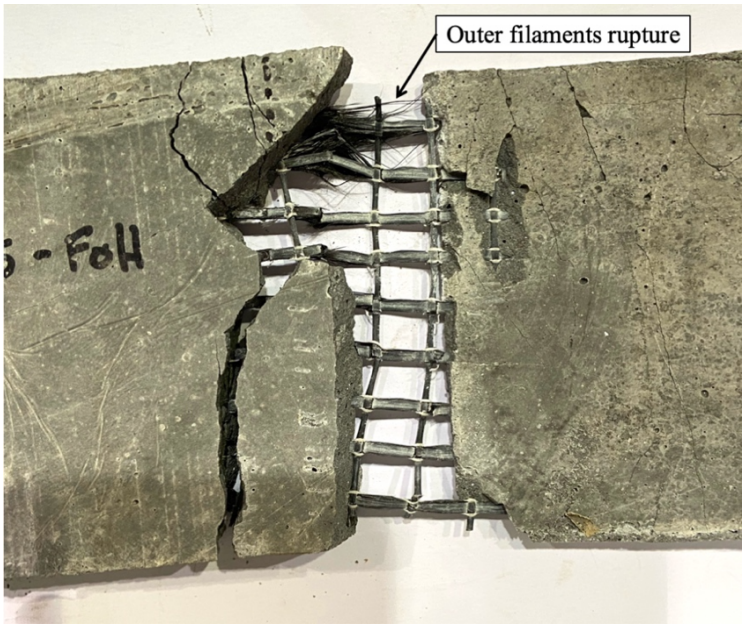


Figure 4.12 - TRC composite with the WBEP-24h fabric after the direct tensile test.

In the case of high-performance textiles such as carbon fabrics, the pull-out of the reinforcement is not desired, since the failure of the composite occurs way

before the total capacity of the fiber and thus, the elevated properties offered by these textiles are not completely utilized. As carbon fibers are quite expensive, costing about 20 euros per meter [116], it is desired to utilize their full mechanical properties. Therefore, in applications where high mechanical properties and superior cracking behavior are required, the curing of the WBEP resin for 7 days prior to casting is more appropriate than curing the textile for only 4 hours, for example. Nonetheless, in applications where design flexibility is prioritized, the use of lower curing times could be a good alternative because the textiles still retain their flexibility and yield composites with a superior mechanical behavior than the uncoated fabric.

4.2.3. Influence of the UHPC matrix

Figure 4.13 exhibits the representative tensile stress *vs.* strain curves for the CONV-EPXY and UHPC-EPXY composites. Table 4.7 lists the average results for the first crack tensile stress (σ_{cr}), strain at the first crack stress (ε_{cr}), tensile strength (σ_{max}), strain at tensile strength (ε_{max}), and the standard deviation of these composites.

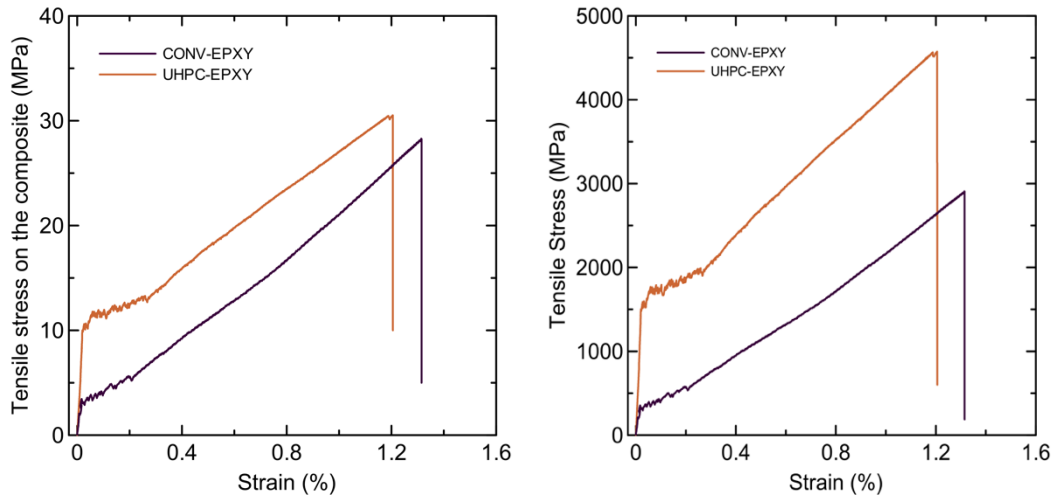


Figure 4.13 - Representative tensile stress *vs.* strain curves for the CONV-EPXY and UHPC-EPXY carbon TRC composites, calculating the stresses with the (a) composite area and (b) reinforcement area.

Table 4.7 - Average results of the direct tensile tests for the CONV-EPXY and UHPC-EPXY carbon TRC composites.

Composite	$\sigma_{cr,CA}$ (MPa)	ε_{cr} (%)	$\sigma_{max,CA}$ (MPa)	$\sigma_{max,RA}$ (MPa)	ε_{max} (%)
CONV-EPXY	2.89 (1.38)	0.0107 (0.00651)	31.4 (11.9)	3068.7 (405.2)	1.27 (0.151)
UHPC-EPXY	8.61 (1.04)	0.0210 (0.00694)	32.2 (3.21)	4209.0 (315.2)	1.24 (0.115)

$\sigma_{cr,CA}$ – first crack stress (obtained using the cross-sectional area of the composite).
ε_{cr} – first crack strain.
$\sigma_{max,CA}$ – ultimate tensile strength (obtained using the cross-sectional area of the composite).
$\sigma_{max,RA}$ – ultimate tensile strength (calculated using the reinforcement area).
$\varepsilon_{\sigma,max}$ – ultimate strain.

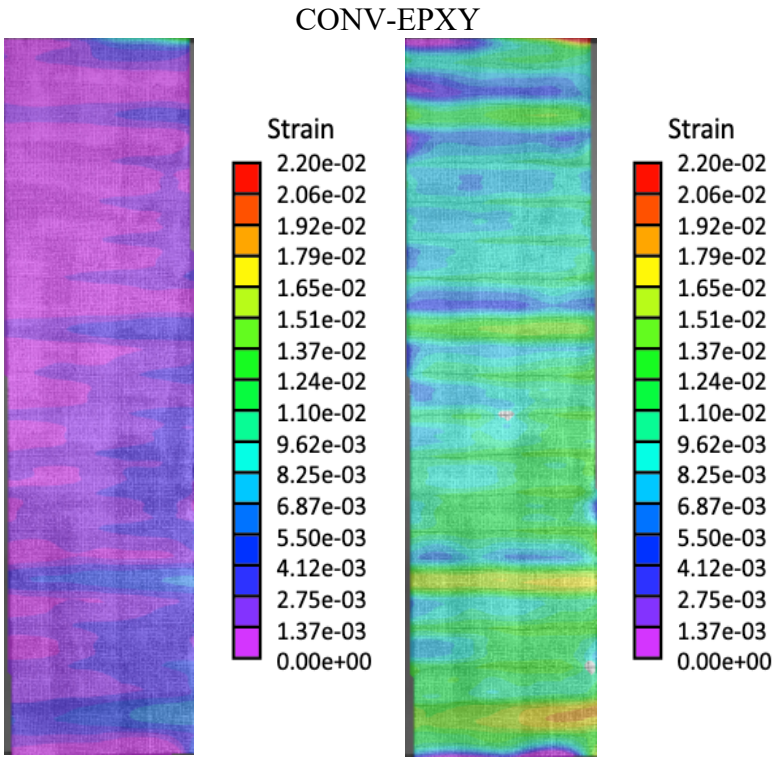
Both types of composites with the epoxy-impregnated fabric exhibited the characteristic strain-hardening behavior of TRC described in Section 4.4.1. It is possible to see in Figure 4.13a that both CONV-EPXY and UHPC-EPXY series reached similar average tensile strengths when the stresses were obtained using the composite area (with the UHPC composites showing an increase in strength of only 2.55% compared to those with conventional matrix). Whereas in Figure 4.13b, it can be observed that the composites with the UHPC outperformed those with the conventional matrix when the stresses were obtained using the reinforcement area. In this case, the use of the UHPC matrix yielded an improvement of 37.2% in the ultimate tensile strength. These results highlight the contribution of the steel fibers to the mechanical performance of the composite. After failure, it was possible to observe in some specimens that the steel fibers were mainly oriented in the longitudinal direction of the composites, as can be seen in Figure 4.14. Thus, their contribution to the tensile strength of the composite was significant. The orientation of the fibers in the main stress direction could be attributed to the hand lamination technique used to cast the specimens and the small mesh opening of the textiles [77]. Yao *et al.* [96] also reported this phenomenon in their study in UHPC specimens with textile reinforcements.



Figure 4.14 - Fiber orientation on the UHPC-EPXY composites subjected to the tensile tests.

The first crack strength was also significantly improved for the composites in which the UHPC matrix was used. While the average first crack stress of the CONV-EPXY series was 2.89 MPa, that of the UHPC-EPXY specimens was 8.61 MPa, a difference of 197.9%. The stress level at which the first crack opens depends directly on the tensile properties of the cementitious matrix. In the case of fiber reinforced concrete, these properties are related to the type of fiber, volume fraction, and fiber-matrix interface [61,79]. In this way, this great difference can be attributed to the higher tensile strength of UHPC. Previous studies have reported that the tensile strength of UHPC matrices can vary from 8 MPa to 15 MPa [96,136]. These results are in accordance with those obtained by Yao *et al.* [96] for carbon TRC with an ultra-high performance concrete matrix.

The difference in the cracking behavior of the composites with the UHPC and CONV matrices was analyzed through a DIC technique. Figure 4.15 displays the cracking pattern of the CONV-EPXY and UHPC-EPXY composites at the end of Stage II and before failure. Table 4.8 presents the results of the DIC analysis for the number of cracks in the transversal direction (# cracks), average cracking opening at the end of Stage II ($w_{m,SII}$), average cracking opening ($w_{m,max}$) and mean crack spacing ($s_{m,max}$) at the ultimate tensile strength in the direct tensile tests.



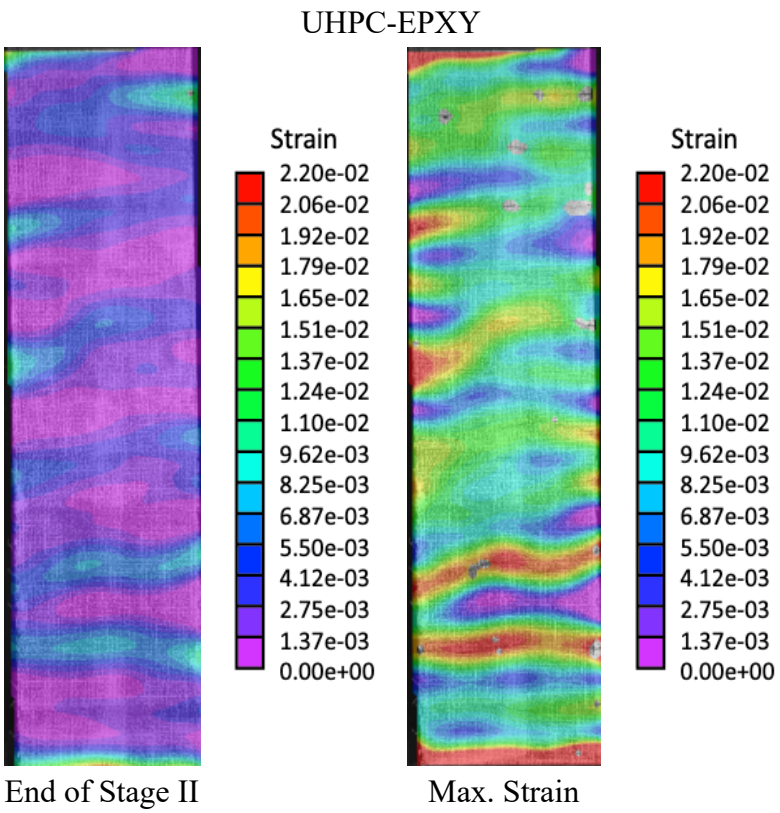


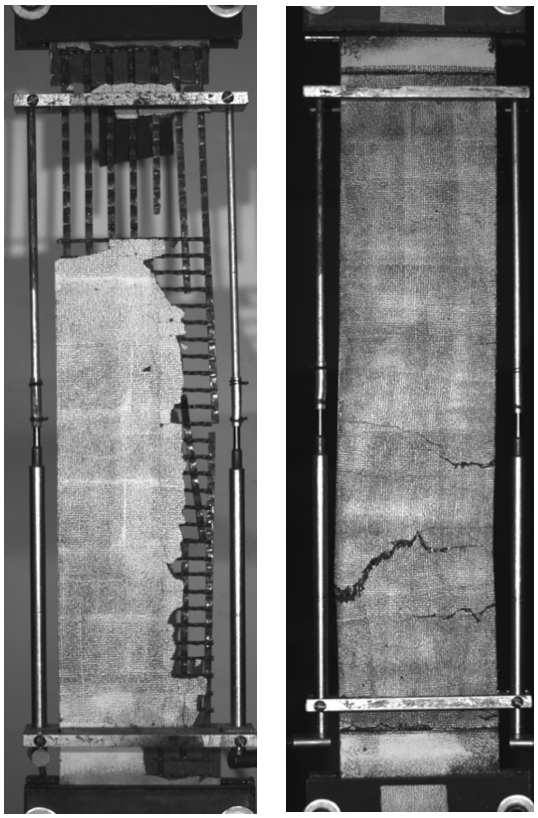
Figure 4.15 - Crack pattern on the CONV-EPXY and UHPC-EPXY composites at the end of Stage II and at the maximum strain (right before failure).

Table 4.8 - Average results of DIC cracking analysis of the TRC composites at the ultimate load.

Composite	# cracks	$w_{m,SII}$	$w_{m,max}$ (μm)	$s_{m,max}$ (mm)
CONV-EPXY	17.4 (3.38)	17.5 (5.15)	47.4 (13.9)	28.1 (5.15)
UHPC-EPXY	10.2 (2.63)	9.26 (2.35)	43.9 (13.7)	38.5 (3.81)

As can be seen in Table 4.8, more cracks were formed on average in the CONV-EPXY specimens than in the UHPC-EPXY variation (17.4 *vs.* 10.2, respectively). In addition, in the CONV-EPXY, these cracks were more evenly distributed, that is, the distance between cracks was smaller (28.1 mm) than in the series with the UHPC matrix (38.5 mm). Despite that, it can be noticed in Table 4.8 that the UHPC-EPXY composites presented smaller cracks. The contribution of the UHPC can be specially noted that the end of Stage II, where the crack width was 47.1% smaller than in the CONV-EPXY series. This significant difference in crack widths can be explained by the bridging mechanism provided by the short steel fibers incorporated into the UHPC matrix. This mechanism helps control the crack propagation, besides improving the energy-absorbing capacity of the composite and the overall performance under tensile loads.

The characteristic failure modes of the composites with the EPXY fabric are shown in Figure 4.16. Although both series failed due to the reinforcement rupture, it is possible to perceive in Figure 4.16 that the rupture of the CONV-EPXY series was characterized by concrete spalling. Conversely, the UHPC composites did not exhibit spalling. This can be once again attributed to the presence of the steel fibers in the matrix, which acted more efficiently in bridging the cracks. The lack of spalling on the UHPC composites indicates it is a safer option for the user's safety in practical applications. Moreover, the UHPC matrix also seems to be a better option than the conventional matrix in terms of the serviceability of structures since it presents a finer crack pattern, which is more advantageous from a structure durability point of view.



(a) (b)

Figure 4.16 - Failure mode of the carbon TRC composites: (a) CONV-EPXY and (b) UHPC-EPXY.

4.3. Flexural behavior of carbon TRC I-section beams

4.3.1. Influence of surface coating

The load *vs.* deflection curves of the CONV-WBEP-240, CONV-THRM-240 and CONV-EPXY-240 carbon TRC beams are presented in Figure 4.17. The main test results can be seen in Table 4.9.

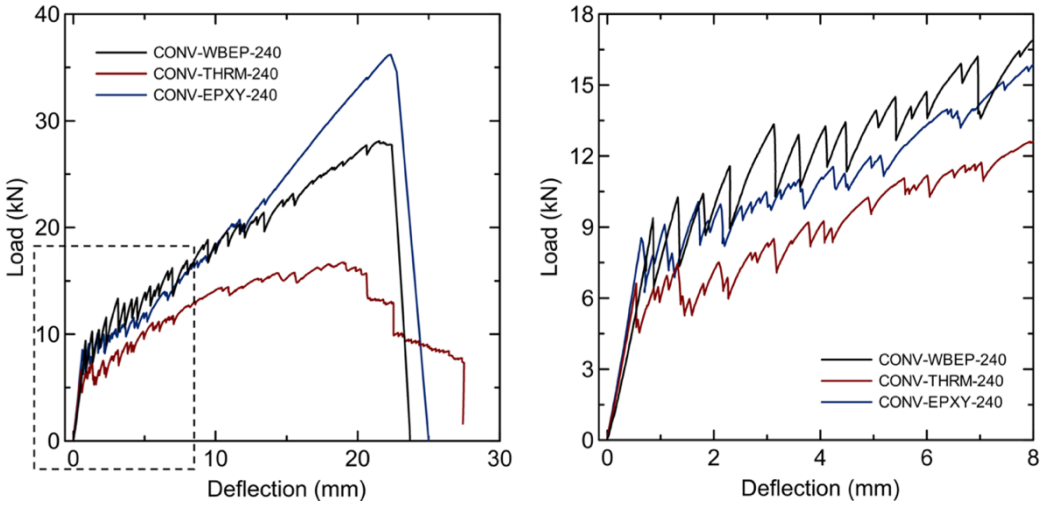


Figure 4.17 - Load *vs.* deflection curves for the CONV-WBEP-240, CONV-THRM-240, and CONV-EPXY-240 carbon TRC beams: (a) overview and (b) detail for low deflections.

Table 4.9 - Main results obtained from the four-point bending tests on the carbon TRC I-section beams: CONV-WBEP-240, CONV-THRM-240, and CONV-EPXY-240.

	CONV-WBEP-240	CONV-THRM-240	CONV-EPXY-240
F_{max} (kN)	28.1	16.7	36.2
$\delta_{F,max}$ (mm)	21.5	19.0	22.3
M_{max} (kNm)	10.5	6.28	13.6
$\Phi_{M,max}$ (1/m)	0.0164	0.00730	0.0485
F_{cr} (kN)	7.74	6.62	8.55
$\delta_{F,cr}$ (mm)	0.731	0.543	0.637
Failure mode	Shear	Shear	Shear

F_{max} – maximum load at mid-span.
δ_{Fmax} – maximum deflection at mid-span at the maximum load.
M_{max} – maximum moment.
$\Phi_{M,max}$ – curvature at maximum bending moment.
F_{cr} – first crack load.
δ_{Fcr} – deflection at the first crack load.

The CONV-EPXY-240 presented the highest maximum load, followed by the CONV-WBEP-240 and CONV-THRM-240 beams, respectively. The difference in ultimate load of the beam with the EPXY-coated textile to the ones with the WBEP and THRM coatings was 28.8% and 116.7%, respectively. This enhanced load-bearing capacity observed in the CONV-EPXY-240 was, however, expected due to the better impregnation and higher textile-matrix bond, as reported in the direct tensile tests.

It is interesting to note that despite the CONV-THRM-240 utilizing the same carbon fabric reinforcement and demonstrating slightly superior mechanical

properties in tensile tests compared to the composites with the WBEP-coated fabric (see Section 4.2.1), this response did not translate to the structural scale. The CONV-THRM-240 beam exhibited a significantly lower load-bearing capacity than the CONV-WBEP-240, achieving only 40.7% of the ultimate load of the beam with the WBEP fabric, which highlights the critical role of textile-matrix bond in translating material-level properties to structural behavior. This inferior behavior and the unclear typical three-stage curve, however, can be related to the failure mechanism that was observed in this beam, as it will be further discussed below.

The Brazilian Standard for the design of concrete structures (ABNT NBR 6118) [6] defines $l/250$, in which l is the beam span, as the maximum deflection of steel RC beams for the Serviceability Limit State (SLS). For a span of 1800 mm, the maximum deflection allowed for the beams would be 7.2 mm. For this displacement, the applied loads on the CONV-WBEP-240, CONV-THRM-240, and CONV-EPXY-240 carbon TRC beams were approximately 14.5, 11.5, and 14.7 kN, which account for about 51.6%, 68.9%, and 40.6% of their load-bearing capacities, respectively. These results show that although carbon textile reinforcements lack yielding capacity upon failure, the ultimate load-bearing capacities of the beams were well above the loads corresponding to the deflection limits, especially in the case of the CONV-EPXY-240 and CONV-WBEP-240 beams, which indicates the suitability of these materials when considering the structural safety.

The cracking behavior of the TRC beams was evaluated with a DIC technique. Figure 4.18 displays the cracking patterns at the maximum deflection allowed by the SLS (7.2 mm) and right before failure of the beams with different coatings. The results obtained in the DIC analysis for the mean cracking spacing and mean cracking widths at these deflections are reported in Table 4.10.

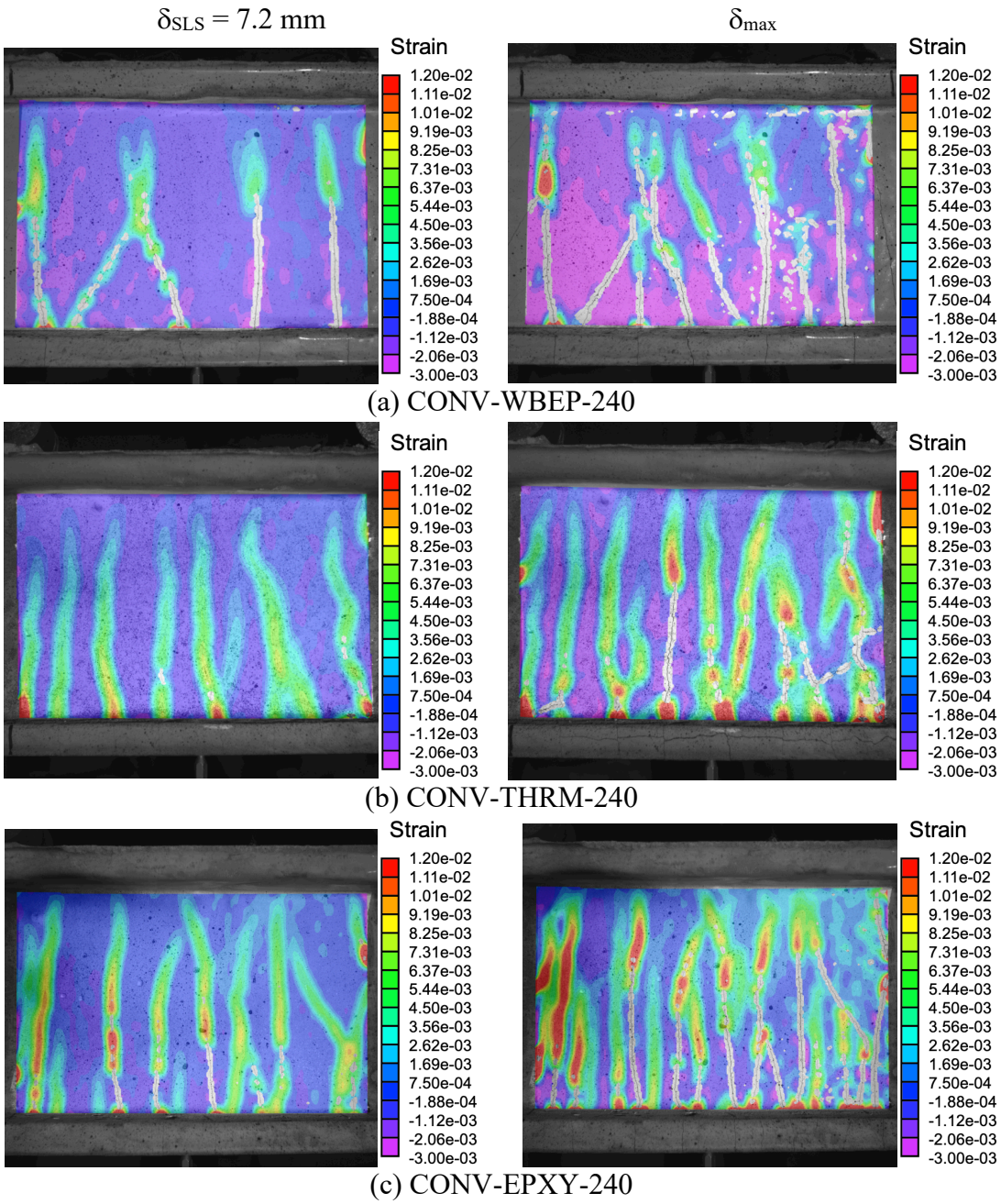


Figure 4.18 - Crack pattern of the (a) CONV-WBEP-240, (b) CONV-THRM-240, and (c) CONV-EPXY-240 at the SLS and at the maximum load before failure.

Table 4.10 - DIC analysis results at different deflection levels for the CONV-WBEP-240, CONV-THRM-240, and CONV-EPXY-240 carbon TRC beams.

	CONV-WBEP-240	CONV-THRM-240	CONV-EPXY-240
$s_{m,SLS}$ (mm)	55.2	33.3	16.4
$s_{m,max}$ (mm)	31.4	33.4	16.5
$w_{m,SLS}$ (μm)	141.5	40.7	47.2
$w_{m,max}$ (μm)	185.1	104.8	110.3

$s_{m,SLS}$ – average cracking spacing on Serviceability Limit State (SLS).
$s_{m,max}$ – average distance between cracks at the maximum load (before rupture).
w_{SLS} – average crack width at the Serviceability Limit State (SLS).
$w_{m,max}$ – average crack width at the maximum load (before rupture).

The CONV-EPXY-240 beam exhibited the finest crack spacing, consistently maintaining an average of 16 mm in both deflections measured (7.2 mm and before failure). The less spaced cracks suggest a more uniform stress distribution across the textile reinforcement and efficient utilization of the carbon fibers. In contrast, the CONV-WBEP-240 beam initially displayed a wide crack spacing of 55 mm at SLS, exhibiting fewer cracks. However, as the load increased, the crack spacing decreased to 31 mm before failure, indicating a denser crack pattern under higher stresses, as seen in Figure 4.18a. The CONV-THRM-240 beam showed an intermediate crack spacing of around 33 mm, which remained relatively consistent between observed deflection levels, indicating a stable crack propagation pattern.

In terms of crack widths, the CONV-WBEP-240 beam exhibited the largest average crack widths, reaching 141.5 μm at SLS and 185.1 μm at maximum load. The CONV-EPXY-240 beam showed moderate crack widths, averaging 47.2 μm at SLS and 110.3 μm at maximum load. These smaller crack widths, coupled with the fine crack spacing, point towards a more controlled crack development process. Despite presenting the worst structural behavior among the specimens, the CONV-THRM-240 beam displayed the smallest crack widths, averaging 40.7 μm at SLS and 104.8 μm at maximum load.

The inferior cracking behavior of the CONV-WBEP-240 beam can be attributed to the lower level of impregnation this textile presented in relation to the THRM and EPXY fabrics (see Section 4.1). With a more superficial coating, fewer filaments were activated during loading and thus, a reduced number of filaments was able to contribute to the multiple-cracking behavior in this beam, resulting in the wider crack spacing and crack widths observed in the CONV-WBEP-240 beam. Despite that, the Brazilian Standard NBR 6118 [6] establishes that, for reinforced

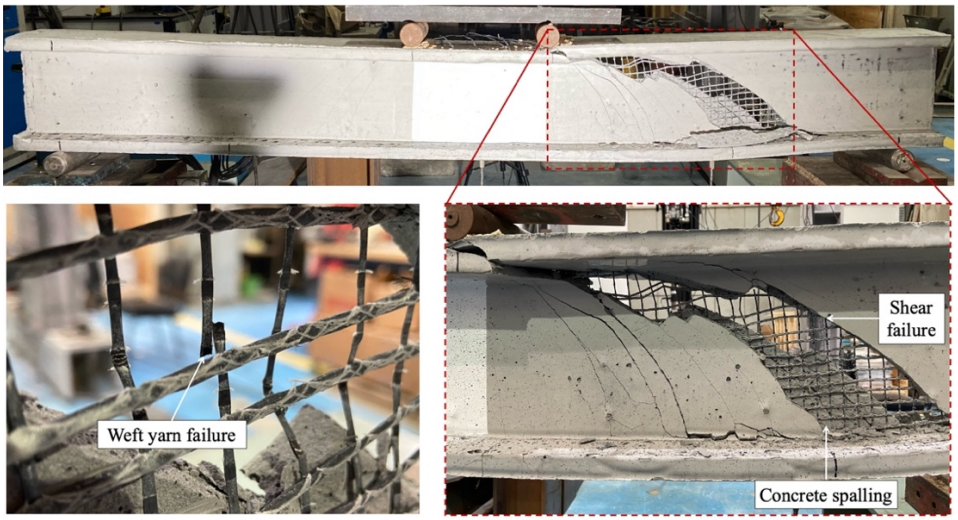
concrete structures, the maximum size for crack opening should range from 0.2 to 0.4 mm, depending on the environmental aggressiveness class, aiming at the protection and durability of the reinforcements. Even considering that carbon textile reinforcements are not subjected to corrosion, the observed crack width values remain within the limits recommended by the standard.

These results indicate that the WBEP coating has the potential to be a viable alternative to the solvent-based epoxy impregnation in practical applications, especially considering that the coating process was conducted manually and at an industrial scale, the impregnation of the reinforcement could be improved, resulting possibly in an even better behavior.

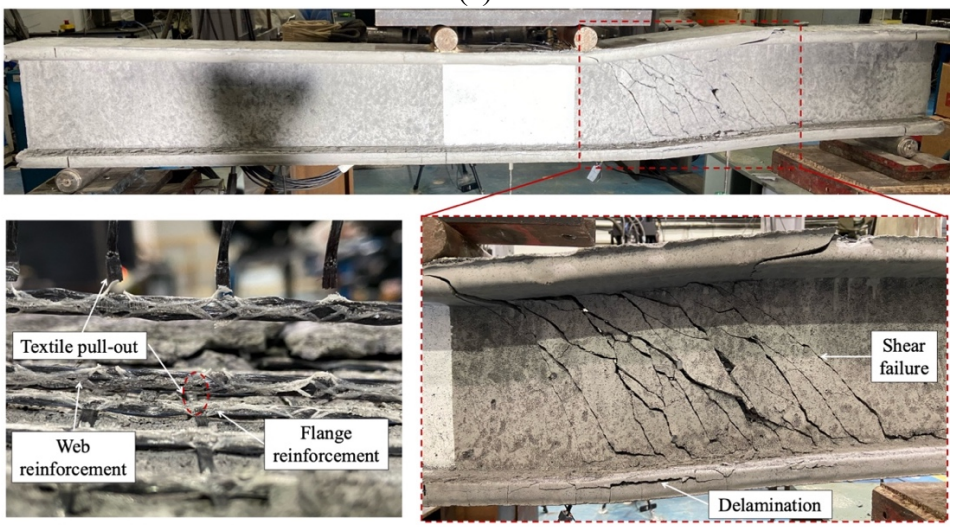
Figure 4.19 shows the failure modes of the carbon TRC beams with conventional matrix and 240 mm section height. All three beams failed by shear. Multiple diagonal cracks were observed on the CONV-WBEP-240 beam in the shear span region prior to failure, which occurred in a brittle manner and was accompanied by concrete spalling in the web area where the failure occurred. After rupture, it was possible to observe total or partial rupture of some weft yarns in the web, as seen in Figure 4.19a. The CONV-THRM-240 beam exhibited several diagonal cracks due to shear stresses, however, the main mechanism involved in the shear failure was the textile pull-out at the flange-web junction. Some delamination between the textile reinforcement and the concrete layers was observed at the bottom flange and at the web of this beam (Figure 4.19b). The textile pull-out in the bottom flange caused the crush of the concrete in the upper flange of the CONV-THRM-240 beam in one of the load application points (see Figure 4.19a and b). The concrete crushing could also be observed in the CONV-WBEP-240 beam. Nonetheless, in this case, it was likely caused by the rupture of the web's weft yarns, which generated an upward force that was counteracted by the load applied by the actuator.

The CONV-EPXY-240 beam failed by shear in the overlap region. The failure of this beam was accompanied by concrete spalling in the web zone as well as in the bottom flange. Furthermore, as in the CONV-THRM-240 beam, delamination between the textile reinforcement and concrete layers was observed on the inferior flange, as shown in Figure 4.19c, although in the beam with the EPXY textile, this delamination was more severe. The excessive delamination can

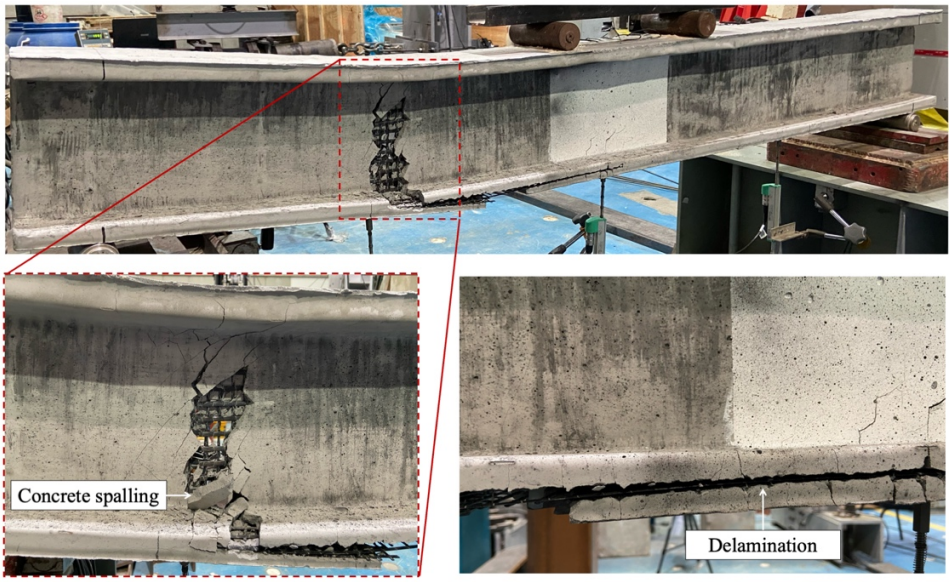
be attributed to the low chemical adhesion of this coating, a solvent-based epoxy resin, with the concrete, as discussed in Section 4.2.1.



(a)



(b)



(c)

Figure 4.19 - Failure modes of the (a) CONV-WBEP-240, (b) CONV-THRM-240, and (c) CONV-EPXY-240 beams.

The premature shear failure observed in the beams can be attributed to several factors. First, due to the way the textiles were available, the fabrics were positioned in the flange with their warp direction aligned longitudinally (perpendicular to the load application). Since the weft yarns present a significantly smaller cross-sectional area compared to the warp yarns, their ability to withstand shear stresses was also considerably smaller, and they were not able to provide sufficient shear crack control. This proved to be more critical for the WBEP and THRM fabric. These fabrics featured weft yarns with smaller cross-sections than the ones in the EPXY textile, which likely contributed to yarn failure observed in the case of the CONV-WBEP-240 beam.

Additionally, the simple method used to create the web-flange connection, which consisted of using wires at specific points along the web-flange junctions, could have hindered the transfer of stresses between the flanges and the web, leading to premature rupture, especially in the case of the CONV-THRM-240 beam. As described in Section 3.3.2, it was desired to form these connections in this reinforcement only by simply using the melting and hardening properties of the thermoplastic resin. Nonetheless, when this method was employed, it was observed that the adhesive bond formed was weak. Thus, wires were also used in some areas of the connection to improve it, however, fewer connection points were “reinforced” in comparison to the other beams. This, combined with the weaker

textile-matrix bond strength, resulted in textile pull-out at the web-flange junction, as seen in Figure 4.19b. This pull-out phenomenon significantly hindered the load-carrying capacity of the beam at an early stage, preventing the full utilization of the fabric's tensile strength, and explaining the inferior behavior exhibited by this specimen when compared to the CONV-WBEP-240 beam, as well as the lack of a clear three-stage flexural behavior typically observed in TRC. This failure, characterized by pullout at the flange-web junction in carbon TRC I-section beams, has also been observed by Goliath *et al.* [126] and Kulas [125]. Goliath *et al.* [126] attributed it to the simple web-flange connection, which was created using a nylon tie to keep the layers of the reinforcement together, a similar process to the one used in this study. Kulas [125] reported that the short anchoring length of the shear reinforcement led to the failure of the test specimens caused by the rovings pulling out of the lower flange.

In the case of the CONV-EPXY-240, the failure in the overlap region can be explained by the fact that the overlap region is considered to be a weak point of the structure, in which stress concentration can happen due to the discontinuity of the reinforcement, causing a premature failure of the structural element.

Figure 4.20 shows the moment *vs.* curvature curves. The curvature was obtained using the strain values measured by the strain gauges on the bottom flange of the textile reinforcement and on the top flange of the beam.

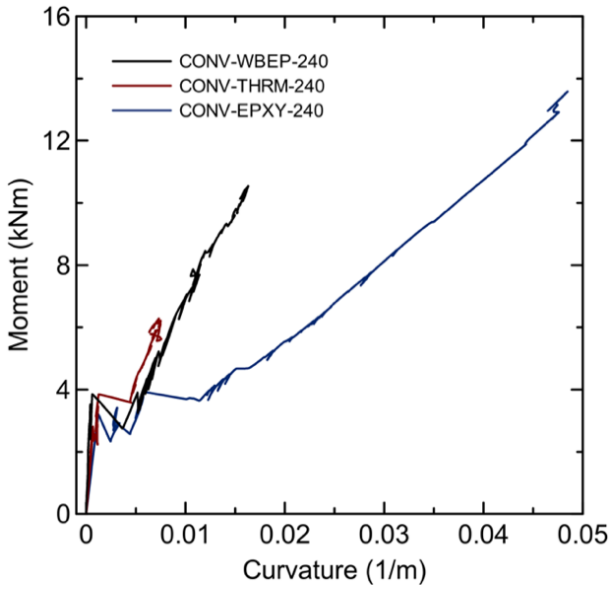


Figure 4.20 - Moment *vs.* curvature curves of the CONV-WBEP-240, CONV-THRM-240, and CONV-EPXY-240 carbon TRC beams.

The moment *vs.* curvature relations obtained show that all beams exhibited the expected behavior of TRC, which can be divided into three stages. Initially, all beams displayed similar behavior in Stage I, where a linear elastic response was observed, with the uncracked matrix governing the material's behavior at this phase. Once the tensile strength of the matrix was reached, a multiple-cracking stage occurred, with the CONV-EPXY-240 beam exhibiting a more prolonged tension stiffening phase. In the post-cracking stage, the CONV-EPXY-240 beam demonstrated the highest moment resistance, reaching a maximum value of 13.6 kNm, while the CONV-WBEP-240 and CONV-THRM-240 beams reached values of 10.5 and 6.28 kNm, respectively. The curvature at failure also varied significantly among the beams, with the CONV-EPXY-240 reaching the highest curvature (0.0485 m^{-1}). Although the slope of the CONV-WBEP-240 curve in this section was similar to that of CONV-THRM-240, the CONV-WBEP-240 beam exhibited a curvature of 0.0164 m^{-1}, which is significantly higher than that achieved by CONV-THRM-240 (0.00730 m^{-1}). The lower curvature of the CONV-THRM-240 beam may be attributed to premature failure caused by textile pull-out at the web-flange junction.

4.3.2. Influence of the UHPC matrix

Figure 4.21a exhibits the load *vs.* deflection at mid-span curves for all beams with the conventional and ultra-high performance concrete matrices and the solvent-based epoxy-coated textile (CONV-EPXY-240, UHPC-EPXY-240, CONV-EPXY-300, and UHPC-EPXY-300). Figure 4.21b shows the detail of the curves at lower deflections. The main results of the four-point bending tests on these beams can be seen in Table 4.11.

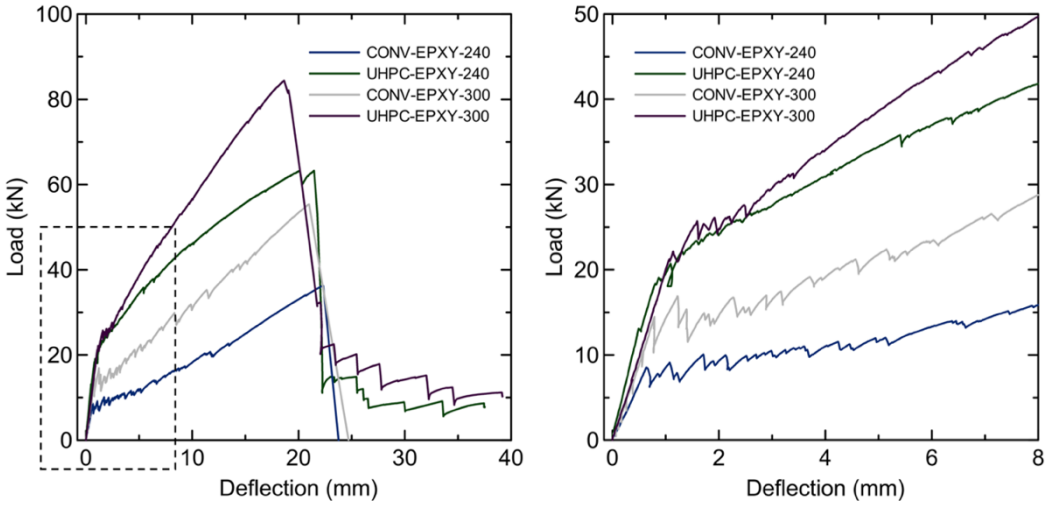


Figure 4.21 - Load *vs.* deflection curves for the CONV-EPXY-240, UHPC-EPXY-240, CONV-EPXY-300, and UHPC-EPXY-300 carbon TRC beams: (a) overview and (b) detail for low deflections.

Table 4.11 - Main results obtained from the four-point bending tests on the carbon TRC I-section beams: CONV-EPXY-240, UHPC-EPXY-240, CONV-EPXY-300, and UHPC-EPXY-240.

	CONV-EPXY-240	UHPC-EPXY-240	CONV-EPXY-300	UHPC-EPXY-300
F_{max} (kN)	36.2	63.8	55.3	84.4
$\delta_{F,max}$ (mm)	22.3	20.1	21.0	18.6
M_{max} (kNm)	13.6	23.7	20.8	31.6
$\Phi_{M,max}$ (1/m)	0.0485	0.0421	-(a)	-(a)
F_{cr} (kN)	8.55	20.7	1.30	22.2
$\delta_{F,cr}$ (mm)	0.637	1.11	0.0183	1.14
Failure mode	Shear	Shear and flexure	Shear and flexure	Flexure

F_{max} – maximum load at mid-span.
δ_{Fmax} – maximum deflection at mid-span at the maximum load.
M_{max} – maximum moment.
$\Phi_{M,max}$ – curvature at maximum bending moment.
F_{cr} – first crack load.
δ_{Fcr} – deflection at the first crack load.
(a) – not obtained due to loss of data before the ultimate load.

Regarding the influence of the UHPC matrix in the beams with the 240 mm section height, it can be observed in Figure 4.21b that the UHPC-EPXY-240 beam exhibited a significantly higher initial stiffness compared to the CONV-EPXY-240, evidenced by the steeper slope of the curve in the linear elastic stage (Stage I). The first crack load was also considerably improved by the UHPC matrix, presenting a difference of 142% in comparison to the conventional matrix. The increased stiffness and first crack load can be attributed to the dense microstructure and

increased strength of the UHPC matrix, combined with the crack bridging effect provided by the steel fibers, which delay the onset of cracking and improve stress distribution.

Furthermore, the UHPC-EPXY-240 beam presented a significantly higher ultimate load capacity than the CONV-EPXY-240, reaching a maximum load of 63.8 kN, a difference of 76.2% to that achieved by the beam with the conventional matrix (36.2 kN). This indicates that the steel fiber reinforced UHPC matrix allowed for greater load distribution to the carbon textile reinforcement, resulting in improved structural performance. The steel fibers played a key role in controlling the crack propagation, thereby increasing the toughness and load capacity of the beam.

As shown in Figure 4.21a, after reaching the ultimate load, both beams experienced a reduction in the load-bearing capacity post-peak. Nevertheless, the UHPC-EPXY-240 beam showed a more gradual decline, presenting a residual load-bearing capacity and indicating a more ductile failure mode compared with the abrupt failure observed in the CONV-EPXY-240 beam.

Similar trends were observed when comparing the UHPC-EPXY-300 and CONV-EPXY-300 beams in terms of the overall behavior. The UHPC-EPXY-300 beam also exhibited higher initial stiffness, first crack load and ultimate load compared to CONV-EPXY-300. In addition, the beam with the UHPC matrix exhibited more ductile failure, presenting a softening stage and residual load-bearing capacity after rupture.

From the load *vs.* deflection curve (Figure 4.21b), it was possible to note that the first crack stress of the CONV-EPXY-300 beam was considerably lower compared to the ones observed in the others beams with the conventional matrix, as shown in Table 4.11, and that the linear elastic stage practically does not exist. Considering that this stage depends mainly on the properties of the uncracked matrix, it is possible that, although it was not observed, this beam had already cracked at some point before the start of the test, which explains the reduced first crack load of the beam.

Evidently, the I-section beams with 300 mm height presented greater load-bearing capacities than their 240 mm counterparts. This result was expected due to the increased cross-sectional area and moment of inertia. It is interesting to note that while the increase in height led to an increase in the maximum load of 32.3%

for the UHPC-EPXY-300, this improvement was 52.8% for the CONV-EPXY-300. This indicates that the section height played a more considerable role in the case of the beams with the fine-grained concrete matrix. This difference in the impact of increasing the beam height between conventional and UHPC matrices can be attributed to the stress distribution within each material. In conventional concrete, stress distribution tends to be less uniform, especially in smaller sections, resulting in stress concentrations at weaker points. By increasing the beam height, the stress distribution becomes more homogeneous, allowing the cross-section to withstand higher loads more efficiently. Conversely, UHPC, due to its inherent material properties and the presence of fibers, exhibits a more uniform stress distribution even in the case of a reduced section.

For the maximum deflection allowed by the Brazilian Standard NBR 6118 [6] in the SLS (7.2 mm), the applied loads on the CONV-EPXY-240 and UHPC-EPXY-240 beams were 14.7 and 39.8 kN, respectively. In the case of the CONV-EPXY-300 and UHPC-EPXY-300, the loads were 26.0 and 47.1 kN, respectively. These results emphasize the significant enhancement in the load-bearing capacity afforded by the use of the UHPC matrix compared to the conventional fine-grained concrete matrix at the serviceability limit state. A 170.7% increase in the load capacity was observed in the UHPC-EPXY-240 in comparison to its conventional counterpart at the same deflection limit. Similarly, the UHPC-EPXY-300 beam exhibited an 81.2% increase in load capacity compared to the CONV-EPXY-300. Moreover, the increase in section height from 240 to 300 mm resulted in a 76.8% increase in load capacity for the CONV beams and an 18.3% increase for the UHPC beams at the SLS deflection limit. This reinforces the observation that while increased section height benefits both concrete types, the effect was more pronounced in beams with the conventional matrix.

Figure 4.22 shows the cracking patterns of the CONV-EPXY-240 and UHPC-EPXY-240 beams at the maximum deflection allowed by the SLS (7.2 mm) and at the deflection at the maximum load obtained with a DIC analysis. Table 4.12 lists the mean cracking spacing and widths at these deflections. As a problem with the DIC data acquisition of the CONV-EPXY-300 beam occurred, only the cracking behavior of the 240 mm high beams is presented and discussed.

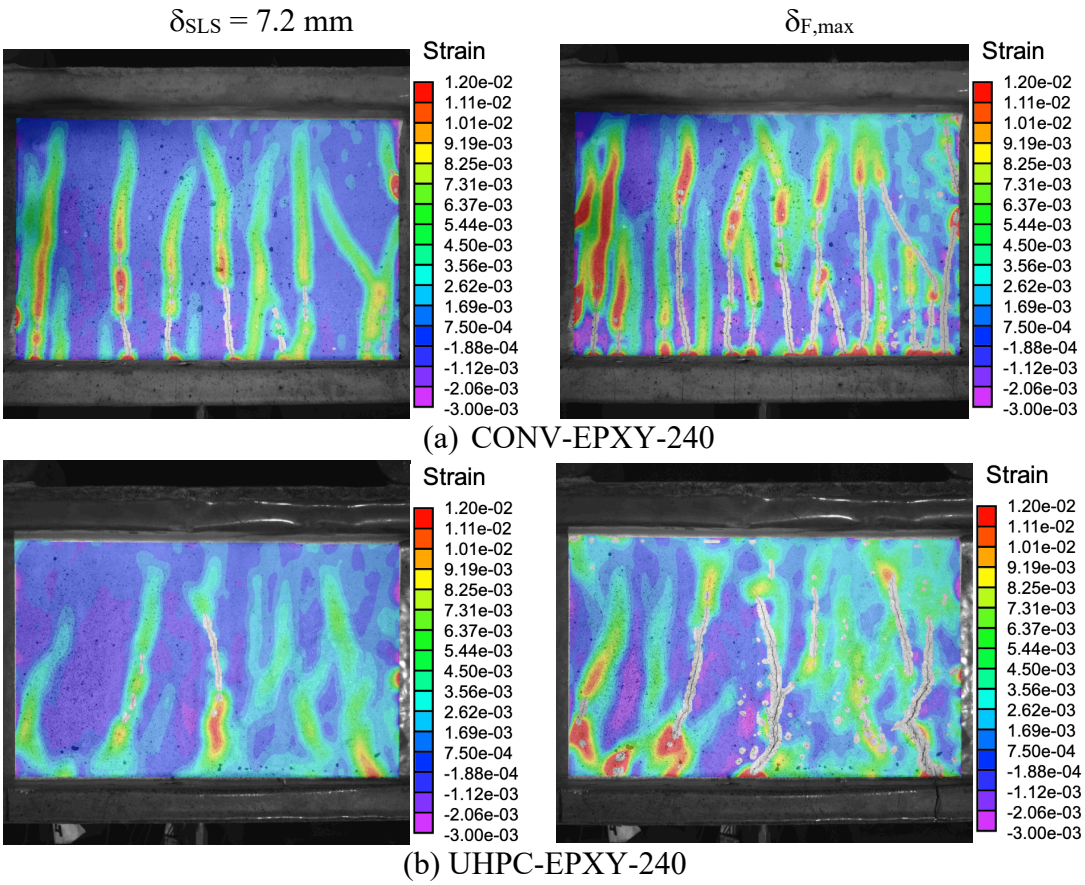


Figure 4.22 - Crack pattern of the (a) CONV-EPXY-240 and (b) UHPC-EPXY-240 beams at the SLS and at the maximum load.

Table 4.12 - DIC analysis results at different deflection levels for the CONV-EPXY-240 and UHPC-EPXY-240 carbon TRC I-section beams.

	CONV-EPXY-240	UHPC-EPXY-240
$s_{m,SLS}$ (mm)	16.4	61.3
$s_{m,max}$ (mm)	16.5	28.7
$w_{m,SLS}$ (μm)	47.2	18.6
$w_{m,max}$ (μm)	110.3	162.2

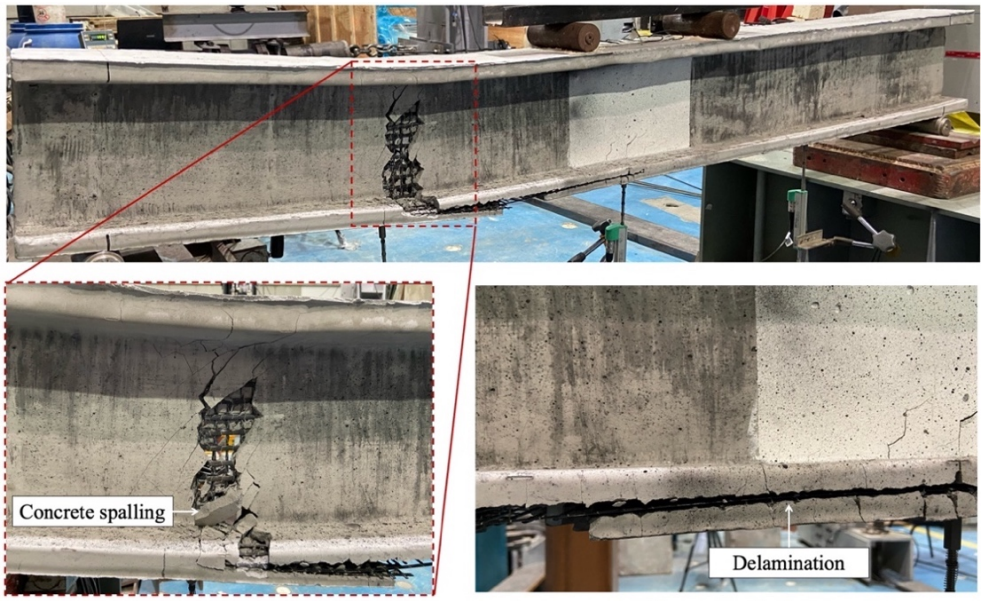
$s_{m,SLS}$ – average cracking spacing on Serviceability Limit State (SLS).
$s_{m,max}$ – average distance between cracks at the maximum load.
w_{SLS} – average crack width at the Serviceability Limit State (SLS).
$w_{m,max}$ – average crack width at the maximum load.

From Figure 4.22, it can be noted that at a 7.2 mm deflection, the beams with the UHPC matrix presented fewer macro cracks, but they were considerably smaller than the ones in the CONV-EPXY-240 beam, as reported in Table 4.12. The mean crack widths measured for the CONV-EPXY-240 and UHPC-EPXY-240 beams at this deflection were 47.2 and 18.6 mm, respectively. This represents a 60.5% reduction.

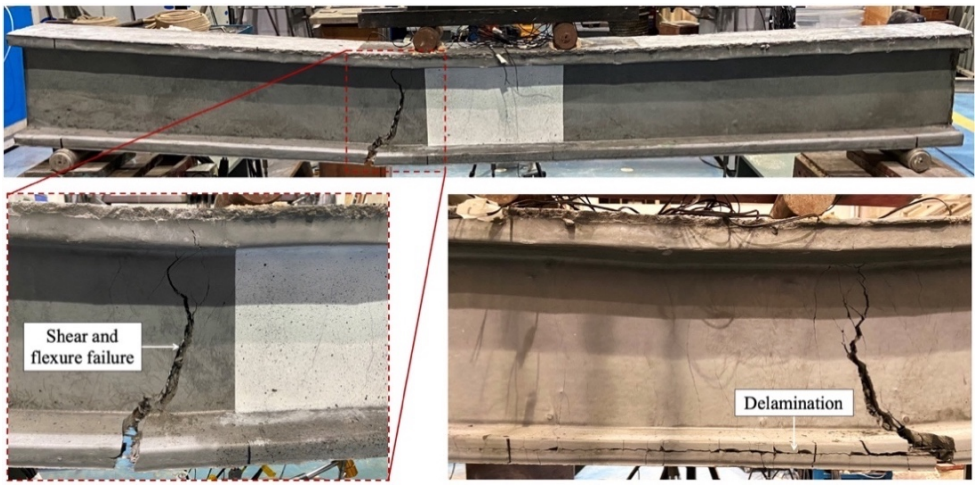
The finer cracking pattern observed, combined with the substantial difference in load capacity at the SLS deflection, highlights the potential of UHPC to provide superior structural performance and durability to TRC elements, particularly in applications where serviceability requirements are critical. This improved performance can lead to more efficient designs, possibly reducing material usage and extending the service life of structures, further contributing to the sustainability of textile reinforced concrete.

It is interesting to note that at the maximum load, the UHPC-EPXY-240 presented a significantly higher crack width than the CONV-EPXY-240 variation. This larger crack size at the ultimate load can be attributed to the localized stress concentrations and the reduced effectiveness of the steel fibers in preventing crack propagation as the beam reaches its ultimate load [137]. While UHPC initially resists cracking better due to its high strength and fiber reinforcement, its dense, relatively brittle nature and the limitations of fiber bridging under high deflections likely contribute to larger cracks at the ultimate load [138]. As the UHPC matrix approaches its ultimate capacity, the fiber-bridging mechanisms may become less effective due to fiber pull-out or rupture, leading to rapid crack propagation and widening [139].

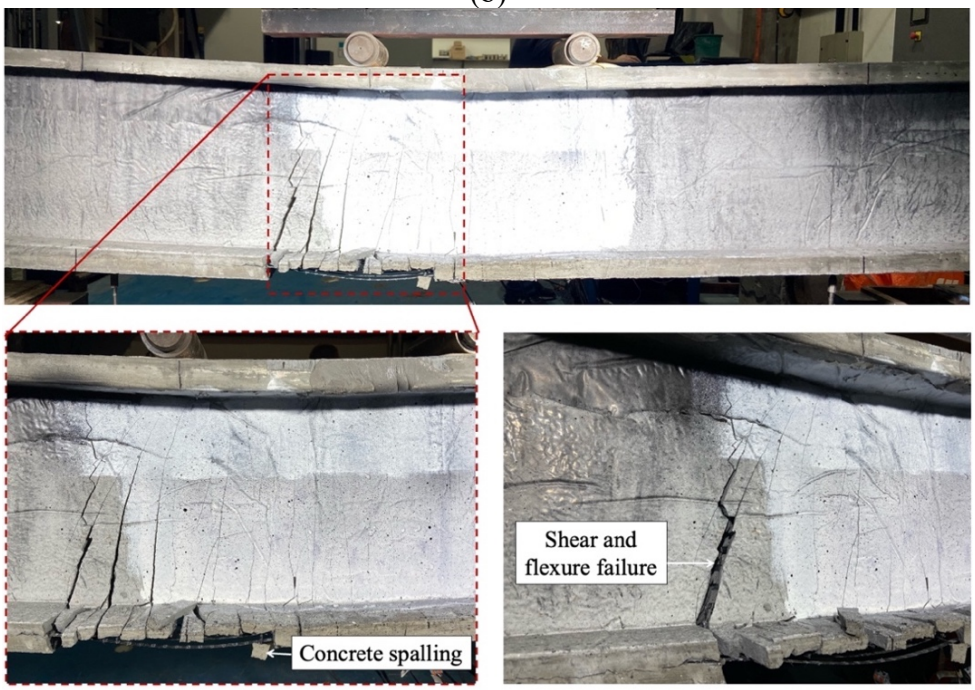
The failure modes of the CONV-EPXY-240, UHPC-EPXY-240, CONV-EPXY-300, and UHPC-EPXY-300 beams can be observed in Figure 4.23.



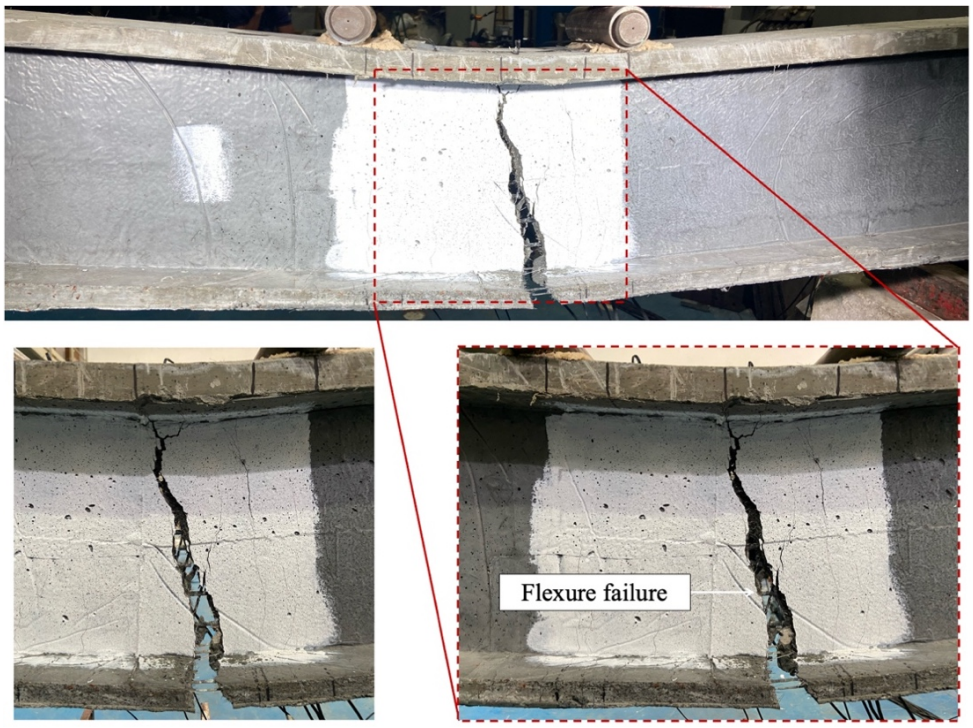
(a)


Shear and
flexure failure
Delamination

(b)


Concrete spalling
Shear and
flexure failure

(c)



(d)

Figure 4.23 - Failure modes of the (a) CONV-EPXY-240, (b) UHPC-EPXY-240, (c) CONV-EPXY-300, and (d) UHPC-EPXY-300 carbon TRC I-section beams.

The failure mode of the UHPC-EPXY-240 beam differed from that presented by the one with the conventional matrix. Unlike the CONV-EPXY-240 beam, which failed by shear in the overlap region, the UHPC-EPXY-240 beam failed due to a combination of shear and flexure stresses. As seen in Figure 4.23b, the crack that led to the rupture of this beam was formed closer to the constant moment region in the direction of one of the load application points, where both shear and bending stresses are maximized. This beam demonstrated a more ductile failure mode and did not display concrete spalling upon failure, despite exhibiting delamination on the bottom flange. The difference in the failure modes can be attributed to the presence of short steel fibers in the UHPC matrix. The dispersed fibers caused the stress transfer between the web and flange to happen more efficiently than in the CONV-EPXY-240, also helping avoid concrete spalling. Nevertheless, their addition alone was not able to substantially increase the shear bearing capacity of the beam, resulting in the observed failure mode previously mentioned.

As observed in Figure 4.23c and d, the failure modes of the beams with 300 mm height were different from those observed in their counterparts with 240 mm height. While the CONV-EPXY-300 beam presented a failure by shear and flexure,

the beam with the UHPC matrix exhibited a flexural failure. The shear strength of a structural element is directly related to the shear span-to-depth (a/d) ratio [140]. In the study conducted by Preinstorfer *et al.* [124], it was observed that with the decrease in the a/d ratio, the shear resistance increased. Therefore, the increase in the beam height to 300 mm resulted in a 20% reduction in the a/d ratio, which enhanced the shear capacity and altered the failure mode. The difference in the failure mode observed between the beams with 300 mm section height can be attributed to the presence of short, dispersed fibers in the UHPC matrix. Previous studies [141,142] have reported that the shear strength of structures subjected to bending stresses can be increased by incorporating dispersed fibers into the concrete matrix. Thus, the steel fibers present in the UHPC matrix acted efficiently in the UHPC-EPXY-300 beam, enhancing the shear load-bearing capacity and leading to a flexural failure.

Figure 4.24 presents the moment *vs.* curvature curves obtained for the beams with the EPXY-coated textile reinforcement. The curvature was obtained from the strain values recorded by the strain gauges glued to the fabric reinforcement and concrete for the CONV-EPXY-240 and UHPC-EPXY-240 beams and those placed on the top and bottom flanges of the CONV-EPXY-300 and UHPC-EPXY-300 beams.

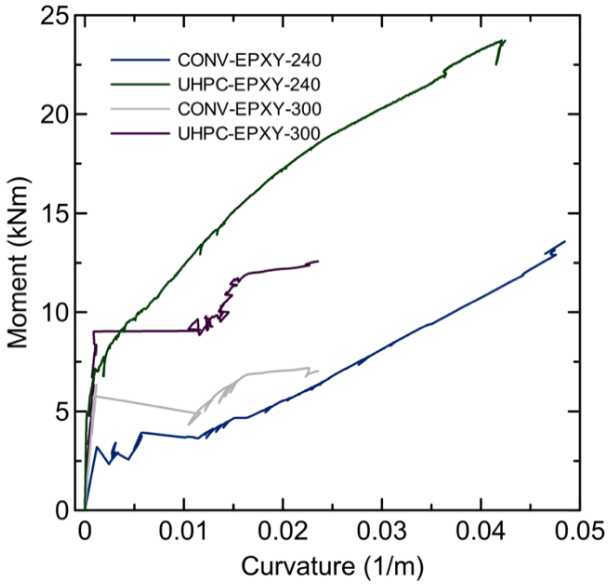


Figure 4.24 - Moment *vs.* curvature curves of the CONV-EPXY-240, UHPC-EPXY-240, CONV-EPXY-300 and UHPC-EPXY-300 carbon TRC beams.

The influence of the ultra-high performance matrix can be observed in the first two stages. In the linear elastic stage, the increase in the stiffness and resistance to the formation of the first crack are related to the mechanical properties of the matrix. In the second stage, there is a gradual transition to the multiple-cracking phase, characterized by stress redistribution in the material. This process shows a delay similar to that described by Goliath *et al.* [126], which can be explained by the bridging effect provided by the steel fibers. This mechanism limits the crack opening and contributes to the post-cracking stiffness [77]. In the third stage, which is governed by the textile reinforcement, the moment-curvature curves exhibited a similar pattern but with an upward shift, reflecting the influence of the matrix properties. As a result, the failure curvature values remained similar. Due to instrumentation issues, it was not possible to obtain the full moment *vs.* curvature relations for the 300 mm-high beams, as shown in Figure 4.24.

5
Conclusion

5.1.
Conclusion

This study aimed to investigate the effect of different surface coatings (a water-based epoxy resin, a thermoplastic resin, and a solvent-based epoxy resin) and the influence of an ultra-high performance concrete matrix on the mechanical and structural performance of carbon textile reinforced concrete.

The effect of different coatings on the hydrophobicity of the carbon yarns was evaluated using water contact angle tests. A water-based epoxy (WBEP), thermoplastic resin (THRM), and commercial solvent-based epoxy (EPXY) coating were considered, as well as various curing times of the WBEP (1 hour, 4 hours, 24 hours, and 7 days). The results indicate that:

- The curing time significantly impacts the hydrophobicity of carbon yarns coated with WBEP, shifting from hydrophilic to hydrophobic as curing progressed, due to water evaporation and coating densification. With higher curing times, WBEP coatings exhibited greater hydrophobicity compared to EPXY and THRM, the latter showing a more hydrophilic nature.
- Although it was expected that the WBEP presented a more hydrophilic nature than the EPXY, the surface roughness contributed to the higher observed contact angles, as confirmed by the scanning electron microscopy analysis of the carbon yarns.

The textiles were evaluated using three-point bending tests to study the influence of different coatings on the flexural stiffness of carbon fabrics. The water-based epoxy (WBEP) and thermoplastic resin (THRM) coatings were compared to two commercial coatings, a solvent-based epoxy (EPXY) and a styrene-butadiene rubber (SBR). The following conclusions can be drawn from the results:

- Although the THRM fabrics presented the highest bending stiffness among all the specimens, the properties of the thermoplastic resin still allow for

design flexibility upon the application of thermal energy, not limiting the versatility this type of coating aims to offer.

- The WBEP coating resulted in stiffer textiles in comparison to EPXY and SBR. However, for its intended use as a suitable eco-friendly alternative to solvent-based epoxy, this may not restrict its application.

The mechanical performance of the TRC composites was assessed through direct tensile tests. The study variables considered were the type of matrix (conventional fine-grained concrete or ultra-high performance concrete), the type of coating (water-based epoxy, thermoplastic resin, or solvent-based epoxy), and, for the case of the specimens with the WBEP coating, the curing time of the resin before casting (4 hours, 24 hours, and 7 days). Based on the results, the following conclusions can be drawn:

- All composites with coated textiles presented the typical strain-hardening behavior of TRC under tensile loading.
- The thermoplastic resin coating yielded a slightly better tensile strength and significantly higher strain capacity than the water-based epoxy (CONV-WBEP-07d) coating, which can be attributed to the higher level of coating of the THRM yarn. However, in terms of cracking pattern, the CONV-THRM series displayed inferior behavior, with a diffused cracking pattern and significant concrete spalling, potentially influenced by the differing yarn geometry. Despite that, the THRM coating demonstrates potential for applications requiring design flexibility. Yet, implementing effective methods for controlled fabric remodeling with THRM coatings is essential for wider adoption.
- The CONV-EPXY composites demonstrated the highest overall mechanical performance, exhibiting substantially higher tensile strength when calculated using the reinforcement area. This can be attributed to the improved impregnation achieved through industrial-scale coating and a stronger bond with the cementitious matrix, as evidenced by the finer and more numerous cracks observed in the DIC analysis.
- Despite the superior performance of the CONV-EPXY specimens, the CONV-WBEP-07d series exhibited promising results, particularly considering the manual application process of the coating. The potential for

improved impregnation through industrial-scale processes suggests that WBEP could achieve performance comparable to that of EPXY. Furthermore, WBEP offers sustainability advantages due to lower VOC emissions and may contribute to a better chemical bond, making it a viable alternative.

- WBEP curing time did not significantly affect the tensile strength but had a considerable influence on the cracking behavior and failure mode of the composites, as a result of the differing textile-matrix bond. Shorter curing times affected the mechanical behavior of the TRC composites in Stage II, leading to fewer, larger cracks, and textile pull-out. Composites with the textiles with longer cured coating exhibited a greater number of finer cracks and an overall better mechanical behavior. Thus, for applications that require high mechanical properties and superior cracking behavior, 7-day curing is optimal, ensuring a strong bond and efficient stress transfer. Nonetheless, in applications where design flexibility is required, shorter curing times might be a more suitable option.
- The UHPC matrix significantly contributed to the increase in the first crack stress of the composites, which can be attributed to the higher tensile strength of this concrete in relation to the fine-grained concrete. Moreover, the dispersed fibers in the UHPC matrix oriented in the direction of the load improved the tensile strength of the TRC composites.
- The UHPC-EPXY series exhibited a finer multiple-cracking pattern in relation to the CONV-EPXY specimens, especially at the end of the multiple-cracking stage. This can be attributed to the presence of steel fibers in the UHPC matrix, which bridged the cracks leading to better cracking behavior.
- UHPC with steel fibers significantly enhances the performance of TRC, improving the ultimate strength, cracking behavior, and durability compared to conventional matrices.

Finally, four-point bending tests were performed to investigate the structural behavior of carbon TRC I-section beams with the WBEP, THRM, and EPXY coatings, CONV and UHPC matrix, and 240 and 300 mm height. Considering the results, the following points can be concluded:

- The level of impregnation of the textiles and the bond with the cementitious matrix play a significant role in the performance of TRC at the structural level. The CONV-EPXY-240 beam demonstrated the highest load-bearing capacity, primarily due to its superior textile-matrix bond and impregnation. Conversely, the CONV-THRM-240 beam exhibited the lowest load capacity due to an inferior textile-matrix bond.
- Although the CONV-EPXY-240 beam achieved a higher ultimate load and presented a finer cracking pattern, CONV-WBEP-240 showed good overall mechanical behavior, and the crack widths remained within the limits specified by the Brazilian Standard. This indicates the suitability of this coating as a viable alternative to the EPXY coating, with the potential for further improvement through enhanced impregnation techniques.
- Web-flange connection, textile orientation, and overlaps are other factors that considerably influence the structural performance of TRC I-section beams, leading to premature failure by shear when inadequate, and with higher shear span-to-depth (a/d) ratios.
- The increase in the cross-section height of the I-section beams from 240 to 300 mm improved the structural performance, with CONV-EPXY-300 and UHPC-EPXY-300 exhibiting higher load-bearing capacities in both the Ultimate and Serviceability Limit States. Furthermore, the failure modes were improved; the CONV-EPXY-300 beam presented a combination of shear and flexure, whereas the UHPC-EPXY-300 beam failed only by flexure.
- The UHPC matrix significantly improved beam performance, exhibiting higher stiffness, crack resistance, and load capacity than conventional concrete. This can be attributed to the dense structure of UHPC and short steel fiber incorporation, which also resulted in more ductile failure modes, and led to the flexure failure in the case of the UHPC-EPXY-300.
- In terms of meeting the cracking, durability, safety, and usability requirements of the Serviceability Limit State (SLS), the UHPC matrix appears to be more suitable than the conventional matrix due to its finer crack behavior, higher load capacities, and failure mode not characterized by concrete spalling.

5.2. Suggestions for future works

Suggestions for future works include the following:

- As the possibility of casting structures or elements with complex shapes using the prepreg approach is promising, it is suggested to evaluate further techniques to enhance the mechanical behavior of composites with this new approach in mind.
- Evaluation of the interface of the composites in cases where the resin of the coated fabric has not achieved its full resistance, especially in the early hours of curing.
- Study methods to improve the bond of textiles in which the coating is not fully cured in order to provide composites with better mechanical performance when the prepreg approach is applied.
- Further evaluation of the influence of different curing times of the WBEP resin on the mechanical behavior of the carbon TRC composites. It is suggested to analyze various curing times to assess the optimal curing time for the prepreg approach.
- Analysis of the long-term behavior of the WBEP coating when using the prepreg approach.
- For the thermoplastic coating to be adopted as a viable alternative to SBR coatings, it is important to investigate easy and effective ways to remodel the fabrics because all yarns must be heated simultaneously in the area where reshaping is desired.
- Evaluate the effect of other types of thermoplastic resins on the mechanical and structural performance of carbon TRC.
- Further analysis of the failure mechanisms involved in the shear failure of carbon TRC beams.
- Investigation of different web-flange connections and their effects on the flexural behavior of carbon TRC I-section beams.
- Application of an analytical model to compare to the experimental results of the flexural tests on the beams.

6
References

[1] Shi C, Jiménez AF, Palomo A. New cements for the 21st century: The pursuit of an alternative to Portland cement. Cem Concr Res 2011;41:750–63. https://doi.org/10.1016/j.cemconres.2011.03.016.

[2] Aïtcin P-C. Cements of yesterday and today Concrete of tomorrow. Cem Concr Res 2000:1349–59.

[3] Mehta PK, Monteiro PJM. Concrete: Microstructure, properties and materials. 3rd edition. McGraw-Hill; 2006.

[4] Beer FP, Johnston Jr. ER, DeWolf TJ, Mazurek DF. Mechanics of Materials. 7th edition. New York: McGraw-Hill Education; 2015.

[5] Bertolini L, Elsener B, Pedeferri P, Polder RB. Corrosion of Steel in Concrete. Wiley; 2003. https://doi.org/10.1002/3527603379.

[6] Associação Brasileira de Normas Técnicas. ABNT NBR 6118 - Projeto de Estruturas de Concreto. 2023.

[7] Brameshuber W. Report 36: textile reinforced concrete-state-of-the-art report of RILEM TC 201-TRC. RILEM Publications 2006.

[8] Hegger J, Will N, Bruckermann O, Voss S. Load-bearing behaviour and simulation of textile reinforced concrete. Materials and Structures/Materiaux et Constructions 2006;39:765–76. https://doi.org/10.1617/s11527-005-9039-y.

[9] Naaman AE. Thin TRC Products: Status, Outlook, and Future Directions. Textile Fibre Composites in Civil Engineering, Elsevier Inc.; 2016, p. 413–39. https://doi.org/10.1016/B978-1-78242-446-8.00019-7.

[10] Hegger J, Voss S. Investigations on the bearing behaviour and application potential of textile reinforced concrete. Eng Struct 2008;30:2050–6. https://doi.org/10.1016/j.engstruct.2008.01.006.

[11] Morgan P. Carbon Fibers and Their Composites. CRC Press; 2005. https://doi.org/10.1201/9781420028744.

[12] Chand S. Review Carbon fibers for composites. J Mater Sci 2000:1303–13.

[13] Dvorkin D, Peled A. Effect of reinforcement with carbon fabrics impregnated with nanoparticles on the tensile behavior of cement-based composites. Cem Concr Res 2016;85:28–38. https://doi.org/10.1016/j.cemconres.2016.03.008.

[14] Halvaei M, Latifi M, Jamshidi M. Study of the microstructure and flexural behavior of cementitious composites reinforced by surface modified carbon textiles. Constr Build Mater 2018;158:243–56. https://doi.org/10.1016/j.conbuildmat.2017.10.044.

[15] Silva RM de C. Comportamento mecânico de concretos têxteis reforçados com tecido de carbono: aspectos materiais e estruturais. Dissertação de mestrado. Pontifícia Universidade Católica do Rio de Janeiro, PUC-Rio, 2018.

[16] Wu G, Kong Z, Chen J, Huo S, Liu G. Preparation and properties of waterborne polyurethane/epoxy resin composite coating from anionic terpene-based polyol dispersion. Prog Org Coat 2014;77:315–21. https://doi.org/10.1016/j.porgcoat.2013.10.005.

[17] Scheurer M, Kalthoff M, Matschei T, Raupach M, Gries T. Analysis of Curing and Mechanical Performance of Pre-Impregnated Carbon Fibers Cured within Concrete. Textiles 2022;2:657–72. https://doi.org/10.3390/textiles2040038.

[18] Heins K, Lesker S, Pütz J, Hüntemann M, Gries T. Effect of thermoplastic impregnation on the mechanical behaviour of textile reinforcement for concrete. SN Appl Sci 2023;5. https://doi.org/10.1007/s42452-023-05305-y.

[19] Callister Jr. WD, Rethwisch DG. Materials Science and Engineering: An Introduction. 10th edition. John Wiley & Sons; 2018.

[20] John SK, Nadir Y, Girija K, Giriprasad S. Tensile behaviour of glass fibre textile reinforced mortar with fine aggregate partially replaced by fly ash. Mater Today Proc, vol. 27, Elsevier Ltd; 2020, p. 144–9. https://doi.org/10.1016/j.matpr.2019.09.135.

[21] Estevan L, Varona FB, Baeza FJ, Torres B, Bru D. Textile Reinforced Mortars (TRM) tensile behavior after high temperature exposure. Constr Build Mater 2022;328. https://doi.org/10.1016/j.conbuildmat.2022.127116.

[22] Trochoutsou N, Di Benedetti M, Pilakoutas K, Guadagnini M. Mechanical Characterisation of Flax and Jute Textile-Reinforced Mortars. Constr Build Mater 2021;271. https://doi.org/10.1016/j.conbuildmat.2020.121564.

[23] Signorini C, Nobili A, Cedillo González EI, Siligardi C. Silica coating for interphase bond enhancement of carbon and AR-glass Textile Reinforced Mortar (TRM). Compos B Eng 2018;141:191–202. https://doi.org/10.1016/j.compositesb.2017.12.045.

[24] Messori M, Nobili A, Signorini C, Sola A. Mechanical performance of epoxy coated AR-glass fabric Textile Reinforced Mortar: Influence of coating thickness and formulation. Compos B Eng 2018;149:135–43. https://doi.org/10.1016/j.compositesb.2018.05.023.

[25] Deng M, Dong Z, Zhang C. Experimental investigation on tensile behavior of carbon textile reinforced mortar (TRM) added with short polyvinyl alcohol (PVA) fibers. Constr Build Mater 2020;235. https://doi.org/10.1016/j.conbuildmat.2019.117801.

[26] Trung Duc Pham L, Woo U, Choi KK, Choi HJ. Tensile characteristics of carbon textile-reinforced mortar incorporating short amorphous metallic and nylon fibers under designed environmental conditions. Constr Build Mater 2022;352. https://doi.org/10.1016/j.conbuildmat.2022.129059.

[27] Dong Z, Deng M, Zhang C, Zhang Y, Sun H. Tensile behavior of glass textile reinforced mortar (TRM) added with short PVA fibers. Constr Build Mater 2020;260. https://doi.org/10.1016/j.conbuildmat.2020.119897.

[28] Teixeira FP, de Souza FR, Garcia SLG, de Andrade Silva F. Strengthening and repair of RC beams using natural sisal Fabric-Reinforced Cementitious Matrix composite. Constr Build Mater 2024;447. https://doi.org/10.1016/j.conbuildmat.2024.138047.

[29] Feng R, Liu P, Zhang J, Wang F, Xu Y, Zhu JH. Bending behaviour of corroded RC continuous beams with C-FRCM strengthening system. Journal of Building Engineering 2022;60. https://doi.org/10.1016/j.jobe.2022.105229.

[30] Feng R, Liu Y, Zhu JH, Xing F. Flexural behaviour of C-FRCM strengthened corroded RC continuous beams. Compos Struct 2020;245. https://doi.org/10.1016/j.compstruct.2020.112200.

[31] Kadhim MMA, Jawdhari A, Adheem AH, Fam A. Analysis and design of two-way slabs strengthened in flexure with FRCM. Eng Struct 2022;256. https://doi.org/10.1016/j.engstruct.2022.113983.

[32] Toska K, Faleschini F, Zanini MA, Hofer L, Pellegrino C. Repair of severely damaged RC columns through FRCM composites. Constr Build Mater 2021;273. https://doi.org/10.1016/j.conbuildmat.2020.121739.

[33] Faleschini F, Zanini MA, Hofer L, Pellegrino C. Experimental behavior of reinforced concrete columns confined with carbon-FRCM composites. Constr Build Mater 2020;243. https://doi.org/10.1016/j.conbuildmat.2020.118296.

[34] Ombres L, Verre S. Structural behaviour of fabric reinforced cementitious matrix (FRCM) strengthened concrete columns under eccentric loading. Compos B Eng 2015;75:235–49. https://doi.org/10.1016/j.compositesb.2015.01.042.

[35] Focacci F, D'Antino T, Carloni C. Tensile Testing of FRCM Coupons for Material Characterization: Discussion of Critical Aspects. Journal of Composites for Construction 2022;26. https://doi.org/10.1061/(ASCE)CC.1943-5614.0001223.

[36] Homoro O, Michel M, Baranger TN. Dry mineral pre-impregnation for enhancing the properties of glass FRCM composites. Constr Build Mater 2020;263. https://doi.org/10.1016/j.conbuildmat.2020.120597.

[37] Scheerer S, Schladitz F, Curbach M. TEXTILE REINFORCED CONCRETE-FROM THE IDEA TO A HIGH PERFORMANCE MATERIAL. 2015.

[38] Peled A, Bentur A, Yankelevsky D. Woven Fabric Reinforcement of Cement Matrix. Advanced Cement Based Materials 1994;1:216–23.

[39] Bentur A, Peled A, Yankelevsky D. Enhanced bonding of low modulus polymer fibers-cement matrix by means of crimped geometry. Cem Concr Res 1997;27:1099–111. https://doi.org/10.1016/S0008-8846(97)00088-4.

[40] Ohno S, Hannant DJ. Modeling the Stress-Strain Response of Continuous Fber Reinforced Cement Composites. ACI Mater J 1994;91:306–12. https://doi.org/10.14359/4293.

[41] Naaman AE. TEXTILE REINFORCED CEMENT COMPOSITES: COMPETITIVE STATUS AND RESEARCH DIRECTIONS. vol. I. 2010.

[42] RILEM. 201-TRC: Textile reinforced concrete n.d.

[43] American Concrete Institute (ACI). 549 - Thin Reinforced Cementitious Products and Ferrocement. Https://WwwConcreteOrg/Committees/Directoryofcommittees/AcommittehomeAspx?Committee_code=C0054900 n.d.

[44] Alexander AE, Shashikala AP. Sustainability of Construction with Textile Reinforced Concrete- A State of the Art. IOP Conf Ser Mater Sci Eng, vol. 936, IOP Publishing Ltd; 2020. https://doi.org/10.1088/1757-899X/936/1/012006.

[45] Malhotra VM. Role of supplementary cementing materials in reducing greenhouse gas emissions. Concrete technology for a sustainable development in the 21st century, London: E & FN Spon; 2000.

[46] Scholzen A, Chudoba R, Hegger J. Thin-walled shell structures made of textile-reinforced concrete: Part I: Structural design and construction. Structural Concrete 2015;16:106–14. https://doi.org/10.1002/suco.201300071.

[47] Chudoba R, Sharei E, Scholzen A. A strain-hardening microplane damage model for thin-walled textile-reinforced concrete shells, calibration procedure, and experimental validation. Compos Struct 2016;152:913–28. https://doi.org/10.1016/j.compstruct.2016.06.030.

[48] Hegger J, Voss S. Investigations on the bearing behaviour and application potential of textile reinforced concrete. Eng Struct 2008;30:2050–6. https://doi.org/10.1016/j.engstruct.2008.01.006.

[49] Kulas C, Goralski C. Die weltweit längste Textilbetonbrücke. Beton- Und Stahlbetonbau 2014;109:812–7. https://doi.org/10.1002/best.201400066.

[50] Inauguration of the world's first building made of carbon concrete CUBE. Https://Tu-Dresden.de/Bu/Der-Bereich/News/Feierliche-Einweihung-Des-Weltweit-Ersten-Gebaeudes-Aus-Carbonbeton-Cube?Set_language=en 2022.

[51] HENN. CUBE. Https://WwwHennCom/En/Project/Cube n.d.

[52] Chudoba R, Van Der Woerd J, Schmerl M, Hegger J. ORICRETE: Modeling support for design and manufacturing of folded concrete structures. Advances in Engineering Software 2014;72:119–27. https://doi.org/10.1016/j.advengsoft.2013.05.004.

[53] Scheerer S, Chudoba R, Garibaldi MP, Curbach M. Shells made of textile reinforced concrete -applications in Germany. Journal of the International Association for Shell and Spatial Structures 2017;58:79–93. https://doi.org/10.20898/j.iass.2017.191.846.

[54] Kim HY, Koh KT, You YJ, Ryu GS, Seo DW, Jin SS, et al. Load-deflection behaviour of concrete slab-type elements casted on stay-in-place TRC formwork. Compos Struct 2020;244. https://doi.org/10.1016/j.compstruct.2020.112310.

[55] Koutas LN, Asce AM, Bournas DA. Flexural Strengthening of Two-Way RC Slabs with Textile-Reinforced Mortar: Experimental Investigation and Design Equations 2017. https://doi.org/10.1061/(ASCE)CC.1943-5614.

[56] Silva RM de C. Textile reinforced concrete with polymer-and mineral-impregnated carbon fabrics: from a material characterization to a structural application. Tese de doutorado. Pontifícia Universidade Católica do Rio de Janeiro, PUC-Rio, 2023.

[57] Hentschel M, Schumann A, Ulrich H, Jentzsch S. Sanierung der Hyparschale Magdeburg. Bautechnik 2019;96:25–30. https://doi.org/10.1002/bate.201800087.

[58] Steinbock O, Pelke E, Ost O. Carbonbeton – Eine neue Verstärkungsmethode für Massivbrücken. Beton- Und Stahlbetonbau 2021;116:101–8. https://doi.org/10.1002/best.202000094.

[59] S&P. Reforço de Vigas e Pilares - Estádio do Maracanã - Rio de Janeiro, Brasil. Https://WwwSp-ReinforcementPt/Pt-PT/Projectos/Reforco-de-Vigas-e-Pilares-Estadio-Do-Maracana-Rio-de-Janeiro-Brasil n.d.

[60] Clyne TW, Hull D. An Introduction to Composite Materials. Cambridge University Press; 2019. https://doi.org/10.1017/9781139050586.

[61] Peled A, Bentur A, Mobasher B. Textile Reinforced Concrete. CRC Press Taylor & Francis Group; 2017.

[62] Koutas LN, Tetta Z, Bournas DA, Triantafillou TC. Strengthening of Concrete Structures with Textile Reinforced Mortars: State-of-the-Art Review. Journal of Composites for Construction 2019;23. https://doi.org/10.1061/(asce)cc.1943-5614.0000882.

[63] Tlaiji T, Vu XH, Michel M, Ferrier E, Larbi AS. Physical, chemical and thermomechanical characterisation of glass textile-reinforced concretes

(TRC): Effect of elevated temperature and of cementitious matrix nature on properties of TRC. Mater Today Commun 2020;25. https://doi.org/10.1016/j.mtcomm.2020.101580.

[64] Strauss Rambo DA, De Andrade Silva F, Toledo Filho RD, Ukrainczyk N, Koenders E. Tensile strength of a calcium-aluminate cementitious composite reinforced with basalt textile in a high-temperature environment. Cem Concr Compos 2016;70:183–93. https://doi.org/10.1016/j.cemconcomp.2016.04.006.

[65] Rambo DAS, de Andrade Silva F, Toledo Filho RD, da Fonseca Martins Gomes O. Effect of elevated temperatures on the mechanical behavior of basalt textile reinforced refractory concrete. Mater Des 2015;65:24–33. https://doi.org/10.1016/j.matdes.2014.08.060.

[66] Wei J, Meyer C. Degradation rate of natural fiber in cement composites exposed to various accelerated aging environment conditions. Corros Sci 2014;88:118–32. https://doi.org/10.1016/j.corsci.2014.07.029.

[67] Toledo Filho RD, Silva F de A, Fairbairn EMR, Filho J de AM. Durability of compression molded sisal fiber reinforced mortar laminates. Constr Build Mater 2009;23:2409–20. https://doi.org/10.1016/j.conbuildmat.2008.10.012.

[68] Filho JDAM, Silva FDA, Toledo Filho RD. Degradation kinetics and aging mechanisms on sisal fiber cement composite systems. Cem Concr Compos 2013;40:30–9. https://doi.org/10.1016/j.cemconcomp.2013.04.003.

[69] Paul S, Gettu R, Naidu Arnepalli D, Samanthula R. Experimental evaluation of the durability of glass Textile-Reinforced concrete. Constr Build Mater 2023;406. https://doi.org/10.1016/j.conbuildmat.2023.133390.

[70] Butler M, Mechtcherine V, Hempel S. Durability of textile reinforced concrete made with AR glass fibre: Effect of the matrix composition. Materials and Structures/Materiaux et Constructions 2010;43:1351–68. https://doi.org/10.1617/s11527-010-9586-8.

[71] Majstorović F, Sebera V, Mrak M, Dolenec S, Wolf M, Marrot L. Impact of metakaolin on mechanical performance of flax textile-reinforced cement-based composites. Cem Concr Compos 2022;126. https://doi.org/10.1016/j.cemconcomp.2021.104367.

[72] Fidelis MEA, Toledo Filho RD, Silva F de A, Mechtcherine V, Butler M, Hempel S. The effect of accelerated aging on the interface of jute textile reinforced concrete. Cem Concr Compos 2016;74:7–15. https://doi.org/10.1016/j.cemconcomp.2016.09.002.

[73] Kong K, Mesticou Z, Michel M, Si Larbi A, Junes A. Comparative characterization of the durability behaviour of textile-reinforced concrete (TRC) under tension and bending. Compos Struct 2017;179:107–23. https://doi.org/10.1016/j.compstruct.2017.07.030.

[74] Silva FDA, Butler M, Hempel S, Toledo Filho RD, Mechtcherine V. Effects of elevated temperatures on the interface properties of carbon textile-reinforced concrete. Cem Concr Compos 2014;48:26–34. https://doi.org/10.1016/j.cemconcomp.2014.01.007.

[75] Bentur A, Mindess S. Fibre Reinforced Cementitious Composites. Taylor & Francis; 2007.

[76] Du Y, Zhang X, Liu L, Zhou F, Zhu D, Pan W. Flexural behaviour of carbon textile-reinforced concrete with prestress and steel fibres. Polymers (Basel) 2018;10. https://doi.org/10.3390/POLYM10010098.

[77] Barhum R, Mechtcherine V. Effect of short, dispersed glass and carbon fibres on the behaviour of textile-reinforced concrete under tensile loading. Eng Fract Mech 2012;92:56–71. https://doi.org/10.1016/j.engfracmech.2012.06.001.

[78] Pham HH, Dinh NH, Kim SH, Park SH, Choi KK. Tensile behavioral characteristics of lightweight carbon textile-reinforced cementitious composites. Journal of Building Engineering 2022;57. https://doi.org/10.1016/j.jobe.2022.104848.

[79] Mobasher B. Mechanics of Fiber and Textile Reinforced Cement Composites. CRC Press Taylor & Francis Group; 2012.

[80] Du Y, Zhang X, Zhou F, Zhu D, Zhang M, Pan W. Flexural behavior of basalt textile-reinforced concrete. Constr Build Mater 2018;183:7–21. https://doi.org/10.1016/j.conbuildmat.2018.06.165.

[81] Zhu D, Liu S, Yao Y, Li G, Du Y, Shi C. Effects of short fiber and pre-tension on the tensile behavior of basalt textile reinforced concrete. Cem Concr Compos 2019;96:33–45. https://doi.org/10.1016/j.cemconcomp.2018.11.015.

[82] Dinh NH, Pham HH, Kim SH, Choi KK. Experimental investigation on flexural and direct shear behaviors of specimens made of lightweight carbon textile-reinforced cementitious composites. Structural Concrete 2023;24:5027–54. https://doi.org/10.1002/suco.202200509.

[83] Mechtcherine V. Novel cement-based composites for the strengthening and repair of concrete structures. Constr Build Mater 2013;41:365–73. https://doi.org/10.1016/j.conbuildmat.2012.11.117.

[84] Li VC. On Engineered Cementitious Composites (ECC) A Review of the Material and Its Applications. vol. 1. 2003.

[85] Gong T, Ahmed AH, Curosu I, Mechtcherine V. Tensile behavior of hybrid fiber reinforced composites made of strain-hardening cement-based composites (SHCC) and carbon textile. Constr Build Mater 2020;262. https://doi.org/10.1016/j.conbuildmat.2020.120913.

[86] Li B, Xiong H, Jiang J, Dou X. Tensile behavior of basalt textile grid reinforced Engineering Cementitious Composite. Compos B Eng 2019;156:185–200. https://doi.org/10.1016/j.compositesb.2018.08.059.

[87] Gong T. On the synergetic action between strain-hardening cement based composites (SHCC) and carbon textile reinforcement under tensile loading, International Association for Fracture Mechanics of Concrete and Concrete Structures; 2019. https://doi.org/10.21012/fc10.235471.

[88] Goliath KB. Flexural Behavior of I-Section Textile Reinforced Concrete Beams. Thesis. Pontifícia Universidade Católica do Rio de Janeiro, PUC-Rio, 2022.

[89] American Society for Testing and Materials (ASTM International). C1856/C1856M - 17: Standard Practice for Fabricating and Testing Specimens of Ultra-High Performance Concrete. 2017.

[90] Hung C-C, El-Tawil S, Chao S-H. A Review of Developments and Challenges for UHPC in Structural Engineering: Behavior, Analysis, and Design. Journal of Structural Engineering 2021;147. https://doi.org/10.1061/(asce)st.1943-541x.0003073.

[91] Buttignol TET, Sousa JLAO, Bittencourt TN. Ultra High-Performance Fiber-Reinforced Concrete (UHPFRC): a review of material properties and design procedures. Revista IBRACON de Estruturas e Materiais 2017;10:957–71. https://doi.org/10.1590/s1983-41952017000400011.

[92] Bajaber MA, Hakeem IY. UHPC evolution, development, and utilization in construction: A review. Journal of Materials Research and Technology 2021;10:1058–74. https://doi.org/10.1016/j.jmrt.2020.12.051.

[93] Yao Y, Silva FA, Butler M, Mechtcherine V, Mobasher B. Tensile and Flexural Behavior of Ultra-High Performance Concrete (UHPC) under Impact Loading. Int J Impact Eng 2021;153. https://doi.org/10.1016/j.ijimpeng.2021.103866.

[94] Mészöly T, Ofner S, Randl N. Effect of Combining Fiber and Textile Reinforcement on the Flexural Behavior of UHPC Plates. Advances in Materials Science and Engineering 2020;2020. https://doi.org/10.1155/2020/9891619.

[95] Rossi E, Randl N, Harsányi P, Mészöly T. Overlapped joints in Textile Reinforced Concrete with UHPC matrix: An experimental investigation. Materials and Structures/Materiaux et Constructions 2021;54. https://doi.org/10.1617/s11527-021-01739-1.

[96] Yao Y, Sun Y, Zhai M, Chen C, Lu C, Wang J. Tensile behavior of textile reinforced ultra-high performance concrete. Constr Build Mater 2024;411. https://doi.org/10.1016/j.conbuildmat.2023.134172.

[97] Triantafillou TC. Textile Fibre Composites in Civil Engineering. Woodhead Publishing; 2016.

[98] Peled A, Bentur A. Fabric structure and its reinforcing efficiency in textile reinforced cement composites. Compos Part A Appl Sci Manuf 2003;34:107–18. https://doi.org/10.1016/S1359-835X(03)00003-4.

[99] Peled A, Bentur A. Geometrical characteristics and efficiency of textile fabrics for reinforcing cement composites. Cem Concr Res 2000;30:781–90. https://doi.org/10.1016/S0008-8846(00)00239-8.

[100] El Kadi M, Kapsalis P, Van Hemelrijck D, Wastiels J, Tysmans T. Influence of loading orientation and knitted versus woven transversal connections in 3D textile reinforced cement (TRC) composites. Applied Sciences (Switzerland) 2020;10. https://doi.org/10.3390/app10134517.

[101] Armakan DM, Roye A. A study on the compression behavior of spacer fabrics designed for concrete applications. Fibers and Polymers 2009;10:116–23. https://doi.org/10.1007/s12221-009-0116-7.

[102] Donnini J, Corinaldesi V, Nanni A. Mechanical properties of FRCM using carbon fabrics with different coating treatments. Compos B Eng 2016;88:220–8. https://doi.org/10.1016/j.compositesb.2015.11.012.

[103] Silva RM de C, Silva F de A. Carbon textile reinforced concrete: materials and structural analysis. Materials and Structures/Materiaux et Constructions 2020;53. https://doi.org/10.1617/s11527-020-1448-4.

[104] Goliath KB, Cardoso DCT, Silva F de A. Influence of mechanical characterization technique on Carbon-TRC constitutive relations. Journal of Building Engineering 2023;67. https://doi.org/10.1016/j.jobe.2023.106058.

[105] Xu S, Krüger M, Reinhardt H-W, Ožbolt J. Bond Characteristics of Carbon, Alkali Resistant Glass, and Aramid Textiles in Mortar. Journal of Materials in Civil Engineering 2004. https://doi.org/10.1061/ASCE0899-1561200416:4356.

[106] Silva F de A, Chawla N, Filho RD de T. Tensile behavior of high performance natural (sisal) fibers. Compos Sci Technol 2008;68:3438–43. https://doi.org/10.1016/j.compscitech.2008.10.001.

[107] Alan Strauss Rambo D, Umbinger de Oliveira C, Pícolo Salvador R, Dias Toledo Filho R, da Fonseca Martins Gomes O, de Andrade Silva F, et al. Sisal textile reinforced concrete: Improving tensile strength and bonding through peeling and nano-silica treatment. Constr Build Mater 2021;301. https://doi.org/10.1016/j.conbuildmat.2021.124300.

[108] Teixeira FP, de Andrade Silva F. On the use of natural curauá reinforced cement based composites for structural applications. Cem Concr Compos 2020;114. https://doi.org/10.1016/j.cemconcomp.2020.103775.

[109] De Souza LO, De Souza LMS, De Andrade Silva F. Mechanics of natural curauá textile-reinforced concrete. Magazine of Concrete Research 2021;73:135–46. https://doi.org/10.1680/jmacr.18.00473.

[110] Santos RF dos. Influência da estrutura de tecido plano de juta empregado como reforço em compósitos cimentícios. Dissertação de mestrado. Universidade Federal de Santa Catarina, UFSC, 2022.

[111] Monaco A, Baldassari M, D'Anna J, Cornetti P. Effectiveness of Flax-TRM composites under traction. Procedia Structural Integrity, vol. 44, Elsevier B.V.; 2023, p. 2278–85. https://doi.org/10.1016/j.prostr.2023.01.291.

[112] Homoro O, Amziane S, Canullo MC, Contamine R. Mechanical characterization of flax textile reinforced cement matrix: effect of matrix parameters and reinforcement amount. European Journal of Environmental and Civil Engineering 2023;27:4528–43. https://doi.org/10.1080/19648189.2023.2194356.

[113] Preinstorfer P, El Kadi M, Dittel G, Ghiassi B, Müller S, Mansur de Castro Silva R, et al. Article of RILEM TC 292-MCC: bond behaviour of textile-reinforced concrete—a review. Materials and Structures/Materiaux et Constructions 2024;57. https://doi.org/10.1617/s11527-024-02339-5.

[114] Schleser M, Walk-Lauffer B, Raupach M, Dilthey U. Application of Polymers to Textile-Reinforced Concrete. Journal of Materials in Civil Engineering 2006. https://doi.org/10.1061/ASCE0899-1561200618:5670.

[115] Valeri P, Fernàndez Ruiz M, Muttoni A. Tensile response of textile reinforced concrete. Constr Build Mater 2020;258. https://doi.org/10.1016/j.conbuildmat.2020.119517.

[116] Scheurer M, Friese D, Heins K, Hahn L, Mersch J, Cherif C, et al. Novel Textile Reinforcements for Advanced Concrete Production Methods, 2024, p. 778–85. https://doi.org/10.1007/978-3-031-70145-0_92.

[117] Silva RM de C, Zhao J, Liebscher M, Curosu I, Silva F de A, Mechtcherine V. Bond behavior of polymer- and mineral-impregnated carbon fiber yarns towards concrete matrices at elevated temperature levels. Cem Concr Compos 2022;133. https://doi.org/10.1016/j.cemconcomp.2022.104685.

[118] Bisby LA, Green MF, Kodur VKR. Response to fire of concrete structures that incorporate FRP. Progress in Structural Engineering and Materials 2005;7:136–49. https://doi.org/10.1002/pse.198.

[119] Hegger J, Will N, Bruckermann O, Voss S. Load–bearing behaviour and simulation of textile reinforced concrete. Mater Struct 2006;39:765–76. https://doi.org/10.1617/s11527-005-9039-y.

[120] Nadiv R, Peled A, Mechtcherine V, Hempel S, Schroefl C. Micro- and nanoparticle mineral coating for enhanced properties of carbon multifilament yarn cement-based composites. Compos B Eng 2017;111:179–89. https://doi.org/10.1016/j.compositesb.2016.12.005.

[121] Nahum L, Peled A, Gal E. The flexural performance of structural concrete beams reinforced with carbon textile fabrics. Compos Struct 2020;239. https://doi.org/10.1016/j.compstruct.2020.111917.

[122] Valeri P, Ruiz MF, Muttoni A. Modelling of Textile Reinforced Concrete in bending and shear with Elastic-Cracked Stress Fields. Eng Struct 2020;215. https://doi.org/10.1016/j.engstruct.2020.110664.

[123] Bielak J, Schmidt M, Hegger J, Jesse F. Structural behavior of large-scale I-beams with combined textile and CFRP reinforcement. Applied Sciences (Switzerland) 2020;10. https://doi.org/10.3390/app10134625.

[124] Preinstorfer P, Huber P, Huber T, Kromoser B, Kollegger J. Experimental investigation and analytical modelling of shear strength of thin walled textile-reinforced UHPC beams. Eng Struct 2021;231. https://doi.org/10.1016/j.engstruct.2020.111735.

[125] Kulas CH. Zum Tragverhalten getränkter textiler Bewehrungselemente für Betonbauteile. PhD thesis. RWTH Aachen, 2013.

[126] Goliath KB, Cardoso DCT, Silva F de A. Flexural behavior of carbon-textile-reinforced concrete I-section beams. Compos Struct 2021;260. https://doi.org/10.1016/j.compstruct.2021.113540.

[127] Santos VB dos. Experimental and numerical study of steel and ultra-high performance concrete composite beams under hogging moment. Tese de doutorado. Universidade Federal de São Carlos, n.d.

[128] American Society for Testing and Materials (ASTM International). ASTM C595: Standard specification for blended hydraulic cements. 2008.

[129] Associação Brasileira de Normas Técnicas. ABNT NBR 16697 - Cimento Portland - Requisitos. Rio de Janeiro: 2018.

[130] Associação Brasileira de Normas Técnicas. ABNT NBR 5738 - Concreto - Procedimento para moldagem e cura de corpos de prova. 2015.

[131] MC-Bauchemie. MC-DUR 1177 WV-A: Ficha técnica. Https://WwwMc-BauchemieComBr/Assets/Downloads/Products/Pt-BR/Fichas_tecnicas/MC-DUR%201177%20WV-APdf n.d.

[132] Correlated Solutions. VIC-2D n.d.

[133] Chau TT, Bruckard WJ, Koh PTL, Nguyen A V. A review of factors that affect contact angle and implications for flotation practice. Adv Colloid Interface Sci 2009;150:106–15. https://doi.org/10.1016/j.cis.2009.07.003.

[134] Wang J, Wu Y, Cao Y, Li G, Liao Y. Influence of surface roughness on contact angle hysteresis and spreading work. Colloid Polym Sci 2020:1107–12. https://doi.org/10.1007/s00396-020-04680-x/Published.

[135] Schoene J, Chudoba R, Hegger J, Raupach M, Jerabek J, Keil A. Experimental and Numerical Analysis of Spalling Effect in TRC Specimens Experimental and Numerical Analysis of Spalling Effect in TRC Specimens*. 2009.

[136] Wille K, Kim DJ, Naaman AE. Strain-hardening UHP-FRC with low fiber contents. Materials and Structures/Materiaux et Constructions 2011;44:583–98. https://doi.org/10.1617/s11527-010-9650-4.

[137] Naaman AE, Reinhardt HW. Characterization of high performance fiber reinforced cement composites - HPFRCC. High Performance Fiber Reinforced Cement Composites 2, E & FN Spon; 1996.

[138] Yoo D-Y, Banthia N, Yoon Y-S. Flexural behavior of ultra-high-performance fiber-reinforced concrete beams reinforced with GFRP and steel rebars. Eng Struct 2016;111:246–62. https://doi.org/10.1016/j.engstruct.2015.12.003.

[139] Wille K, Naaman AE. Pullout Behavior of High-Strength Steel Fibers Embedded in Ultra-High-Performance Concrete. ACI Mater J 2012;109:479–88. https://doi.org/10.14359/51683923.

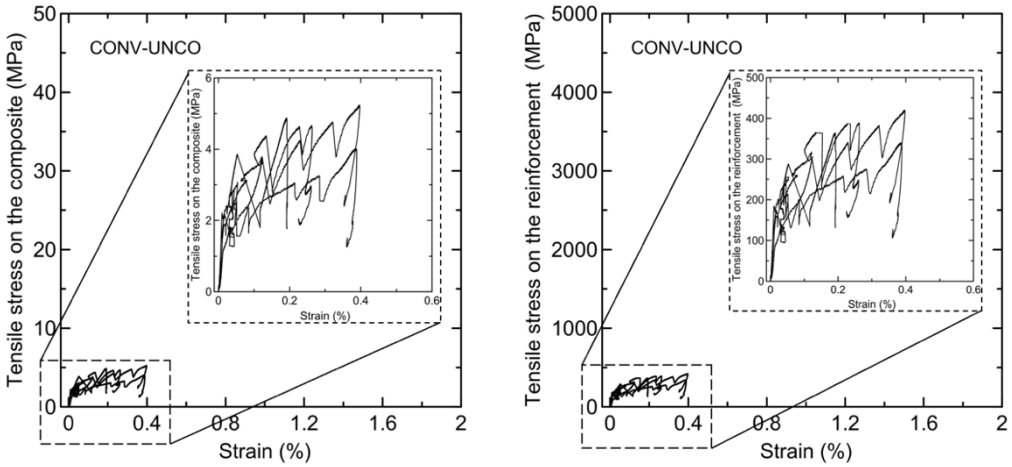
[140] Zhang F, Xu J, Esther B, Lu H, Fang H, Liu W. Effect of shear span-to-depth ratio on the mechanical behavior of composite sandwich beams with GFRP ribs and balsa wood core materials. Thin-Walled Structures 2020;154:106799. https://doi.org/10.1016/j.tws.2020.106799.

[141] Dinh HH, Parra-Montesinos GJ, Wight JK. Shear Strength Model for Steel Fiber Reinforced Concrete Beams without Stirrup Reinforcement. Journal of Structural Engineering 2011;137:1039–51. https://doi.org/10.1061/(ASCE)ST.1943-541X.0000362.

[142] Cucchiara C, La Mendola L, Papia M. Effectiveness of stirrups and steel fibres as shear reinforcement. Cem Concr Compos 2004;26:777–86. https://doi.org/10.1016/j.cemconcomp.2003.07.001.

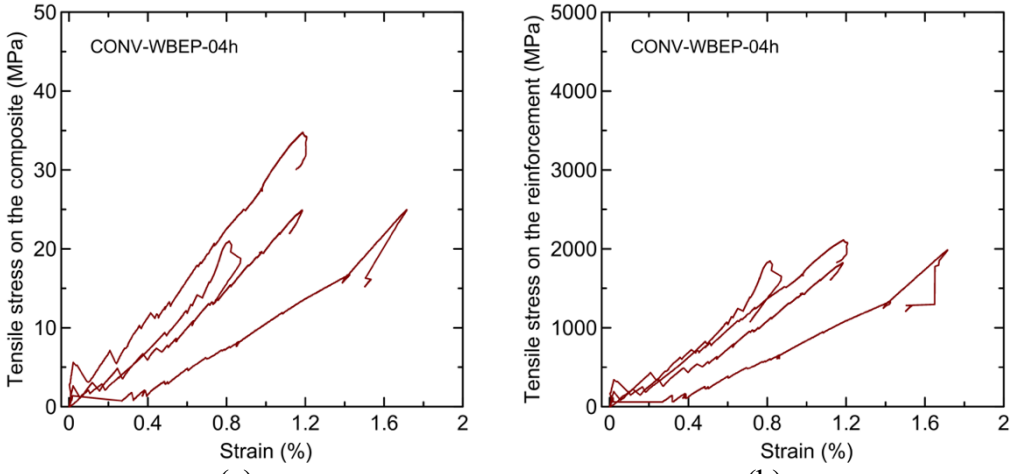
Appendix A

In this section, the tensile stress *vs.* stress curves obtained from the direct tensile tests for all composites are presented.



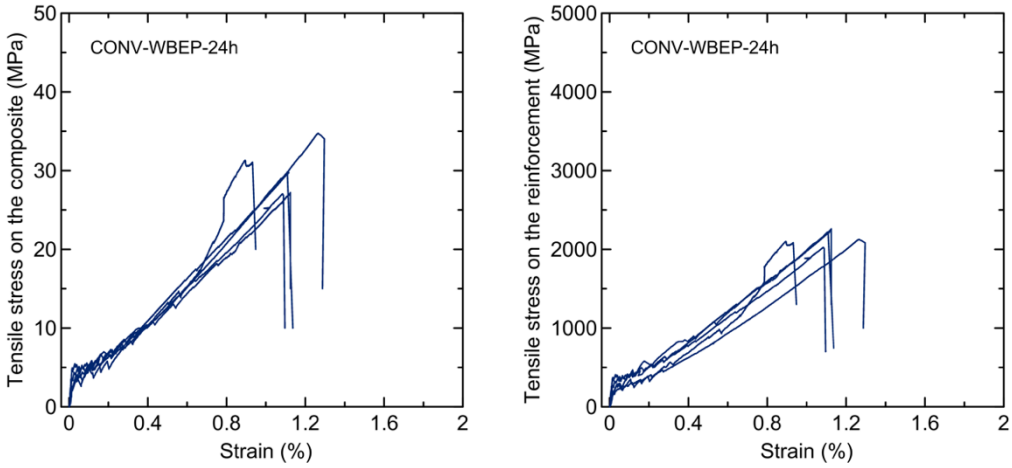
(a) (b)

Figure A.0.1 - Tensile stress *vs.* strain curves of the CONV-UNCO carbon TRC composites with the tensile stress obtained using the: (a) composite cross-sectional area and (b) reinforcement area.



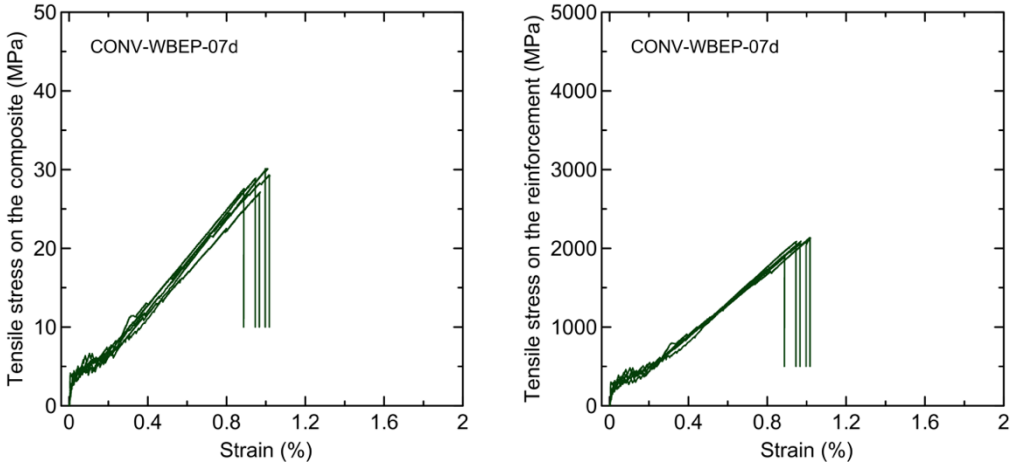
(a) (b)

Figure A.0.2 - Tensile stress *vs.* strain curves of the CONV-WBEP-04h carbon TRC composites with the tensile stress obtained using the: (a) composite cross-sectional area and (b) reinforcement area.



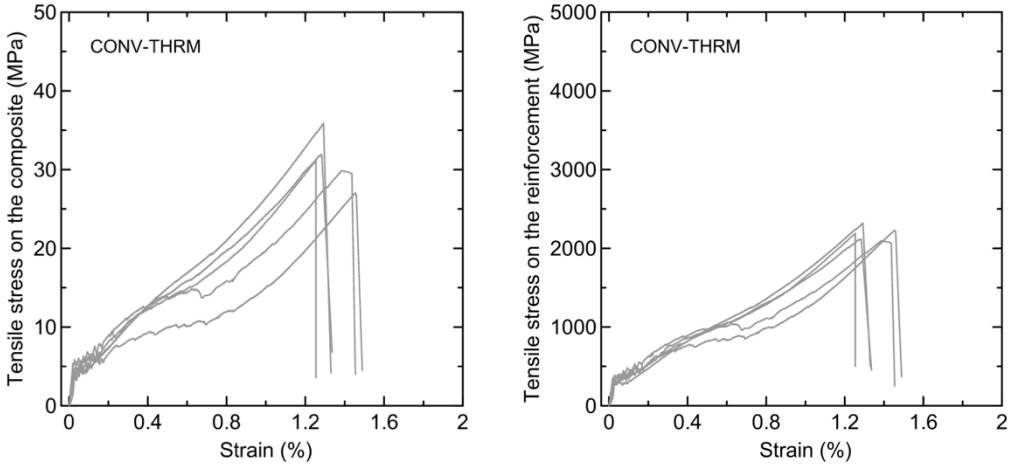
(a) (b)

Figure A.0.3 - Tensile stress *vs.* strain curves of the CONV-WBEP-24h carbon TRC composites with the tensile stress obtained using the: (a) composite cross-sectional area and (b) reinforcement area.



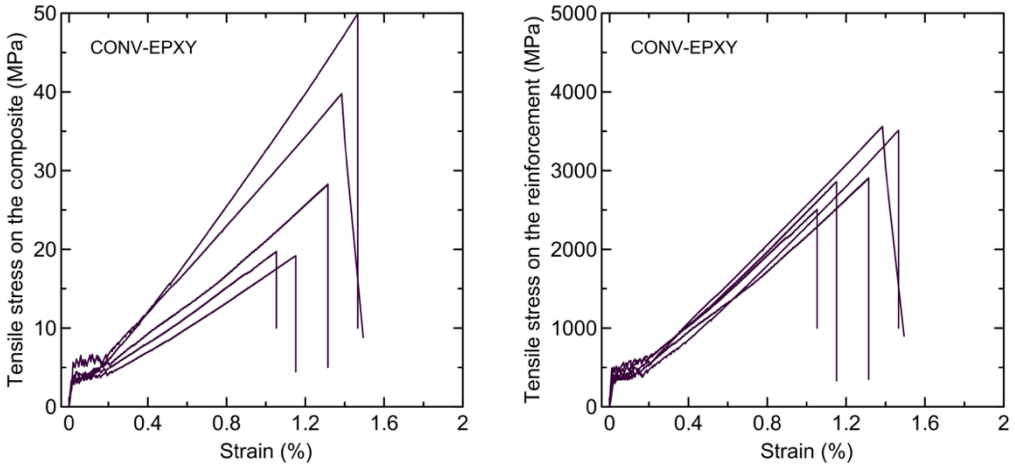
(a) (b)

Figure A.0.4 - Tensile stress *vs.* strain curves of the CONV-WBEP-07d carbon TRC composites with the tensile stress obtained using the: (a) composite cross-sectional area and (b) reinforcement area.



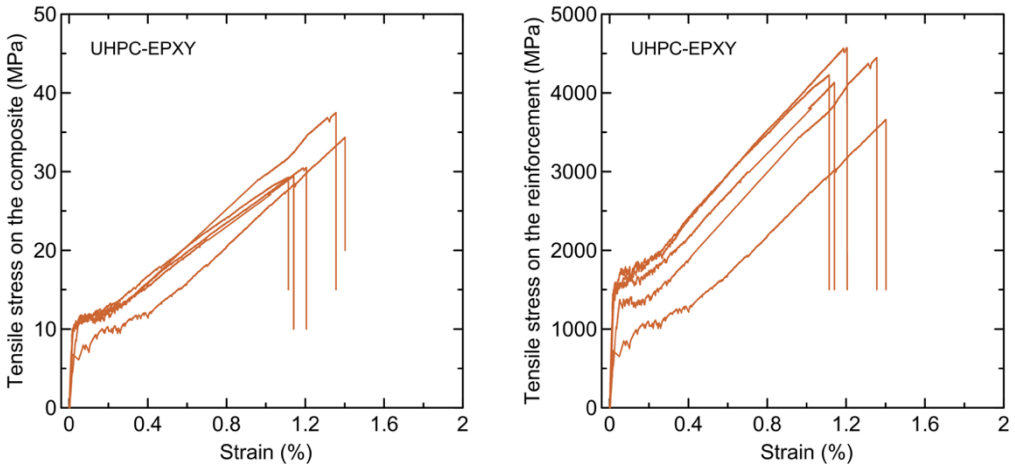
(a) (b)

Figure A.0.5 - Tensile stress *vs.* strain curves of the CONV-THRM carbon TRC composites with the tensile stress obtained using the: (a) composite cross-sectional area and (b) reinforcement area.



(a) (b)

Figure A.0.6 - Tensile stress *vs.* strain curves of the CONV-EPXY carbon TRC composites with the tensile stress obtained using the: (a) composite cross-sectional area and (b) reinforcement area.



(a) (b)

Figure A.0.7 - Tensile stress *vs.* strain curves of the UHPC-EPXY carbon TRC composites with the tensile stress obtained using the: (a) composite cross-sectional area and (b) reinforcement area.